Control mechanisms over the RNA-guided self-assembly of tobacco mosaic virus-based nanotemplates

Kontrollmechanismen zur RNA-gesteuerten Selbstassemblierung Tabakmosaikvirus-basierter Nanotemplate

Von der Fakultät Energie-, Verfahrens- und Biotechnik der Universität Stuttgart
zur Erlangung der Würde eines Doktors der Naturwissenschaften (Dr. rer. nat.)
genehmigte Abhandlung

vorgelegt von
Angela Nicole Schneider
aus Kassel

Hauptberichter:	Prof. Dr. Christina Wege (apl.)
Mitberichter:	Jun.-Prof. Dr. Björn Voß
Tag der mündlichen Prüfung:	09. März 2022

Institut für Biomaterialien und biomolekulare Systeme
Universität Stuttgart
2022

Ein Gelehrter in seinem Laboratorium ist nicht nur ein Techniker; er steht auch vor den Naturgesetzen wie ein Kind vor der Märchenwelt.

Marie Curie

Phantasie ist wichtiger als Wissen, denn Wissen ist begrenzt.

Albert Einstein

Erklärung/Declaration

Hiermit erkläre ich, dass ich die vorliegende Arbeit selbstständig und nur mit Hilfsmitteln durchgeführt habe, die im Text angegeben sind.

I hereby declare that I performed and wrote this thesis independent from further help or other materials than stated.

Name/*Name* Angela Nicole Schneider

Unterschrift/*Signature*

Datum/*Date* 14.12.2021

The experiments presented in this thesis were performed under supervision of Professor Dr. Christina Wege in the Research Unit Molecular & Synthetic Plant Virology (formerly: Department of Molecular Biology and Plant Virology), Institute of Biomaterials and Biomolecular Systems of the University of Stuttgart between March 2014 and June 2017. A part of the experimental work was performed at the University of Paris-Diderot, Laboratoire d'Electrochimie Moléculaire, CNRS, Paris, France under guidance and support of Dr. Christophe Demaille, Dr. Agnès Anne and Dr. Arnaud Chovin.

The present dissertation has a non-cumulative structure.

In the following, parts of the thesis that have been already published in scientific journals are listed. Other parts of this dissertation were presented either as presentations or posters at scientific conferences.

Scientific Publications

Schneider, Angela N.; Eber, Fabian J.; Wenz, Nana L.; Altintoprak, Klara; Jeske, Holger; Eiben, Sabine; Wege, Christina (2016): Dynamic DNA-controlled "stop-and-go" assembly of well-defined protein domains on RNA-scaffolded TMV-like nanotubes. In: Nanoscale 8 (47), pp. 19853-19866. DOI: 10.1039/C6NR03897B.

Wenz, Nana L.; Piasecka, Sylwia; Kalinowski, Matthäus; Schneider, Angela N.; Richert, Clemens; Wege, Christina (2018): Building expanded structures from tetrahedral DNA branching elements, RNA and TMV protein. In: Nanoscale 10 (14), pp. 6496–6510. DOI: 10.1039/C7NR07743B.

Paiva, Telmo O.; Schneider, Angela; Bataille, Laure; Chovin, Arnaud; Anne, Agnès; Michon, Thierry; Wege, Christina; Demaille, Christophe Demaille (2022): Enzymatic activity of individual bioelectrocatalytic viral particles: dependence of catalysis on length and virion type. In: Nanoscale 14 (3), pp. 875-889. DOI: 10.1039/d1nr07445h

Conference Contributions

Invited Talks and Poster

12/2014 Projekthaus NanoBioMater, Stuttgart, Germany

Angela Schneider

"Tobacco mosaic virus particles with domain structure"

Talks

02/2016 Winter School SPP 1569, DFG; Potsdam, Germany

Angela Schneider; Petia Atanasova; Jörg J. Schneider et al.

Status of project DFG-EI 901/1-3 im DFG-SPP 1569 (Antragssteller: Sabine Eiben, Holger Jeske, Joachim Bill, Jörg J. Schneider): "Genetically optimized tobacco mosaic viruses as scaffold for the *in vitro* generation of semiconductor bio/metal-oxide nanostructured architectures"

03/2015 Statusmeeting SPP 1569, DFG; Hillesheim, Germany

Angela Schneider; Petia Atanasova et al.

Perspectives of project DFG-EI 901/1-3 im DFG-SPP 1569 (Antragssteller: Sabine Eiben, Holger Jeske, Joachim Bill, Jörg J. Schneider): "Genetically optimized tobacco mosaic viruses as scaffold for the *in vitro* generation of semiconductor bio/metal-oxide nanostructured architectures"

Posters

03/2017 DPG-Tagung, Bonn, Germany

Angela Schneider, Fabian J. Eber, Nana L. Wenz, Klara Altintoprak, Holger Jeske, Sabine Eiben, Christina Wege
"Tobacco mosaic virus with defined discriminable coat protein domains: Manipulating RNA-directed self-assembly"

02/2016 DGM-Konferenz Bioinspired Materials, Potsdam, Germany

Angela Schneider, Christina Wege, Sabine Eiben

"Tobacco mosaic virus-like nanotubes with defined discriminable subdomains for the fabrication of bio/inorganic materials"

06/2015 Summer School des Projekthauses NanoBioMater, Bad Herrenalb, Germany

Angela Schneider, Fabian Eber, Christina Wege, Sabine Eiben

"DNA oligomer-assisted assembly of tobacco mosaic virus nanotubes with defined subdomain structure"

Table of Contents

List of Abbreviations and Formula Symbols

A_{405}	absorption	IgG	immune globulin G (antibody)
AbMV	abutilon mosaic virus	iva	*in vitro* assembly
ABTS	2,2'-azino-bis(3-ethylbenzo-thiazoline-6-sulphonic acid)	*k*	k-factor
AFM	atomic force microscopy	LiCl	lithium chloride
BSA	bovine serum albumine	M	mol per L
c	concentration	miRNA	micro RNA
CCMV	cowpea chlorotic mottle virus	MOPS	3-(N-morpholino)propanesulfonic acid
cDNA	complementary DNA	[mal]-GOx	maleimide-PEG_{12}-conjugated GOx
CP	coat protein	MWCO	molecular weight cut off
CP_{Cys}	CP of TMV_{Cys}	NaOAc	sodium acetate
CP_{Lys}	CP of TMV_{Lys}	NHS	succinimidyl
$CP_{Lys\text{-}Bio}$	CP of $TMV_{Lys\text{-}Bio}$	nt	nucleotide(s)
d	optical path length	OAs	origin of assembly
DMDC	dimethyl dicarbonate	PAGE	polyacrylamide gel electrophoresis
DNA	deoxyribonucleic acid	PBS	phosphate-buffered saline
ds	double stranded	PCI	phenol : chloroform : isoamyl alcohol
DTLP	TLPs with defined CP domains	PEG	polyethylene glycol
EDTA	ethylenediaminetetraacetic acid	pH	lat. potentia hydrogenii; potential of hydrogen
EtBr	ethidium bromide	pI	isoelectric point
ex.	excess	PPB	potassium phosphate buffer
f.c.	final concentration	PQQ-GDH	quinoprotein glucose dehydrogenase
GOx	glucose oxidase	*r*	radius
h	height	*RCF*	relative centrifugal force
HRP	Horseradish peroxidase	RCNMV	red clover necrotic mosaic virus
hRNA	heterologous RNA	RNA	ribonucleic acid

rpm	rounds per minute
RT	room temperature
S	sedimentation coefficient (Svedberg constant)
SDS	sodium dodecyl sulfate
SPP	sodium potassium phosphate buffer
ss	single-stranded
[s]-GOx	streptavidin-conjugated GOx
[s]-HRP	streptavidin-conjugated HRP
t	time
TEM	transmission electron microscopy
TLP	TMV-like particle
TLS	tRNA-like structure
TMV	tobacco mosaic virus
TMV_{Cys}	TMV mutant S3C
TMV_{Lys}	TMV mutant T158K
$TMV_{Lys\text{-}Bio}$	TMV_{Lys} coupled with NHS-PEG_{12}-Biotin-linkers
UC	ultracentrifugation
UTR	untranslated region
UV	ultraviolet
w	mass fraction
wt	wild type
VIS	visible
ε	extinction coefficient
λ	wavelength
ω	angular velocity

Zusammenfassung

Größe und Anordnung von klar abgegrenzten Bereichen unterschiedlicher Oberflächenchemie auf einzelnen Nanopartikeln sind durch die jeweiligen Herstellungsverfahren limitiert. Virusähnliche Partikel bieten von Natur aus eine Außenfläche genau definierter, aber gut modifizierbarer Makromoleküle auf der Nanoskala und können in vielfacher Weise funktionalisiert werden. Solche Nanoobjekte bieten Möglichkeiten für verschiedene Anwendungen in der Bionanotechnologie, z. B. als Bildgebungs- und Diagnosewerkzeuge, Template für Microarrays, elektronische Bauteile und Biosensoren. Das Tabakmosaikvirus (TMV), ein für den Menschen nicht pathogenes Pflanzenvirus, kann kostengünstig und in großen Mengen in einem Gewächshaus hergestellt werden. Seine Selbstorganisation aus einzelsträngiger Ribonukleinsäure (RNA) von 6395 nt mit 2130 identischen Kopien seines Hüllproteins (*coat protein*, CP) macht TMV zu einem herausragenden und vielseitigen Werkzeug für die Bionanotechnologie. Die viralen Nukleoprotein-Röhrchen sind 300 nm lang, mit einen Außendurchmesser von 18 nm und einem Kanaldurchmesser von 4 nm, und bieten ein hohes Oberfläche-zu-Volumen-Verhältnis sowie eine hohe Stabilität gegen raue Behandlungen oder ungünstige Umgebungsbedingungen. Die Bildung von TMV-ähnlichen Partikeln (*TMV-like particles*, TLPs) kann auch *in vitro* leicht induziert werden – sogar mit synthetischen RNAs, die den TMV-Assemblierungs-ursprung (*origin of assembly*, OAs) beinhalten, und mit genetisch veränderten TMV-CP-Typen, von denen auch unterschiedliche Varianten gemeinsam in einzelne Partikel eingebaut werden können. Um für eine breite Palette von Anwendungen interessant zu sein, sind eine Vielfalt von möglichen Bindungstypen zwischen CPs und funktionellen Molekülen sowie genau vordefinierte Kopplungsstellen von Vorteil.

In dieser Arbeit wurden neue Strategien entwickelt, um räumlich wohldefinierte, selektiv adressierbare CP-Domänen auf einer einzelnen TMV-ähnlichen Nanoröhre zu erzeugen. Zu diesem Zweck wurde dynamische DNA-Nanotechnologie angewendet, um die RNA-vermittelte Selbstassemblierung von TMV-CP zu steuern. Eine "*Stop-and-go*-Technik" nutzt DNA-Oligonukleotide als "Stopper", die sequenzspezifisch an definierten Stellen in der TMV-RNA hybridisieren und so ihre Verpackung in TMV-CP an der Hybrid-Duplex-Position blockieren. Ein nicht-bindender Überhang ("*Toehold*") ermöglicht den Neustart der Assemblierung mithilfe eines vollständig revers-komplementären "Ablöse"-DNA-Oligonukleotids (als "*Fuel*"), so dass durch Verdrängung des Stopper-Strangs eine benachbarte CP-Domäne mit andersartigen Bindungsstellen wachsen kann, wenn die erste CP-Variante gegen eine andere ausgetauscht wurde. Dafür wurden Stopper identifiziert, die

effektiv an eine RNA-Position hybridisieren und die Assemblierung behindern. So konnte das Verpacken von TMV wt-RNA effizient an Stellen im 3'-Bereich, in Bezug auf den OAs, blockiert werden. Die nicht-vollständig assemblierten Nanoröhrchen blieben über einen Zeitraum von 12 Tagen bei 4 °C sowie während ihrer Reinigung durch Ultrazentrifugation erfolgreich gestoppt, wobei auch der heraushängende RNA-Teil intakt blieb. Durch DNA-vermitteltes Ablösen des Stoppers ließ sich die Assemblierung wieder starten. Zur Erzeugung von Nukleoprotein-Röhrchen mit zwei verschiedenen Domänen wurde ein Protokoll zur differentiellen Ultrazentrifugation entwickelt, um CP-Varianten auszutauschen und nicht erwünschte TLP-Aggregate abzutrennen. Zur Visualisierung der beiden, in ihrer Länge genau definierten Abschnitte wurde Avidin mittels Bioaffinitätskopplung an die biotinylierten 3'-terminalen Domänen immobilisiert. So wurde gleichzeitig die ortsselektive Funktionalisierbarkeit der Domänen bewiesen.

Um zu untersuchen, ob dieser DNA-basierte Kontrollmechanismus auf Stopper-Bindungsstellen in TMV-RNA beschränkt war oder auf beliebige RNA-Sequenzen übertragen werden konnte, wurden drei Plasmid-Konstrukte hergestellt, mit denen heterologe RNAs (hRNAs) mit TMV-OAs *in vitro* transkribiert wurden. Diese wurden auf ihr Verhalten in *Stop-and-go*-Experimenten untersucht. Sie führten erfolgreich zu partiell assemblierten Nanoröhrchen, wenn die hRNAs in heterologen Regionen 3' vom OAs durch Stopper blockiert waren, und auch die anschließende vollständige Verpackung nach Verwendung der Strangverdrängungsreaktion wurde erreicht. So wurde die generelle Anwendbarkeit der *Stop-and-go*-Technik zur Assemblierungskontrolle von Nukleoproteinröhrchen aus RNAs mit integrierter TMV-OAs-Sequenz und TMV-CP festgestellt. Allerdings zeigten sich erhebliche Unterschiede in der Effizienz unterschiedlicher DNA-Stopper, die sich nicht direkt aus ihrem Schmelzpunkt oder ihrer Primärsequenz ableiten ließen. Studien zu einer höheren Anzahl von Stopper-Bindungsstellen, sowohl 3' als auch 5' des OAs, lieferten tiefere Einblicke in Randbedingungen und Grenzen beim Unterbrechen der Assemblierung *in vitro*.

Sekundärstrukturen diskreter RNA-Sequenzen wurden mit gängiger Software simuliert und in Korrelation zu den experimentell ermittelten Effizienzen des Stoppens gestellt, sodass der Einfluss der räumlichen Faltung auf die Zugänglichkeit der RNA für die Hybridisierung von DNA-Oligonukleotiden diskutiert werden konnte. Dabei konnten aber mehrere praxisrelevante Parameter durch die verfügbaren Computerprogramme nicht berücksichtigt werden, so dass die *In-silico*-Verfahren zwar einige Erklärungsansätze für ineffiziente Stopperpositionen ergaben, die Komplexität der Interaktionen zwischen RNA, DNA und CP aber für sicherere Vorhersagen weitere Analysen und Simulationen benötigen wird.

Experimentell wurde die Verdrängung von Stopper-DNA-Strängen durch revers-komplementäre Ablöse-DNA-Oligomere sowie Temperaturerhöhung untersucht. Es wurden einzelne Sequenzen identifiziert, an denen sich zwei Stopper gleichzeitig an TMV-RNA hybridisieren, aber selektiv nacheinander ablösen ließen. Die sukzessive Entfernung beider Stopper und schrittweise Assemblierung der RNA/DNA-Hybride mit verschiedenen CP-Varianten erzeugte erstmals Nanoröhren mit drei verschiedenen, genau definierten Subdomänen, die entweder durch zwei miteinander kombinierte 3'-Stopper, oder aber durch einen 5'- und einen 3'-Stopper vermittelt wurden. Die so erzeugten, unterschiedlich substrukturierten TMV-CP-exponierenden Dreidomänen-Template wurden zur räumlich definierten Anordnung von Biomolekülen auf der Nano- bis Mesoskala untersucht, mit Blick auf Anwendungen als künstliche Multienzymkomplexe oder in Multiplex-Biosensoren. Zu diesem Zweck wurden Enzyme oder Antikörper an einzelne Domänen der TLPs gekoppelt. Die Integrität der ortsselektiv konjugierten Glucoseoxidase bzw. Meerrettichperoxidase wurde in Lösung mit einem kolorimetrischen Glucose-Nachweis analysiert. Die Positionen von nachfolgend gebundenen Antikörpern an einzelne Domänen wurden im Partnerlabor in Paris mittels *In-situ*-Rasterkraftmikroskopie an auf Goldoberflächen immobilisierten TLPs sichtbar gemacht. Die vielversprechenden Resultate deuten darauf hin, dass die TMV-Dreidomänen-Partikel als neuartige Nanoträger-Systeme vielseitige Möglichkeiten bieten, um synthetische Enzymkaskaden herzustellen, z. B. für *Point-of-Care*-Testgeräte oder für die Grundlagenanalytik über elektrochemische Rasterkraftmikroskopie (AFM-SECM).

1 Abstract

Both size and arrangement of well-defined regions of different surface chemistries on individual nanoparticles are limited by their respective fabrication processes. Virus-like particles inherently provide an outer surface of well-defined but readily modifiable macromolecules at the nanoscale and can be functionalized in multiple ways. Such nanoobjects offer opportunities for various applications in bionanotechnology, such as imaging and diagnostic tools, templates for microarrays, electronic devices, and biosensors. Tobacco mosaic virus (TMV), a plant virus that is nonpathogenic to humans, can be produced inexpensively and in large quantities in a greenhouse. Its self-assembly from single-stranded ribonucleic acid (RNA) of 6395 nt with 2130 identical copies of its coat protein (CP) makes TMV an outstanding and versatile tool for bionanotechnology. The viral nucleoprotein tubes are 300 nm long, with an outer diameter of 18 nm and a channel diameter of 4 nm and offer a high surface-to-volume ratio and high stability against harsh treatments or adverse environmental conditions. The formation of TMV-like particles (TLPs) can be easily induced *in vitro* – even from synthetic RNAs containing the TMV origin of assembly (OAs) and with genetically modified TMV-CP types, of which, moreover, different variants can also be incorporated together into single particles. To be of interest for a wide range of applications, a large number and variety of possible binding types between CPs and functional molecules, as well as well-defined coupling sites, are advantageous.

In this work, new strategies were developed to generate spatially well-defined, selectively addressable CP domains on a single TMV-like nanotube. To this end, dynamic DNA nanotechnology was applied to drive RNA-mediated self-assembly of TMV-CP. A "stop-and-go technique" uses DNA oligonucleotides as "stoppers" that hybridize sequence-specifically at predefined sites in the TMV-RNA, blocking its packaging into TMV-CP at the hybrid duplex position. A non-binding overhang ("toehold") allows subsequent restart of assembly using a fully reverse-complementary "release" DNA oligonucleotide (as "fuel"), so that an adjacent CP domain with different binding sites can grow after displacing the stopper strand and replacement of the first CP variant by a second one. To do this, stoppers were identified that effectively hybridize to a specific RNA position and interfere with nanotube assembly. It was shown that packaging of TMV wt-RNA could be efficiently blocked at sites in the RNA 3' region, relative to the OAs. The incompletely assembled nanotubes remained successfully stopped over a period of 12 days at 4 °C as well as during their purification by ultracentrifugation, leaving the protruding RNA portion intact. DNA-mediated

detachment of the stopper allowed assembly to be restarted. To generate nucleoprotein tubes with two different domains, a differential ultracentrifugation protocol was developed to exchange CP variants and separate unwanted TLP aggregates. To visualize the two segments, precisely defined in length, avidin was immobilized on the biotinylated 3'-terminal domains using bio-affinity coupling. This simultaneously demonstrated the site-selective functionalization of specific domains. To investigate whether this DNA-based approach was limited to stopper-binding sites in TMV-RNA or could be applied to arbitrary sequences, three plasmid constructs were generated to transcribe heterologous RNAs (hRNAs) containing TMV-OAs *in vitro*. These scaffolds were evaluated for their behavior in stop-and-go assembly experiments. They successfully resulted in partially assembled nanotubes when hRNAs were blocked by stoppers in heterologous regions 3' from the OAs, and subsequent complete packaging following the strand displacement reaction was also achieved. Thus, the general applicability of the stop-and-go technique for assembly control of nucleoprotein tubes from RNAs with integrated TMV-OAs sequence and TMV-CP was verified. However, significant differences were found in the efficiency of different DNA stoppers, which could not be directly deduced from their melting point or primary sequence. Subsequent studies on a higher number of stopper binding sites, both 3' and 5' of the OAs, provided deeper insights into boundary conditions and limitations in disrupting assembly *in vitro*.

Secondary structures of discrete RNA sequences were simulated with common software and correlated to the determined efficiencies of stopping, so that the influence of spatial folding on the accessibility of RNA stretches for stopper binding could be discussed. In this context, a number of practically relevant experimental parameters could not be considered for by the available computer programs, so that although the *in silico* methods yielded some explanations for inefficient stopper positions, the complexity of the interactions between RNA, DNA, and CP will require further analysis and simulations for more confident predictions.

Experimentally, the displacement of stopper DNA strands by reverse-complementary detachment of DNA oligomers as well as temperature-induced was investigated. Singular sequences were identified that allowed two stoppers to hybridize simultaneously to TMV RNA but to be selectively detached sequentially. Successive removal of both stoppers and stepwise assembly of the RNA/DNA hybrids with different CP variants generated nanotubes with three different, well-defined subdomains for the first time and mediated either by two 3' stoppers combined with each other, or by a 5' and a 3' stopper. The resulting differently substructured TMV-CP-exposing three-domain TLPs were investigated for spatially defined assembly of biomolecules on the nano- to mesoscale, with a view to applications as artificial multienzyme complexes or in multiplex

biosensors. For this purpose, enzymes or antibodies were coupled to single domains. The integrity of site-selectively conjugated glucose oxidase or horseradish peroxidase was analyzed in solution using colorimetric detection. The positions of subsequently bound antibodies to individual domains were visualized by *in situ* atomic force microscopy in a partner lab in Paris, using TLPs immobilized on gold surfaces. The promising results indicate that the TMV three-domain particles, as novel nanocarrier systems, offer versatile opportunities to fabricate synthetic enzyme cascades, *e.g.*, for point-of-care assay devices or for basic analysis *via* electrochemical atomic force microscopy (AFM-SECM).

2 Introduction

2.1 Bionanotechnology - a short historical overview

As early as 1959, Richard Feynman shared his visions of nanometer-scale technology with the audience in his famous lecture "There's Plenty of Room at the Bottom". He encouraged scientists and engineers to develop methods and devices to manipulate and control molecules atom by atom (Feynman 1960). His main ideas were the compression of data to even smaller spaces, the advantages of miniaturized computers, the need for better electron microscopes, the design of microscopic machines, and physical molecule manipulation as a form of synthetic chemistry.

However, the term "nanotechnology" was first mentioned by Norio Taniguchi in 1974 on a conference to explain processes in semiconductors at the nanoscale, but it was not used again until the early 1980s. In the 1980s, the beginning of the golden era of nanotechnology was pioneered by the work of K. Eric Drexler and Richard Smalley and his team.

Drexler contrasted Feynman's approach of bringing products from macroscopic scale to nanometer scale with his approach of generating functional units such as pumps, motors and containers from biological building blocks (Drexler 1981; Lee and Moon 2020b) and thus referred to differences in the terms used today: top-down and bottom-up approaches. Drexler introduced protein engineering to design new proteins with special properties and assemble them into larger molecular units to use as nanomachines (Drexler 1981, 2004). Smalley, along with Robert Curl and Sir Harold Kroto, discovered spherical, stable arrangements consisting of 60 carbon atoms after vaporizing graphite with laser irradiation (Kroto et al. 1985). They earned the Nobel Prize in Chemistry in 1996 for these fullerenes, also called bucky balls. In addition to this groundbreaking contribution, Smalley's team enriched nanotechnology and its biomedical applications with other innovative contributions (Papazoglou and Parthasarathy 2007).

Clear terminological definitions of the term (bio)nanotechnology have been called for time and again but are not strictly followed. The field of nanotechnology comprises many scientific and technical fields such as chemistry, physics, engineering, medicine, biology, etc. It is rather considered as a generic term for properties, products and processes on the nano and micrometer scale. Bionanotechnology makes use of biological macromolecules and their notable performances to generate novel nanomaterials with precisely controlled functions, shapes and composites for various applications. Chad A. Mirkin achieved breakthroughs to bionanotechnology with his work in

the many different areas of self-assembled monolayers, nanoparticles, DNA-based materials, nanolithography and the design of molecular electronic devices (Caldwell et al. 1993; Mirkin et al. 1996; Piner et al. 1999; Storhoff et al. 1997; Rosi and Mirkin 2005; Mirkin and Ratner 1992).
Developments in bionanotechnology show a range of opportunities, but also pose challenges. Many products and devices have become indispensable, for example for healthcare-related applications as nanocarriers for therapeutics or vaccines (Hou et al. 2021; Tenchov et al. 2021; Su and Kang 2020; Steinmetz et al. 2020) or as templates of biosensors (Medintz et al. 2003; Koch et al. 2018; Alafeef et al. 2020). The main challenges of bionanotechnology are considering biocompatibility and long-term effects of nanostructures on the organism through direct or indirect application on the human body (Bruckman et al. 2014; Baranowska-Wójcik et al. 2020; Amani et al. 2019). Bionanotechnology will continue to enrich daily life, but its development and application, as well as that of any other technology, should be done with caution and consideration of its consequences.

2.1.1 Nucleic acids in bionanotechnology

Nucleic acids, including DNA and RNA, are polymers containing four different nucleobases: adenine (A), cytosine (C), and guanine (G) are found in both, DNA and RNA. However, they differ in the fourth nucleotide: thymine (T) is found in DNA and uracil (U) in RNA. Within nucleic acid strands, the respective nucleotides can stably hybridize and form hydrogen bonds with appropriate partner nucleotides. DNA prefers Watson-Crick base paring, *i.e.*, A with T and G with C, whereas RNA can also build non-canonical base pairs, like G with A or T. They also adopt different structural motifs due to the differences in base pairing as it is reviewed in detail in Guo 2010. A DNA helix preferentially forms the typical B form, whereas RNA adopts the A form configuration under physiological conditions. The thermodynamically most stable form of the double helix is the RNA-RNA interaction. Comparisons of RNA-DNA and DNA-DNA interactions show that their sequence determines which of the helices is more stable (Sugimoto et al. 1995; Searle and Williams 1993).
Nucleic acids have a broad spectrum of biochemical roles, such as storage and transfer of genetic information, catalytic functions, regulation of gene expression, etc. Constructing nucleic acid-based materials has become an important technique in bionanotechnology and take advantage of the key properties of DNA and RNA, hybridization, self-assembly, stability of branched structures and convenient synthesis of desired sequences (Lee and Moon 2020a; Seeman 2010). The fabrication of nanoparticles requires building blocks that are predictable and precise and can be functionalized accordingly. Such nucleic acid-based building blocks are produced using various bottom-up approaches, resulting in two- or three-dimensional constructs. DNA nanotechnology has produced

several functional units for various applications over the last 40 years. Due to the well predictable double helical conformations, initial work was aimed at well-defined DNA structures, like cubes (Chen and Seeman 1991), tetrahedra (Goodman et al. 2005) or DNA origami (Rothemund 2006; Gu et al. 2009), as well as arrangements that served as templates, *e.g.* to generate nanowires from inorganic materials (Braun et al. 1998). However, the possibility of using DNA building blocks to generate DNA nanomechanical devices quickly came to the attention of the researchers (Seeman 2005; Bath and Turberfield 2007).

In biological organisms there are many models of molecular machines, the most complex in cells are proteins. Typical representatives include ATP synthase, a rotary motor that catalyzes the synthesis of adenosine triphosphate (ATP), or linear motor proteins such as dynein and kinesin, which "walk" along microtubules to transport biomolecules, and myosin, which moves along actin filaments and is responsible for muscle contraction. All of these motor proteins require ATP as an energy source and are already used in nanotechnology (Hess et al. 2004; van den Heuvel and Dekker 2007).

One of the first active DNA-based nanomaterials with well-defined structure was a DNA switch based on the transition of the B form to the Z form of DNA by the addition of a stabilization complex, hexaamminecobalt(III) chloride (Mao et al. 1999). However, since only two mechanical states were possible here, further possibilities were exploited by nucleic acid hybridization in sequence-dependent manner.

Yurke and his team used the control over the hybridization of diverse predefined DNA strands as a technique to create a circuit of opening and closing DNA tweezers (Yurke et al. 2000). These tweezers were assembled in their opened state from three structuring oligonucleotides and could be closed by adding a closing DNA strand. This closing strand as one component of the "fuel" oligonucleotides contained fully complementary sequences to the tweezers plus an additional non-complementary overhang region. As the circuit progressed, the addition of the second fuel component, the removal strand, displaced the closing strand, as the two parts were fully complementary, allowing the tweezers to open. This strand displacement reaction is expected to begin with the hybridization of both fuel components at the overhang, also called toehold. The waste product of this reaction is the fuel duplex, which diffuses away from the tweezers. The latter can re-enter a new cycle. The success and efficiency of the tweezers was validated by fluorescence resonance energy transfer (FRET). This study established the toehold-mediated strand displacement reaction, and became widely accepted in the dynamic DNA nanotechnology as a technique for the construction of nanomechanical devices as reviewed in detail in Zhang and Seelig 2011. DNA walkers have

been developed, inspired by motor proteins such as kinesin, by applying strand displacement reactions (Sherman and Seeman 2004). These DNA walkers move along a one-dimensional DNA track with one step per added input strand. DNA walkers are, among other things, suitable for transporting molecules as shown in Gu et al. 2010. Here, gold nanoparticles were picked up as cargo by DNA walkers along a DNA origami pathway and transported further. Recent studies suggest DNA walkers in dynamically controlled reaction, *e.g.*, by changing the pH (Yao et al. 2020) and for use in analytical and diagnostic applications, like the ultrasensitive detection of antibiotics (Zhang et al. 2020) or cancer-related genes (Wu et al. 2020), in which both systems were constructed in a three-dimensional manner.

DNA is considered a pioneer material for nucleic acid-based bionanotechnology; however, RNA is increasingly becoming a good alternative with its own advantages for nanomaterials and their construction which are briefly discussed below. This can rely on the ability of RNA to self-assemble into more rigid structures than is simply possible for DNA. In addition, artificial RNA can be designed to self-assemble immediately following its synthesis by *in vitro* transcription. In a recent study, it was even shown that by designing a single RNA transcript, an *in situ* biosensor for the detection of micro RNAs (miRNA) could be generated (Kobori et al. 2019). Through hybridization of the *in vitro* transcribed RNA to miRNA, the RNA adopted a different structural conformation, allowing the broccoli aptamer to form, which activated the added fluorescent probe so that this signal could be analyzed optically. Such strand displacement reactions are adapted from the previously presented methods of DNA nanotechnology and are even used in a dynamic manner. A recent study applied principles of dynamic RNA nanotechnology to construct conditioned guide RNAs that directs the function of a CRISPR protein effector, as is common for dynamic DNA nanotechnology (Hanewich-Hollatz et al. 2019).

Also due to its natural functions, RNA can be successfully used for various applications. For example, specifically selected RNA aptamers are used as biosensors in surface plasmon resonance assays (Oguro et al. 2009). In particular, RNA nanotechnology has a major impact on nanomedicine because it holds tremendous advantages such as it can both transfer and detect molecules in a targeted manner, and individual subunits can be functionalized in different ways, making it possible to combine detection and therapy in an RNA nanoparticle as it is reviewed in Guo 2010. In addition, the protein-free production of nanoparticles does not stimulate undesired reactions of the immune system.

2.1.2 Spatially arranged biomolecules on nanocarriers for bionanotechnology

In nature, nucleic acid complexes with protein domains are found, *e.g.*, in the form of ribosomes, spliceosomes, or RNA-induced silencing complexes (RISCs). In these nucleoprotein structures, which are important for various cellular synthesis and regulatory mechanisms, both RNA and proteins take on these tasks and serve as structural donors and catalysts. It is therefore of great interest to build new defined structures from nucleic acids and proteins that could achieve diverse functionality. In addition to the self-assembly of RNA and DNA, the ability of some proteins to self-assemble could be exploited to gain access to a range of higher order functional structures (Chandrasekaran 2016). The two- and three-dimensional assembly of biomaterial-based complexes on surfaces has been extensively studied over the last decades.

Since virus-based biomaterials have been investigated in the course of this thesis, their surface immobilization will be briefly discussed below. There are several principles for immobilization of viral nanoscale constructs on surfaces, as described in detail for tobacco mosaic virus (TMV)-based particles (Chu et al. 2018). The simplest of the methods is the nonspecific attachment to a surface through attractive interactions (Koch et al. 2015; Atanasova et al. 2011). As specific methods, nucleic acid-based hybridization (Eber et al. 2013; Mueller et al. 2011), binding into polymeric complexes (Tseng et al. 2006), and a thiol-based interaction on gold surfaces (Royston et al. 2008; Chu et al. 2016) have been investigated, leading to diverse spatial arrangements. All the immobilization techniques play an important role in getting the bionanoscaffolds into a two- or three-dimensional arrangement, for example such three-dimensional ordered nano constructs have been used for the surface design of battery electrodes (Royston et al. 2008) or anti-reflective current collectors (Chiang et al. 2012).

However, another important research interest lies in the spatial arrangement of functional biomolecules on the surface of the nanoscaffolds. Various biological functions, for example the adhesion of viruses or bacteria to a cell surface or the binding of cells to other cells or antibodies, require a spatially controlled arrangement of the respective target molecules on the nano- and micrometer scale. For further research into essential biological pathways and for the development of novel diagnostic and pharmaceutical devices, multi- and polyvalent carriers of ligands with site-selectively addressable binding locations at tunable lateral spacings are necessary building blocks (Mammen et al. 1998; Koch et al. 2016; Küchler et al. 2016).

The generation of spatially ordered artificial multienzyme complexes provide advantages in biocatalysis as it was shown by a DNA-controlled approach (Müller and Niemeyer 2008) but it is also suggested for viral templates to serve as nanocarriers with three-dimensionally arranged enzymes

(Cardinale et al. 2012; Koch et al. 2015). As viral templates, plant viruses are preferred because they are non-pathogenic to humans and stable over a wide range of physical and chemical conditions. As nucleoprotein complexes, several plant viruses offer the above-mentioned advantages: their nucleic acid-based genomes and capsid proteins spontaneously assemble into more complex structures with highly ordered protein arrangement, and their individual components can be genetically and chemically modified and functionalized. In a previous study from our group, the plant virus TMV was presented as a multivalent platform to bring two different enzymes, glucose oxidase and horseradish peroxidase, into spatial proximity in a mixed assembly (Koch et al. 2015). These enzyme-loaded scaffolds showed advantages in terms of their storage stability and reusability as glucose detection devices. The increased immobilization efficiency of streptavidin-conjugated enzymes achieved by biotinylated TMV adapters also resulted in higher enzyme activities captured, due to the scaffolding effect of the TMV-like nanocarriers determined in comparison to enzymes directly bound into a microtiter plate. Another study on a two-enzyme cascade used potato virus A as a nanoscaffold and decorated the viral template with two different enzymes using virus-specific antibodies (Besong-Ndika et al. 2016). A sandwich ELISA (enzyme-linked immunosorbent assay) approach was used to achieve simultaneous purification of recombinant enzymes from cell lysate and immobilization of these enzymes on the nanocarriers. The spatial proximity of active sites of multiple enzymes strengthened the cascade reaction, reduced the diffusion distances and thus increased the overall efficiency of the metabolic pathway (Conrado et al. 2008). The effect of spatial arrangement was recently demonstrated by determining increased enzyme activity of three enzyme variants assembled on the T4 phage capsid compared to measurements in solution (Liu et al. 2020). This could also be shown for TMV-like particles serving as scaffolds to connect three distinct enzymes *via* protein pairs as linker molecules to the nanocarriers (Wei et al. 2020). The as-designed synthetic multienzyme complex was generated in bacterial cells.

2.2 Tobacco mosaic virus as a versatile model – then and now

As important as tobacco mosaic virus (TMV) has become as a biological component in bionanotechnological applications, it has played a key role in the discovery of virology. Therefore, this chapter will give a brief overview of TMV as a historically valuable model virus as well as will introduce its important features such as its dimensions, self-assembly ability, and tailored synthesis capabilities that make it an excellent tool and template for bionanotechnology. In 1886, Adolf Meyer investigated a disease of tobacco plants. Because of the mosaic-like symptoms of the leaves, he called this syndrome tobacco mosaic disease. He was able to show that the reason was a pathogen, as it could be transferred to healthy leaves *via* plant sap from affected leaves (Lustig and Levine 1992). Meyer's observations were laying one of the foundations of plant virology. A few years later, Dimitri Ivanovsky started investigations of tobacco mosaic disease building on Meyer's findings. He performed various filtration methods with infectious plant sap to remove bacteria, but the filtrate remained infectious (Lustig and Levine 1992; Zaitlin 1998). His observations alone suggested a pathogen smaller than bacteria and every similar thing previously known, and initiated many years of further investigation until the discovery of the virus. At the same time, Martinus Beijerinck studied the infectious plant sap filtrate and published in 1898 that it contained a new pathogen, smaller and different from previously known pathogenic agents, that could multiply in living plants. He described it as a contagious living fluid ("contagium vivum fluidum") that was liquid and soluble and called this fluid "virus" (Lustig and Levine 1992; Zaitlin 1998). Thus, tobacco mosaic virus (TMV) was the first virus to be discovered and initiated an era around a variety of studies on diverse viruses, viral components, and their structures. TMV played a key role in the history of virology and is significant not only because of the discovery of the viral concept. It was the first virus to be purified and visualized by X-ray crystallography and electron microscopy. Many conceptual progresses of virology were developed using TMV, *e.g.*, the chemical composition of a virus (RNA and proteins) and the isolation of the individual components (Lustig and Levine 1992). Other milestones include the use of the genome of TMV to prove that infectious or genetic information is stored in RNA, the concept of self-assembly by dissociated components into an infectious virus, and the first identification of the sequence of a viral coat protein (Zaitlin 1998; Fraenkel-Conrat 1986).

Tobacco mosaic virus belongs to the genus *Tobamovirus*, specified as positive-sense single-strand RNA virus that is non-enveloped and possesses a helically arranged rod-shaped structure. TMV infects especially tobacco plants and other members in the family *Solanaceae* as well as many

different other families, and shows conspicuous features after infection of a plant like stunted growth and the characteristic mosaic-like discoloration and brittleness of the leaves (exemplarily shown in ***Fig. 2-1***).

2.2.1 Tobacco mosaic virus structure and assembly

TMV in its native state is a 300 nm nucleoprotein tube with an outer diameter of 18 nm. The virus is comprised of a single-stranded, positive-sense RNA of 6395 nt (Goelet et al. 1982) helically encapsidated by coat proteins (CP). The nucleic acid is fully protected, as it is embedded in an inner groove between the proteins with a diameter of 8 nm, but the hollow central channel with 4 nm diameter is given by the CP arrangement (***Fig. 2-1***) (Namba et al. 1989; Fromm et al. 2015).

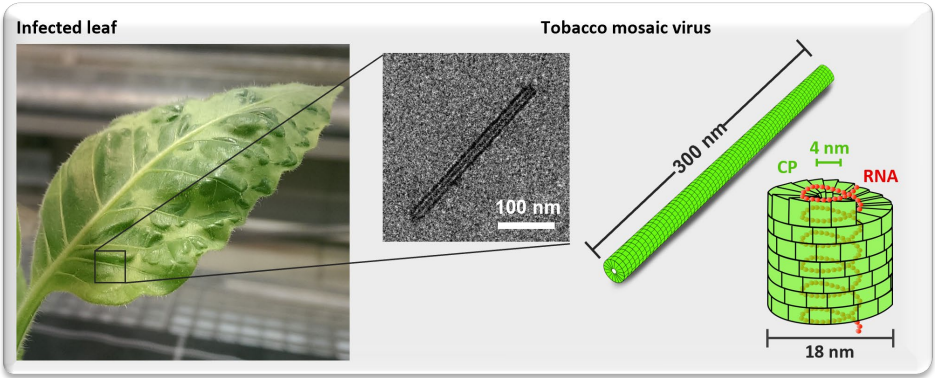

Figure 2-1 Tobacco mosaic virus infection: *N. tabacum* "Samsun" nn leaf infected with TMV (left). Illustration of a TMV particle stained with uranyl acetate, visualized *via* transmission electron microscopy (mid) in contrast to schemes depicting the length and diameter of TMV (right). The inner channel has a diameter of 4 nm specified by CP (green), the RNA (red) is embedded in an inner grove between the protein helix.

The capsid is comprised of 2130 copies of its CP with a molecular size of a single CP of 17.5 kDa. Isolated CPs vary in their interactions depending on pH, temperature and ionic strength as it was proposed by Durham et al. (1971). At neutral pH and low ionic strength, isolated CP is in an equilibrium of the aggregated states, predominantly composed of 20S aggregates. 20S aggregates, also called CP disks, are a formation of a double layer of 34 CPs. Another minor content are A-proteins which are described as a mixture of smaller aggregates of three to six subunits (for a detailed review see: Butler 1999). Both, CP disks and A-proteins are important players in the self-assembly process. TMV-RNA encodes at least four proteins: a 126-kDa protein, a 183-kDa protein (a translational read-through product of the 126-kDa protein), a cell-to-cell movement protein (MP, 30 kDa), and

the CP (17.5 kDa) (Goelet et al. 1982). Both, the 126-kDa and the 183-kDa proteins are directly translated from the ss(+)RNA. The expression of both proteins is needed for efficient replication (Ishikawa et al. 1986) and is depicted as replicase in genome maps of this thesis. In contrast, MP and CP are synthesized from subgenomic RNAs and are not essential for replication (Chujo et al. 2015; Palukaitis and Zaitlin 1986).

The genome has a 5'-m^7G-cap, followed by a short untranslated region (UTR), also called Ω- or 5' leader sequence (68 nt) (Tanguay and Gallie 1996). TMV lacks a 3' poly(A) tail but possesses a ≈ 200 nt long 3' UTR. The 3' UTR consists of two domains: the tRNA-like structure (TLS) of 105 nt at the 3' terminus including two pseudoknots and a domain upstream of the TLS that forms three pseudoknots (***Fig. 2-2a***) (Guilley et al. 1979; Rietveld et al. 1984; van Belkum et al. 1985; Zeenko et al. 2002). The upstream pseudoknot domain (UPD) serves as the functional equivalent to a poly(A) tail. Both termini, the 5' capped Ω sequence and the 3' UPD promote the translational efficiency (Tanguay and Gallie 1996).

A major relevance for self-assembly of viral particles plays another structural motif, the origin of assembly (OAs) sequence. The OAs is located approximately 1000 nt upstream of the 3' RNA end (Zimmern and Wilson 1976; Zimmern 1977). The proposed sequence (nt 5290-5527 of the TMV-RNA sequence according to (Goelet et al. 1982)) consists of three symmetrically spaced hairpins (stem and loop structures) (***Fig. 2-2b***) which become successively coated by the three first disks during assembly (Zimmern 1983). The 3' terminal stem loop of this sequence, named stem loop A, is the most stable, whereas the other hairpins B and C lack GC base pairs, consequently those structures are bound weaker (Zimmern 1983). Stem loop A is the core sequence of the nucleation initiation and defined as the nucleation loop that intercalates between the first protein disk layers during assembly initiation. Additionally, mutation studies of the loop A sequence revealed that the AAGAAGUUG motif was necessary for a rapid nucleation and fully packaging (Turner and Butler 1986). In a comparative study with the temperature-sensitive TMV mutant Ni 2519 it was proposed that loops B and C guide the specific recognition of CPs by the cooperative binding of the successive second and third disk (Zimmern 1983).

Such structural motifs have also been identified in RNA genomes of various viruses like the red clover necrotic mosaic virus (RCNMV) (Sit et al. 1998) and the bacteriophage MS2 (Stockley et al. 2007), which serve as packaging signals or origin of assembly to encapsidate the virus genome with its CPs. As it was already shown in the 1950s for ssRNA viruses like TMV (Fraenkel-Conrat and Williams 1955) and cowpea chlorotic mottle virus (CCMV) (Bancroft and Hiebert 1967), TMV

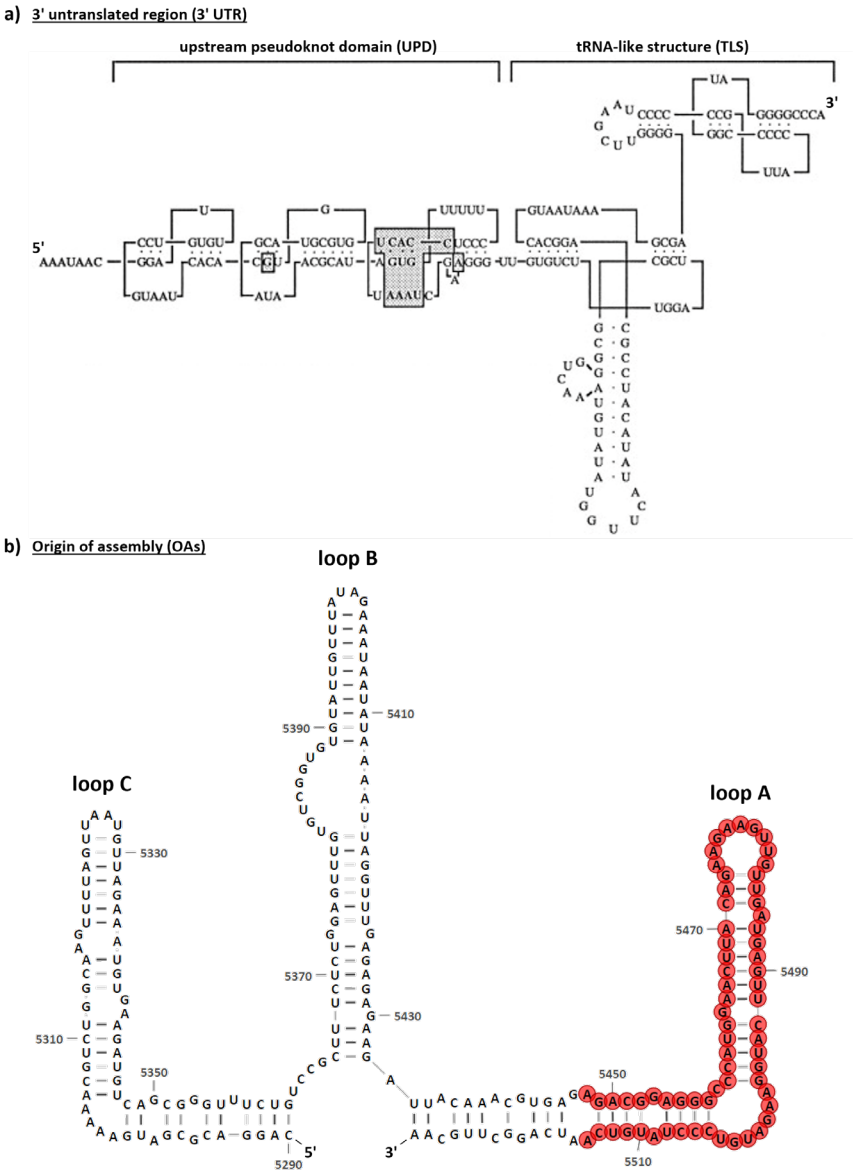

Figure 2-2 Secondary structure representation of two important structural motifs of TMV-RNA. **(a)** 3' untranslated region (3'UTR, nt 6211-6395*) comprised of the tRNA-like structure and the adjacent upstream pseudoknot domain (modified according to the Creative Commons Attribution 4.0 International Public License from Tanguay and Gallie 1996). **(b)** Origin of assembly (OAs) sequence (nt 5290-5527*) composed of three symmetrically spaced hairpin structures (loop A, B and C) adapted from Zimmern 1983. The core stem A is highlighted with red outlines. *numbered according to Goelet et al. 1982.

can self-assemble *in vitro* in a spontaneous process driven by interaction between CP disks and RNA (CP-RNA) and between adjacent CP subunits (CP-CP) (Garmann et al. 2014) without the addition of an energy source.

The self-assembly of TMV-RNA with CP into TMV nanotubes is most likely initiated by a double-layered CP disk (with 17 CPs per layer (Durham et al. 1971; Durham and Klug 1971)) at the OAs region of the RNA. The nucleation stem loop A of the OAs interacts with the central channel of the CP disk and becomes embedded in the inner groove formed by adjacent subunits of the disk (Champness et al. 1976) (see the highlighted cutout in ***Fig. 2-3*** for a scheme).

This triggers the conversion of the RNA-disk complex into a two-turn helical arrangement (Butler et al. 1972). The RNA is embedded between the helically arranged disk layers. In addition, it is known that a CP subunit is connected to three RNA nucleotides at the bottom as well as at the top (Jonard et al. 1977). As the longer 5' RNA tail folds back into the inner hole of the disks, both RNA termini are on the same side, namely at the 3' end of the growing particle (Butler et al. 1977; Lebeurier et al. 1977). The nanotube grows at its 5' terminus with cooperative binding of more disks, whereas the encapsidation into the downstream direction is accomplished by A-proteins (see ***Fig. 2-3***). This bidirectional self-assembly is faster into the 5' direction, since at this end, the long RNA cannot disturb the addition of disks, due to the back-folded 5' RNA tail, which is different from the 3' direction (Fukuda et al. 1978; Butler and Lomonossoff 1980). Despite different rates, it is expected that the assembly runs simultaneously in both directions (Fukuda et al. 1980; Fairall et al. 1986). Furthermore, it was shown that a major portion of all RNA scaffolds has formed full nucleoprotein tubes within 5 to 6 min using simple experimental conditions (20 °C, 0.1 M sodium potassium buffer of pH 7) (Butler and Lomonossoff 1980).

TMV-CP can be modified genetically and can still participate in the self-assembly process with TMV-like particles of the same integrity as the wild type (Mueller et al. 2010; Kadri et al. 2011; Geiger et al. 2013). Chemical modification can also be made to CP, which takes place on preformed TMV rods and then heat transforms them into spherical nanoparticles (Bruckman et al. 2014). Other genetic modification such as by insertion of an additional peptide lead to other form factors after assembly e.g. as filamentous network with lengths around 300 nm but varying diameter from 13-18 nm (Love et al. 2015).

Besides the variability of CPs, also the RNA can be manipulated. Although it has been suggested that rapid nucleation as well as efficient and fast packaging requires a G at every third position in the nucleation loop (Turner and Butler 1986), various studies have shown that foreign RNAs and polynucleotides can also be encapsidated by TMV-CP. Independent of whether its genetical

arrangement is similar to the native RNA or not, if the nucleic acid template is shorter or longer, or if heterologous RNA containing the OAs is used – all types can be assembled with CP *in vitro* to nanotubes of respective length and diameter (Cooper 2014; Gaddipati and Siegel 1990; Gallie et al. 1987; Lam et al. 2016; Maharaj et al. 2014; Sleat et al. 1986; Smith et al. 2007; Turner et al. 1989). Nevertheless, it also became clear in some of these studies that assembly efficiency varied due to reduced assembly rates or abortion of the packaging process, likely due to unfavorable, distinct RNA secondary structures (Sleat et al. 1986; Gaddipati and Siegel 1990).

In addition, TMV-CP can also encapsidate polynucleotides, with nascent tube lengths dictated by the polynucleotide length (Schön and Mundry 1984; Lucate and Szuchmacher Blum 2017). An influence of the secondary structure of polynucleotides to be packaged by CPs was suggested in experiments using other viral CPs (Beren et al. 2017). Poly U ranging from 1000 to 9000 nt in length, lacking any secondary structure, was preferentially completely packaged into VLPs by the CCMV (cowpea chlorotic mosaic virus) protein compared to viral RNA. However, there was a clear difference in the particles formed: poly U formed VLPs with a diameter of 22 nm instead of particles with a diameter of 28 nm, which were composed with normal RNA.

The combination of the before-mentioned features of TMV makes it to a well-known and controllable tool for bionanotechnology. However, to obtain virus-like particles with a specific size and defined functionality depending on their application, the secondary structure of the RNA template and the coat proteins used, as well as precise control over the self-assembly of the two individual components, must be considered.

2.2.2 Manipulation of TMV-like nanotube assembly

Regarding applications based on enzyme-cascades it is of great interest to enable a spatially defined arrangement of such cascades on a single carrier particle, which requires various coupling sites on the outer surface given by selectively addressable, different CP variants. Generating stochastically distributed CP species on the outer surface of a nanotube was enabled by preparation of disks with mixed CP by use of CP blends for the assembly. In contrast, mixing two disk preparations each with a different type of CP with OAs-containing RNA is expected to result in stochastically distributed stripes (Eiben et al. 2014; Eiben 2018). Thus, this method cannot produce fine-tuned domains regarding their lengths and positions. Another approach provided particles with two to three domains in a striped pattern with a more predefined position, using a substoichiometric amount of a first CP variant to initiate the self-assembly process, and thereafter, the partially assembled rods were completed by addition of a second CP mutant in high excess (Geiger et al. 2013). A similar

approach of sequential reconstruction was taken to study the nucleation site in different TMV strains, with the very same result, also here TMV nanotubes with three different CP domains were obtained (Fukuda et al. 1980). Moreover, the substoichiometric approach yields only a limited number of domains, at most three, due to the bidirectional assembly with a defined domain around the OAs that depends on the TMV strain used. Another recently published study demonstrates the preparation of two to three different addressable TMV-CP domains immobilized on a gold-coated silicon surface (Brown et al. 2021). Again, a co-assembly approach was used, based on a capsid variant that can self-assemble pH controllably in the absence of RNA.

As it is known that hybridized, cross-linked cDNA segments ranging from 100 to 300 nt stall the encapsidation of a growing TMV nucleoprotein tube site-selectively (Fairall et al. 1986), this idea could be used to combine DNA nanotechnological methods with viral self-assembly. Some studies on bionanotechnology applications have already taken advantage of RNA-DNA base pairing, for example, to drive the self-assembly of RNA into complex nanostructures by DNA helical strands (Wang et al. 2013) or to control a DNA rotational nanomachine by RNA elements (Zhong and Seeman 2006).

A dynamic DNA-controlled RNA-directed self-assembly process for TMV-CP with TMV-RNA was developed, to enable different coupling sites separated in domains with precisely defined length and position (Eber 2012, dissertation, manuscript IV; Schneider et al. 2016). The so-named "stop-and-go technique" uses DNA oligonucleotides as "stoppers" that hybridize sequence-specifically at predefined sites in the TMV-RNA, blocking its encapsidation into TMV-CP at the DNA/RNA hybrid position (schematically depicted in ***Fig. 2-3a***). Besides the part of the stopper, complementary to RNA, it additionally contains of a non-binding overhang as one component of a fuel oligonucleotide pair. This stable but reversible blockage of the partially assembled nucleoprotein tube enables subsequent replacement of the first CP variant. The restart of assembly is initiated using a "release" DNA oligonucleotide fully reverse-complementary to the RNA-binding one, as the second fuel component, so that an adjacent differently addressable CP domain can grow after hybridization-mediated displacement of the stopper strand (see ***Fig. 2-3b***). Hybridization of the stopper and release strands is assumed to begin at the toehold region, triggering branch migration and displacing RNA from the RNA/DNA duplex (Yurke et al. 2000). The efficiency of the toehold was studied and the most efficient lengths and composition were defined (Yurke and Mills 2003; Zhang and Winfree 2009), which were considered for the stop-and-go principle applied to TMV assembly.

For stopping TMV growth in the 5' direction, it is assumed that the DNA/RNA hybrid region is unable to enter the inner channel of the growing nanotube, as suggested in a previous study (Fairall

et al. 1986).The stop-and-go approach was first introduced using two *in vitro* transcribed RNA templates, RNA 2884 and RNA 2253, originating from the TMV sequence and containing its origin of assembly (OAs) (Eber 2012).

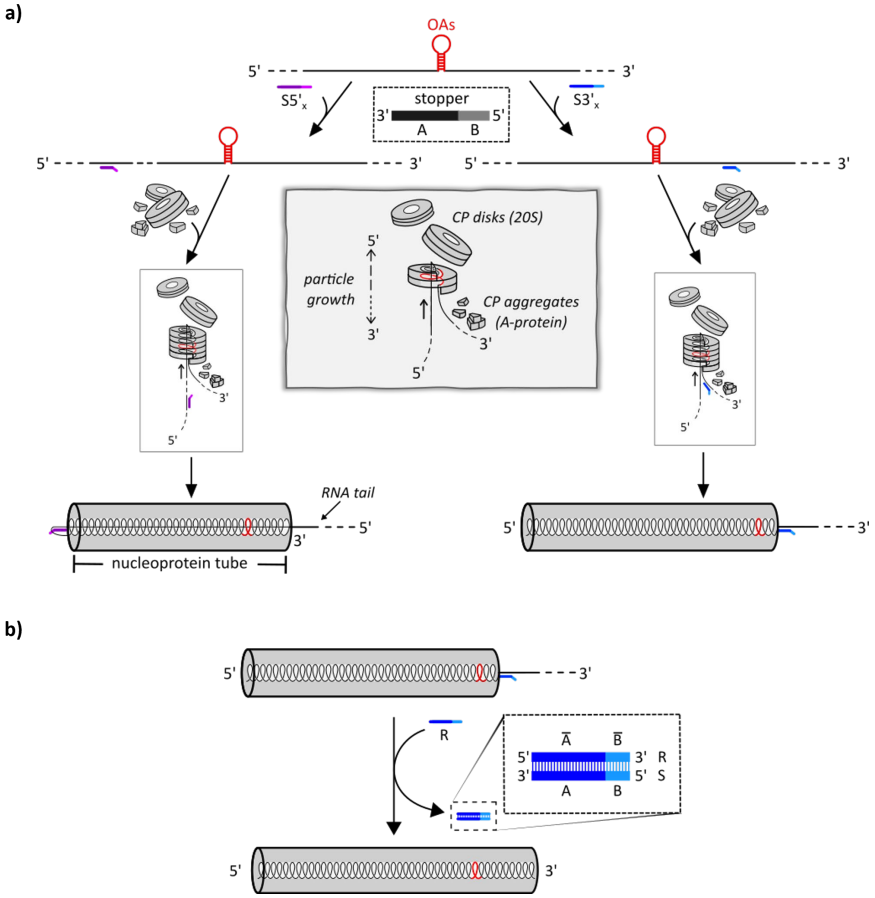

Figure 2-3 Scheme of stop-and-go principle. **(a)** Partial nucleoprotein tube assembly, initiated at the OAs structure (red), arrested by a stopper "S" containing a 3' portion that hybridizes to the RNA scaffold (A), and a 5' non-complementary portion serving as a toehold for the final strand displacement reaction (B, remains accessible to base pairing with a third nucleic acid strand). The highlighted cutout depicts the TMV assembly nucleation initiated at the OAs by a CP disk (for mechanistic details refer to text). **(b)** Restart of assembly after strand displacement reaction initiated by the addition of completely complementary release DNA oligomer "R" in respect of stopper S. Adapted from Schneider et al. 2016 according to the Creative Commons Non-Commercial Attribution 3.0 International Public License.

Two distinct procedures were compared to hybridize four different stoppers to RNA 2884 at their specific sites, 5' or 3' of TMV-OAs, respectively, in 75 mM sodium potassium phosphate buffer (SPP, pH 7.2, supplemented with 3 mM $MgCl_2$).

The following self-assembly of RNA 2884/stopper hybrids with wt-CP showed that only one 3' stopper effectively blocked the self-assembly at its RNA/DNA duplex position. Furthermore, the stop-and-go competence was investigated using 42 °C, 16 h to bind the suitable 3' stopper to RNA 2553, since here, an RNase H assay did not exhibit a difference between two hybridization procedures tested (Eber 2012). The partial encapsidation with wt-CP was performed at 20 °C and the assembly reaction could be restarted by a toehold-mediated displacement of the stopper using a release DNA oligomer, complementary to the stopper. Nevertheless, the conditions used did not reveal fully completed nanotubes after reinitiation of assembly (Eber 2012).

2.3 Purpose of this thesis

The high demand for nanoscaffolds that can provide different ligands at a tunable lateral distance in defined regions has already been presented in section 2.1.2. and 2.2.2. Thus, the major aim of this thesis was to further investigate and refine the stop-and-go technique, to enable the generation of TMV-like nanotubes with differently addressable subdomains of alterable aspect ratios in order to install, *e.g.*, a multienzyme cascade on a single nanocarrier for enhancing the possibilities for various applications. For that purpose, native TMV-RNA was investigated in respect of its stop-and-go competence. In **chapter 4.1** the first proof-of-concept experiments are presented. For that purpose, the reaction conditions established by Eber 2012 were adjusted to an experimentally identified optimum. Furthermore, to clearly monitor the intermediate assembly states during the generation of TMV-like particles with different CP domains (DTLPs), a native gel electrophoretic analysis method was extended. Assembly intermediates were additionally analyzed by transmission electron microscopy (TEM) and revealed reliable statistical data to verify the feasibility of the stop-and-go method to produce length-defined CP subdomains of desired size. Consequently, a protocol was developed to produce TMV-like particles with two domains (2-DTLPs: wt-Lys_{Bio}-DTLPs (261-39 nm)), and exemplarily the 3' terminal $CP_{Lys\text{-}Bio}$ domain was visualized by TEM after decoration of the biotinylated CP portion with avidin conjugates.

Chapter 4.2 presents experiments to demonstrate the universality of dynamic DNA-conrolled RNA-CP assembly. To this end, three distinct heterologous RNA constructs were designed and accessed *in vitro* from accordingly cloned plasmids, each containing the TMV-OAs and

investigated in respect of their stop-and-go capability with stoppers complementary to sequences in the heterologous regions. Although the yields and purity of those nucleoprotein assembly products were low, the results prove the universality of the stop-and-go technique. Major parts of **chapters 4.1 and 4.2** have been published in Schneider et al. (2016) and are mentioned at the relevant passages.

The aforementioned studies exclusively represent stopping at RNA positions 3' from the OAs. This 3' region assembles to 40 nm, which is still a minor part of TMVs overall length (40 nm of 300 nm). Various reasons were discussed, and it seemed to be clear that it is of high importance to overcome the problems. In **chapter 4.3**, different conditions of the stop-and-go assembly are thus presented to facilitate 5' stopping, *e.g.*, varying the hybridization procedure or assembly temperature, comparing the stopper design. A software-based simulation of the stopper target sites was carried out, aiming at a better prediction of suitable stopper binding sites. Those calculations are correlated with experimental results.

Previous studies indicate the high utility of TMV as carrier rods for enzymes, which have been successfully applied in biosensors (Koch et al. 2015; Bäcker et al. 2017; Koch et al. 2018). A recently submitted article based on the work of this thesis could visualize the enzymatic activity of only a few quinoprotein glucose dehydrogenase (PQQ-GDH) enzymes bound antibody-mediated to the 3' terminal domain of a 2-DTLP (Cys-Cys$_{Bio}$-DTLPs (261-39 nm)) by scanning electrochemical atomic force microscopy (AFM-SECM) (Paiva et al. 2022).

The development of TMV domain particles as novel nanocarrier systems offers versatile opportunities to produce synthetic enzyme cascades, *e.g.*, for point-of-care assay devices or for basic analysis for example *via* AFM-SECM. Since in this work, single sequences could be identified that allowed two stoppers to hybridize simultaneously to TMV-RNA but selectively detach one after the other, the production of TMV-like particles with three domains (3-DTLPs) was therefore investigated as a major challenge. It was indeed possible to generate 3-DTLPs, most interesting with a view to applications as scaffolds for artificial multienzyme complexes or in multiplex biosensors. For this purpose, enzymes or antibodies were coupled to single domains and analyzed by colorimetric glucose detection (Koch et al. 2015) or *in situ* atomic force microscopy performed in the lab of our cooperation partner, Dr. Christophe Demaille at the University of Paris-Diderot, Laboratoire d'Electrochimie Moléculaire, CNRS, Paris. The performed experiments are illustrated in **chapter 4.4**.

3 Materials and Methods

3.1 Materials and instrumentation

All commercial materials were used according to the manufacturer's instructions, unless otherwise stated. Buffers and solutions were prepared with ultrapure water (H_2O, 18.3 MΩ cm), and are detailed at relevant passages. The following overview lists suppliers of typically used materials and instrumentations; exceptions are stated in the relevant sections.

Material	**Supplier**
(Bio)chemicals	Carl Roth (Karlsruhe, Germany)
Amicon® Ultra-0.5 centrifugal filter devices	Merck/Millipore (Darmstadt, Germany)
Avidin, GOx, ABTS	Sigma-Aldrich (Saint Louis, USA)
Clear F-bottom 96-well polystyrene (# 655061);	Greiner Bio-One (Frickenhausen, Germany)
Coomassie Brillant Blue R250	Serva Electrophoresis (Heidelberg, Germany)
Functional linkers	Thermo Scientific (Rockford, IL, USA)
MEGAscript® High Yield Transcription Kits	Ambion (Austin, USA)
Oligonucleotides	Biomers (Ulm, Germany)
Restriction enzymes	New England Biolabs (NEB; Ipswich, USA)
RNase H	Roche Applied Science (Mannheim, Germany)
Streptavidin-conjugated HRP (#SM1C)	SDT (Baesweiler, Germany)

Instrumentation	**Supplier**
Nanowizard II microscope (AFM)	(JPK, Germany)
Biometra TAadvanced Twin thermocycler	Analytik Jena GmbH (Jena, Germany)
ChemiDoc Imaging System	Bio-Rad Laboratories (Hercules, USA)
membraPure system	Aquintus (Bodenheim, Germany)
NanoDrop 1000 Spectrophotometer	ThermoScientific (Wilmington, USA)
SpectrafluorPlus	Tecan Group AG (Männedorf, Schweiz)
Tecnai G2 Sphera (TEM)	(FEI, Eindhoven, Netherlands)
Thermomixer F 1.5	Eppendorf AG (Hamburg, Germany)
Ultracentrifuge Optima L90K	Beckman Coulter GmbH (Krefeld, Germany)

3.2 Methods

3.2.1 UV-Vis spectroscopy

The concentration and purity of RNAs, nucleoprotein tubes and CP preparations were determined using a NanoDrop 1000 Spectrophotometer. In detail, the concentration was calculated by assuming an A_{260} of 1 for 40 µg mL^{-1} RNA. The concentration of nucleoprotein tubes and CP were estimated with the extinction coefficients $\varepsilon_{TMV,260}$ = 3 mL(mg cm)$^{-1}$ or $\varepsilon_{CP,280}$ = 1.3 mL(mg cm)$^{-1}$, respectively.

3.2.2 Ultracentrifugation

To purify from residual educts, concentrate the sample or to change the buffer, the desired products (partially/fully assembled TLPs, linker- or enzyme coupled TLPs) were separated from the preparation mixture *via* ultracentrifugation (UC) if not otherwise stated. The samples were transferred to 1.5 mL UC tubes and filled up to 250 µL with 10 mM SPP if the volume was < 250 µL. All nanotube preparations were centrifuged in the 45 Ti rotor of Optima L90K at 4 °C in 1.5 mL UC tubes in corresponding adapters. After centrifugation, the supernatant was removed, the pellet was washed carefully with H_2O and finally resolved in 10 mM SPP at 10 °C, 600 rpm, for at least 2 h, for at most 16 h. Samples were subsequently stored at 4 °C until further use. With this method – at various *g*-force and time regimes – macromolecules with specific sedimentation coefficient were sedimented from the sample (for an overview see ***Tab. 3-1***).

Table 3-1 Sedimentation coefficients of molecules that will be sedimented in the 45 Ti rotor in Optima L90K (Beckman Coulter, GmbH) and averaged *g*-force using rotor parameters according to manufacturer's manual.

Sedimentation coefficient (S) [a]	Rotational speed (rpm)	Time (min)	*g*-force (averaged) [b]
≥ 88	39 000	120	118 991 *g*
≥ 89	45 000	90	158 420 *g*
≥ 95	38 000	120	113 000 *g*
≥ 110	35 000	120	95 834 *g*
≥ 116	34 000	120	90 500 *g*
≥ 146	35 000	90	95 834 *g*

[a] S was calculated as a ratio of time and k-factor, $k = (\ln(r_{max}/r_{min})/\omega^2)*(10^{13}/3600)$ with maximal radius r_{max} = 103.8 mm, minimal radius r_{min} = 35.9 mm, angular velocity of the rotor in radians per second ω = 0.1047*rpm; [b] averaged *g*-force (equates to RCF: relative centrifugal force) calculated *via* RCF = 112 r_{av} (rpm/1000)² with averaged radius r_{av} = 69.8 mm

3.2.3 Preparation of tobacco mosaic virus (TMV) variants and its coat protein (CP)

wt-TMV particles as well as TMV mutants, TMV_{Cys} (S3C) and TMY_{Lys} (T158K) (Geiger et al. 2013), were isolated from systemically infected *N. tabacum* "Samsun" nn plants. 1-butanol extraction and poly ethylene glycol (PEG) precipitation were applied to the homogenized leaf tissue according to Gooding and Hebert (1967), described in detail by Chapman (1998). The isolated nanotubes were sedimented by UC in the 60 Ti rotor of Optima L90K at 120 000 *g*, 4 °C for 90 min. The pellet was resolved and diluted to preparations of 10 mg mL^{-1} in 10 mM sodium potassium phosphate buffer (SPP, pH 7.4).

The additional cysteine residue of CPs on the outer surface of TMV_{Cys} was covalently conjugated with a maleimide-PEG_{11}-biotin linker (EZ-Link™ Maleimide-PEG_{11}-Biotin) as described (Koch et al. 2015). TMV_{Lys} exposes an accessible amino group on the surface of every CP subunit that was functionalized by a succinimidyl-(NHS-)PEG_{12}-biotin-linker (EZ-Link™ NHS-PEG_{12}-Biotin). TMV_{Cys} and TMV_{Lys} were incubated with the respective biotin-linker in a 22-fold and 11-fold molar excess over CP mutant, respectively, at 22 °C, 3 h under gently shaking at 400 rpm in a thermomixer. Non-conjugated biotin-linkers were removed by UC (95 834 *g*, 2 h). The coupling efficiencies were monitored by sodium dodecylsulfate polyacrylamide gel electrophoresis (SDS-PAGE) (Laemmli 1970) and was determined densitometrically by Image J software (Rasband 1997-2011). wt-CP and CP_{Cys} as well as the biotinylated CP variants, $CP_{Cys\text{-}Bio}$ and $CP_{Lys\text{-}Bio}$, were prepared from the corresponding virion samples using an acetic acid-based protocol as reported (Fraenkel-Conrat 1957). CPs in concentrations ranging from 5-10 mg mL^{-1} in 75 mM SPP (pH 7.2) were incubated directly adjacent for at least 48 h at room temperature (RT), to induce 20 S disk formation (Butler 1972).

3.2.4 Preparation of wt-RNA and hRNA scaffolds

wt-RNA was extracted from a plant-derived TMV preparation by a phenol : chloroform : isoamylalcohol (PCI, 25:24:1)-based method (Chapman 1998), followed by precipitation in 0.1 volume of 3 M sodium acetate (NaOAc, pH 5.3) and 2.5 volumes of ethanol for 15 min at −20 °C. To yield pure RNA, after centrifugation (15 min, 20 000 *g*, 4 °C) the pellet was washed with 100 µL 70 % ethanol. The resolved RNA samples were stored in dimethyl dicarbonate (DMDC)-treated H_2O at -80 °C in 20 µL aliquots of 1 µg μL^{-1}.

In addition to the wt-RNA, three types of RNAs each containing TMV-OAs and different heterologous (non-TMV) portions were produced and named hRNA I–III (heterologous RNA I-III, see ***Fig. 3-1*** for the respective constructs) as published in Schneider et al. (2016).

Briefly, the DNA template for hRNA I is based on a cDNA containing the major sequence portion of the TMV-OAs (Zimmern 1983) (nt 5350–5531 according to (Goelet et al. 1982)) inserted into pGEM®-T Easy vector (Promega, Mannheim, Germany), kindly provided by Klara Altintoprak, Stuttgart. After plasmid linearization with DraIII-HF, *in vitro* transcription of ≈ 300 ng linearized template was performed using MEGAscript® T7 High Yield Transcription Kit according to the manufacturer's instructions at 37 °C, 19 h (to improve the yield for short constructs), subsequent treatment with TURBO DNase and final lithium chloride (LiCl) precipitation. A T7 RNA polymerase transcription terminator region (Jeng et al. 1992) was identified at positions 1262–1301 of the pGEM® plasmid sequence (see Promega Corporation product information sheet # 9PIP256, revised version 8/13, Madison, USA). Hence, a mixture of two RNA fragments were yielded after *in vitro* transcription and is referred to as hRNA I: the pre-maturely terminated product of 1262 nt, and a read-through RNA of 2748 nt.

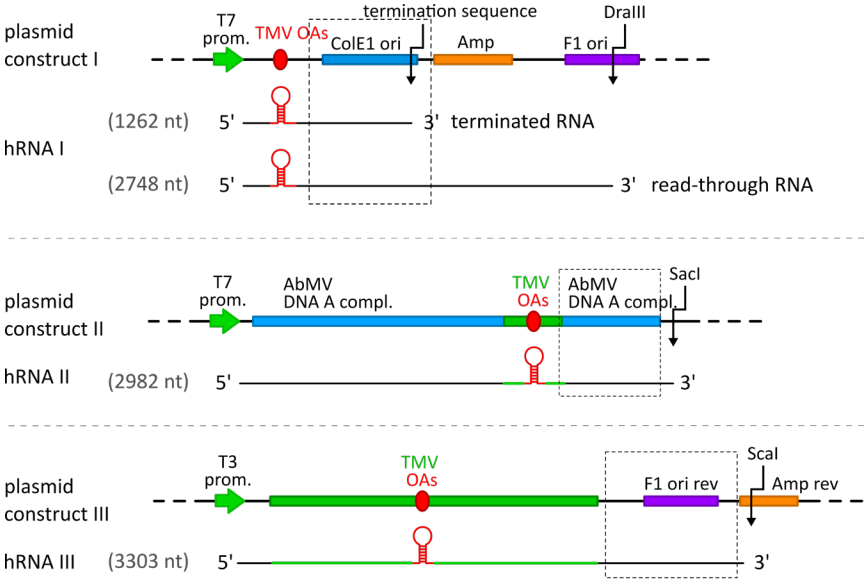

Figure 3-1 Plasmid constructs for *in vitro* transcription to produce the heterologous non-TMV-RNAs (hRNAs). Segments between the relevant T7 or T3 RNA polymerase promoter and the restriction sites used for linearization of the plasmids are shown. Residual TMV sequences are colored green with the OAs in red. Heterologous coding and non-coding sequences of prokaryotic and eukaryotic origin are colored individually (common abbreviations of plasmid elements are used). AbMV DNA A: Abutilon mosaic virus genomic DNA A. Below each plasmid construct, the expected RNAs are depicted in 5' to 3' orientation, with the lengths of the different sequence elements indicated. Boxes indicate binding regions of stopper and are detailed in ***Fig. 4-8a***. Drawings are not in scale. Adapted from Schneider et al. 2016 according to the Creative Commons Non-Commercial Attribution 3.0 International Public License.

To obtain the plasmid construct II, the cDNA of the TMV-OAs (comprising TMV nt 5211–5584, including the OAs) was inserted into the Abutilon mosaic virus (AbMV; EMBL accession number X15983) sequence of a clone (based on the vector pLITMUS28i (NEB)), kindly provided by Tatjana Kleinow, Stuttgart. The resultant template was linearized with SacI-HF followed by *in vitro* transcription of ≈ 300 ng linearized template with T7 RNA polymerase (using MEGAscript® T7 High Yield Transcription Kit, incubation: 37 °C, 4 h; TURBO DNase treatment and LiCl precipitation) to produce hRNA II of 2982 nt.

The plasmid construct for hRNA III was created from a partial TMV cDNA (comprising TMV nt 4253–6398, including the OAs) and inserted into pBlueScript II SK(+) (Agilent Technologies, Santa Clara, USA). The final template construct was linearized with ScaI-HF, and ≈ 300 ng linearized template was *in vitro* transcribed by T3 RNA polymerase using a MEGAscript® T3 High Yield Transcription Kit (incubation: 37 °C, 4 h; TURBO DNase treatment and LiCl precipitation). The desired hRNA III was 3303 nt in length. All RNA constructs were stored in aliquots of 1 µg/µL in DMDC-treated H_2O at -80 °C.

3.2.5 Stopper design, characteristics, and handling

Stopper DNA oligomers (referred to as stoppers regardless of whether they arrested the assembly or not) were designed using the guidelines adapted from PCR primers (Dieffenbach et al. 1993) and strand displacement reactions (Zhang and Seelig 2011; Yurke et al. 2000). Stopper sequences were selected avoiding secondary structures and self-dimerization (Kibbe 2007). The melting temperatures for RNA/DNA hybrids were calculated with the nearest-neighbor two-state-model, thermodynamic parameters (Sugimoto et al. 1995) and salt correction (Owczarzy et al. 2004; Owczarzy et al. 2008). Toehold overhangs of all stoppers, and the complementary portion in the release DNA strands were identical and 8 nt long as it was suggested for strand displacement reactions (Zhang and Winfree 2009; Yurke and Mills 2003). For an overview of sequences and characteristics of stoppers see ***Tab. 3-2***.

The purchased oligonucleotides were resolved in DMDC-treated H_2O according to manufacturer's instruction to result in a stock-solution of 100 pmol/µL. The stock-solution was stored at -80 °C. Working solutions of all stoppers and release DNA oligomers were prepared as aliquots of 10 pmol/µL diluted in DMDC-treated H_2O and stored at -20 °C for at maximum five thaw-and-freeze cycles.

Table 3-2 Sequences and characteristics of the stoppers as well as release DNA oligomers used for the RNA-directed self-assembly of TMV-CP. Asterisks (*) replace the linked toehold sequence (CTGACTTC), identical for all stoppers. Sequences serving as reverse-complementary toehold release portions are underlined.

Name	Sequence (5' > 3')	T_m (°C) [b]	%GC	Binding region		Tube length (nm) [d]	target
				length (nt)	position [c]		
5' stopper [a]							
S5'$_9$	*GTCCCTTGAACAGATGCGATGC	63	55	22	405 - 426	281	
S5'$_8$	*TGATGTTCGCATGTCTGGAAAG	61	45	22	613 - 634	271	
S5'$_7$	*AAAGGTCAACTTGTCTCCATCG	60	45	22	827 - 848	261	
S5'$_6$	*TCCCAAACGCCAGTGAAATCTC	63	50	22	1527 - 1548	228	
S5'$_5$	*AGATTCGACACCGCAGCAGATAG	64	52	23	2217 - 2239	196	wt-RNA
S5'$_4$	*GGGTTTCAAGGTCAATAGCAGC	61	50	22	2262 - 2283	194	
S5'$_3$	CCGAGAGTGGCCTCGTCGGCTCTTTCCATCC*	79	65	31	5189 - 5219	56	
S5'$_2$	GAGTGGCCTCGTCGGCTCTTTC*	75	64	22	5194 - 5215	56	
S5'$_1$	GGTGGTTATAGCATAATTGGGA*	59	41	22	5268 - 5289	52	
3' stopper [a]							
S3'$_1$	*CTCTTTTTCCCGGTTCGAGATCG	66	52	23	5533 - 5555 1348 - 1370	261 64	wt-RNA hRNA III
S3'$_2$	*CGGCGACAGTAGCCTCCGAATC	66	64	22	5671 - 5692	267	
S3'$_3$	*ACAAGAACACGAACTGAGATGG	60	45	22	5733 - 5754	270	
S3'$_4$	*CGCTGATGACAAGAACACGAACTG	63	50	24	5739 - 5762	270	
S3'$_5$	*TTAACTCTATTGGATCGGCCCACG	64	50	24	5761 - 5784	271	wt-RNA
S3'$_6$	*CAGGACTAGAGGTCCAAACCAAACC	61	52	25	6159 - 6183	290	
S3'$_7$	*GCATCTTGACTAGCTCAAGTTGCAGGACTAGAGGTCC	76	51	37	6169 - 6205	290	
S3'$_8$	*CTTGACTAGCTCAAGTTGCAGGAC	64	50	24	6178 - 6201	291	
S3'$_9$	*GCATCTTGACTAGCTCAAGTTGC	65	47	23	6183 - 6205 1998 - 2020	291 95	wt-RNA hRNA III
S3'$_{t1}$	*TGCCTGCGGATGTATATGAACC	62	50	22	6323 - 6344	297	
S3'$_{t2}$	*GCTTTATTACGTGCCTGCGGATG	64	52	23	6333 - 6355	298	wt-RNA
S3'$_{t3}$	*CCTCGCTTTATTACGTGCCTGC	63	54	22	6338 - 6359	298	
h-S3'$_1$	*GTGCGGGCCTCTTCGCTATTAC	63	59	22	2345 - 2366	111	
h-S3'$_2$	*CGTGGCGAGAAAGGAAGGGAAG	63	59	22	2511 - 2532	118	hRNA III
h-S3'$_3$	*GCCCACTACGTGAACCATCACC	63	59	22	2629 - 2650	124	
h-S3'$_4$	*GACCGAGATAGGGTTGAGTGTTG	60	52	23	2732 - 2754	129	
hI-S3'$_1$	*CGGGTTTCGCCACCTCTGACTTG	64	61	23	769 - 791	37	
hI-S3'$_2$	*ATAGTCCTGTCGGGTTTCGCCAC	62	57	23	779 - 801	37	
hI-S3'$_3$	*AGGTATCCGGTAAGCGGCAG	60	60	20	858 - 877	41	hRNA I
hI-S3'$_4$	*TTCCCGAAGGGAGAAAGGCGGAC	65	61	23	878 - 900	42	
hI-S3'$_5$	*CTACAGCGTGAGCTATGAGAAAG	56	48	23	909 - 931	43	
hII-S3'$_1$	*ACTCCTGCATCTCCTCGGGAACG	64	60	23	2187 - 2209	103	
hII-S3'$_2$	*AATAATCATCCGCCCACTCCTGC	61	52	23	2202 - 2224	104	
hII-S3'$_3$	*GTGCCCACATCGTCTTCCCTGTC	63	60	23	2289 - 2311	108	hRNA II
hII-S3'$_4$	*AGCTTTAGATAGTGCGGTGCGAC	61	52	23	2404 - 2426	113	
hII-S3'$_5$	*TTGAGAGTCCAGTTGCGTAGACC	60	52	23	2587 - 2609	122	
Release oligo							
R3'$_1$	CGATCTCGAACCGGGAAAAAGAG GAAGTCAG	69#	-	-	-	-	S3'$_1$
R3'$_5$	CGTGGGCCGATCCAATAGAGTTAA GAAGTCAG	69#	-	-	-	-	S3'$_5$
R3'$_9$	GCAACTTGAGCTAGTCAAGATGC GAAGTCAG	68#	-	-	-	-	S3'$_9$
h-R3'$_1$	GTAATAGCGAAGAGGCCCGCAC GAAGTCAG	71#	-	-	-	-	h-S3'$_1$
hI-R3'$_3$	CTGCCGCTTACCGGATACCT GAAGTCAG	70#	-	-	-	-	hI-S3'$_3$
hII-R3'$_5$	GGTCTACGCAACTGGACTCTCAA GAAGTCAG	69#	-	-	-	-	hII-S3'$_5$

[a] indicate the binding site on the RNA relative to the OAs position; [b] nearest neighbor calculation with parameters for RNA-DNA hybrids, salt correction with 75 mM Na^+ and 1.5 mM Mg^{2+}, oligo concentration estimated with 700 nM; #calculation with parameters for DNA–DNA hybrids (Allawi and SantaLucia 1997), salt correction with 75 mM Na^+, oligo concentration estimated with 7 µM; [c] in respect of the RNA sequence; [d] expected tube length estimated for respective scaffold in the presence of the particular stopper (mean position).

3.2.6 Hybridization of stoppers

Hybridization of stoppers to RNA was performed in 75 mM SPP (pH 7.2) supplemented with 1.5 mM $MgCl_2$. Unless otherwise stated, 3.5 µM DNA oligomers (stoppers) were hybridized to 140 nM RNA (corresponding to a 25-fold molar excess of stopper over RNA). A typical reaction volume for gel evaluation was 7 µL composed of 2.2 µL RNA (1 µg/µL), 1.1 µL SPP-$MgCl_2$-solution (500 mM SPP, 10 mM $MgCl_2$), 2.45 µL stopper (10 pmol/µL) and 1.3 µL DMDC-treated H_2O. The standard hybridization procedure included an initial denaturation for 5 min at 65 °C with a subsequent linear temperature gradient (0.1 °C s^{-1}) to 30 °C (total cooling time: 350 s), performed in a thermocycler, and a subsequent storage on ice until further use for at maximum 10 min as published in Schneider et al. (2016). If a longer storage was necessary, the sample was stored at -20 °C for at maximum four weeks. The following hybridization procedures were evaluated and identified at relevant passages: (1) 25 °C, 2 h and (2) 30 °C, 2 h.

3.2.7 Stop-and-go assembly

For RNA-directed *in vitro* assembly, 0.2 µg $µl^{-1}$ (final concentration, f.c.) of RNA (mass fraction w_{RNA} = 0.05 %) hybridized with stopper were mixed with 3.8 µg $µl^{-1}$ (f.c.) of wt-CPs (mass fraction w_{CP} = 0.95 %). For this purpose, typically 7 µL of the hybridization mixture, containing 2 µg RNA, as detailed in ***section 3.2.6*** was incubated with 4 µL CPs (10 mg/mL) at 25 °C or 15 °C for 3 h in a thermocycler, unless otherwise stated. Reactions were stopped by cooling on ice and stored at 4 °C for further procedure.

For toehold-release of stoppers after their hybridization to RNA and after partial nanotube reconstitution, a 10-fold molar excess of the complementary release DNA oligomer (35 µM) over the stopper was added and incubation performed at 25 °C for 3 h in a thermocycler, if not otherwise stated as published in Schneider et al. (2016). To this end, usually 5.5 µL of the before prepared sample of partially assembled nanotubes was mixed with 1.2 µL release DNA strand (20 pmol/µL). The samples of partially and fully assembled nanotubes were prepared for native agarose gel electrophoresis and transmission electron microscopy (TEM).

3.2.8 Stop-and-go fabrication of TLPs with two or three CP subdomains (2-DTLPs, 3-DTLPs)

For various purposes, nucleoprotein tubes with up to three domains were produced mediated by different stoppers. Preparation conditions as well as details of the distinct domains are listed in ***Table 3-3*** for the individual samples. The prefixed abbreviations depict the CP types and the numbers in brackets indicate the length of the individual domains in nm. wt-RNA served as scaffolds

for all types of DTLPs. Stopper S3'$_1$ was applied in a 5-fold molar excess over RNA, whereas other stoppers were added in 25-fold molar excess, detailed in ***section 3.2.6***. Stop-and-go assembly was processed using concentrations as described in ***3.2.7***. CP amounts for the second and third domain were calculated to 1.5-fold assembly excess over the remaining RNA tail. To develop a purification procedure using UC, wt-Cys$_{Bio}$-DTLPs (261-39) were prepared. The intermediate assembly products, prior and after UC, as well as supernatants and resolved pellets were analyzed *via* native gel electrophoresis (for centrifugation steps and conditions see ***Table 3-3***). The final preparation was applied to bio-affinity coupling with avidin or streptavidin-conjugated glucose oxidase ([s]-GOx) (for protocol see ***section 3.2.9***) and analyzed *via* TEM. An advanced stop-and-go protocol including purification steps *via* UC (for details see ***Table 3-3***) was developed to fabricate wt-Lys$_{Bio}$-DTLPs (261-39) and the 3' terminal domain was visualized using bio-affinity coupling of avidin, detailed in ***section 3.2.9*** *via* TEM as published in Schneider et al. (2016).

Table 3-3 Conditions of preparation and details of the distinct domains of DTLP types. The prefixed abbreviations depict the CP types and the numbers in brackets indicate the length of the individual domains in nm.

		2-DTLPs		3-DTLPs	
	DTLP name	**wt-Cys$_{Bio}$** (261-39)	**wt-Lys$_{Bio}$** (261-39)	**Cys-wt-Lys$_{Bio}$** (261-30-9)	**Cys-wt-Lys$_{Bio}$** (72-199-29)
	Stopper name	S3'$_1$	S3'$_1$	S3'$_1$:S3'$_9$	S5'$_6$:S3'$_5$
	Hybridization	65 °C → 30 °C (0.1 °C/s)		65 °C → 30 °C (0.1 °C/s)	30 °C, 2 h
assembly I	T_{ass} (°C)	25	25	25	15
	CP type	wt-CP	wt-CP	CP$_{Cys}$	wt-CP
	length* (nm)	261	261	261	199
	domain site$^{\#}$	5'	5'	5'	center
	UC	90 500 *g*, 2 h	113 000 *g*, 2 h	113 000 *g*, 2 h	158 420 *g*, 1.5 h
assembly II	T_{ass} (°C)	25	25	25	25
	release [a]	R3'$_1$	R3'$_1$	R3'$_1$	R3'$_5$
	CP type	CP$_{Cys\text{-}Bio}$	CP$_{Lys\text{-}Bio}$	wt-CP	CP$_{Lys\text{-}Bio}$
	length* (nm)	39	39	30	29
	domain site$^{\#}$	3'	3'	center	3'
	UC	90 500 *g*, 2 h	90 500 *g*, 2 h	95 834 *g*, 2 h	118 991 *g*, 2 h
assembly III	T_{ass} (°C)	–	–	25	30
	release [a]			R3'$_9$	temp.-induced
	CP type			CP$_{Lys\text{-}Bio}$	CP$_{Cys\text{-}Bio}$
	length* (nm)			9	72
	domain site$^{\#}$			3'	5'
	UC			95 834 *g*, 1.5 h	95 834 *g*, 2 h
	Application	evaluation of purification	bio-affinity coupling, visualization *via* TEM	two-enzyme cascade, colorimetric assay	antibody detection, *in situ* AFM

*length of CP domain; $^{\#}$domain sites in relation to nucleoprotein tube orientation; [a] strand displacement of stopper *via* toehold-mediated release by a complementary DNA strand or temperature-induced.

Two types of 3-DTLPs were generated for uses as differently addressable templates for diverse applications. Cys-wt-Lys_{Bio}-TLPs (261-30-9) were utilized to install a two-enzyme cascade on two of its domains as described in ***section 3.2.10*** and analyzed in a colorimetric assay, detailed in ***section 3.3.6***. In contrast, Cys-wt-Lys_{Bio}-TLPs (72-199-29) served as scaffold for directed immunomarking of the $CP_{Lys\text{-}Bio}$ domain to facilitate subsequent *in situ* atomic force microscopic (AFM) detection of an antibody-decorated subdomain as referred in ***section 3.3.7***.

3.2.9 Bio-affinity coupling of avidin to DTLPs

DTLPs were investigated by TEM to enable the visualization of a decorated CP subdomain. For this purpose, 22 µL (100 µg) of desired 2-DTLPs were incubated at 22 °C for 2.5 h under gentle shaking at 200 rpm in a thermomixer with 45 µL of 2 mg mL^{-1} avidin in phosphate-buffered saline (PBS, 137 mM NaCl, 2.7 mM KCl, 10 mM Na_2HPO_4, 1.8 mM KH_2PO_4, pH 7.4) resulting in a 2-fold molar excess of avidin over biotin-moieties. The unbound biomolecules were excluded by another UC step (90 500 *g*, 2 h).

3.2.10 Preparation of a two-enzyme cascade on Cys-wt-Lys_{Bio}-TLPs (261-30-9)

To investigate whether DTLPs can be applied as a scaffold for a multienzyme complex consisting of groups of enzymes installed on two of three subdomains, glucose oxidase (GOx) and horseradish peroxidase (HRP) were conjugated to the 5' terminal and 3' terminal domains. For that purpose, maleimide-conjugated GOx ([mal]-GOx) was prepared by incubation of 0.24 µL (60 nmol) of a heterobifunctional maleimide-PEG_{12}-NHS linker (10-fold molar excess over GOx) with 96 µL (6 nmol) GOx at 20 °C, 2 h under shaking at 600 rpm in a thermomixer. Subsequently, [mal]-GOx was purified *via* a centrifugal filter device (10 kDa MWCO) according to the manufacturer's protocol. 60 µL (60 µg) Cys-wt-Lys_{Bio}-TLPs (261-30-9) were incubated at 22 °C, 2 h in a thermomixer with 25 µL [mal]-GOx (2.5 nmol) and 22.5 µL of a streptavidin-conjugated ([s])-HRP (216 pmol, commercially traded product), resulting in a one- and two-fold molar excess of enzyme over CP_{Cys} and $CP_{Lys\text{-}Bio}$ domains, respectively. The non-coupled [mal]-GOx and [s]-HRP molecules were separated by UC (95 834 *g*, 1.5 h) and removed with the supernatant. The enriched enzyme-carrying DTLPs were resuspended in 10 mM SPP, 16 h at 10 °C and 600 rpm in a thermomixer and stored at RT for up to 2 h prior determination of enzyme activity (for protocol see ***section 3.3.6***).

3.3 Analytical methods

3.3.1 RNase H assays

Hybridization success of DNA stoppers to the RNA scaffolds as well as their complete removal mediated by a release oligomer in the absence of CP were evaluated with a modified RNase H assay (Donis-Keller 1979). 2 µg of RNA were hybridized with stopper as described in ***section 3.2.6***, in a total volume of 7 µL. The sample was separated into two aliquots, one was stored on ice, whereas the other was incubated with 1.1 µL of the respective release DNA oligomer (10 pmol/µL) that correspond to a 10-fold molar excess over stopper for 4 h at 25 °C in a thermocycler. A control sample lacking a stopper was prepared under the same conditions. Each sample was treated with 3 µL (= 0.3 U) of a freshly prepared DMDC-treated H_2O-diluted RNase H solution for 20 min at 37 °C, followed by heat-inactivation of the enzyme at 65 °C for 20 min in a thermocycler.

3.3.2 Denaturing gel electrophoresis

RNA fragments generated in RNase H assays as well as *in vitro* transcribed RNAs were analyzed in 0.3 M formaldehyde-containing 1% agarose gels (1.5 % agarose gels for hRNAs) in 1 x 3-(N-morpholino)propanesulfonic acid (MOPS) buffer (10x MOPS: 200 mM MOPS, 50 mM NaOAc x $3H_2O$, 10 mM EDTA pH 7.0) with buffer circulation according to standard protocols (Green and Sambrook 2012) as described in Schneider et al. (2016). RNA samples (1 µg) were incubated in 15 µl denaturing solution (1.7 µl 10x MOPS, 9.9 µl deionized formamide, 2.9 µl 37 % formaldehyde, 0.5 µl DMDC-treated H_2O, 0.05 µl 1 % ethidium bromide (EtBr)) for 15 min at 65 °C, supplemented with 1.5 µl loading buffer (1 mM EDTA, 0.4% bromophenol blue, 50 % glycerol) while the gel was pre-run at 3.5 V cm^{-1} for 15 min. Electrophoretic separation was executed at 2.3 V cm^{-1} for 15 min and at 3.2 V cm^{-1} for the remaining time (around 4 h) until the bromphenol blue band had reached the bottom of the gel. An ssRNA molecular weight marker (N0362S, NEB) served as the calibration standard. Agarose gels were imaged by a ChemiDoc Imaging System.

3.3.3 Native agarose gel electrophoresis

Native agarose gel electrophoresis was performed according to an optimized protocol as published in Schneider et al. (2016). Equal amounts of each assembly product were applied to a 1 % or 1.5 % agarose gel (for wt-RNA- or hRNA-directed assembly products, if not otherwise stated) prepared in 50 mM SPP (pH 7.2) and run for 19 h at 1.1 V cm^{-1} with buffer circulation. To identify the residual unencapsidated RNA, buffer as well as gel contained 0.05 % EtBr. EtBr-stained bands were imaged by ChemiDoc Imaging System. Subsequently, to exchange the buffer of the gel, it was

agitated for 30 min in destain solution (10 % (v/v) glacial acid, 40 % (v/v) EtOH) and subsequently, the proteins were stained with 0.1% Coomassie Brillant Blue R250 (in 10 % (v/v) glacial acid, 40 % (v/v) EtOH) for 1.5 h (Green and Sambrook 2012). Finally, the gel was destained by extensive washing with destain solution (exchanged multiple times, each 20-30 min) and a final washing step with H_2O was necessary to achieve an almost transparent background.

Insignificant lanes of the gels were cut off of the images, to illustrate only the relevant parts. In this case the lanes are depicted clearly separated from each other. Each gel image was exclusively compiled out of the same gel compared by both staining methods, respectively (EtBr – left, Coomassie – right). Amounts and/or concentrations of particles were evaluated with the software Image J (Rasband 1997-2011).

3.3.4 Transmission electron microscopy

Qualitative and quantitative analyzes of nanotubes, and the spatial arrangement of domain-TLPs were performed by transmission electron microscopy (TEM). The products were adsorbed to a Formvar©-carbon-coated copper grid and stained 2 min with a solution of 1 % uranyl acetate and 0.25 mg/ml bacitracin (Mueller et al. 2010). The samples were analyzed in a Tecnai G2 Sphera transmission electron microscope (FEI, Eindhoven, Netherlands) at 200 kV with a 16 megapixel camera (TemCam F416R, TVIPS, Gauting, Germany).

3.3.5 Statistical evaluation of products analyzed *via* TEM

Randomly selected positions on the grids were imaged and the lengths of nanotubes readily separated from each other were measured using the Image J software (Rasband 1997-2011). The resultant lengths were classified in 10 nm size classes and three independent assembly experiments were analyzed statistically as outlined in Schneider et al. (2016). The inter-experimental variation and the consistency between repetitions were determined using the non-parametric Mann–Whitney Rank Sum Test for the corresponding size classes. Finally, the length classes were averaged and compiled in histograms with their standard deviations using Microsoft Excel. SigmaStat version 4.0.0.37 (Systat Software, Inc.) was used to execute statistical analyses and boxplot graphs.

3.3.6 Enzyme activity determination of a two-enzyme cascade on 3-DTLPs

The activity of enzymes bound to Cys-wt-Lys_{Bio}-TLPs (261-30-9) (prepared as described in ***section 3.2.8***) was kindly determined by Claudia Koch as described (Koch et al. 2015). Briefly, 100 µL of two differently concentrated DTLP samples (1 ng/µL, 2 ng/µL) were applied to a high-binding microplate. 100 µL of substrate mixture (f.c.: 100 mM glucose, 5 mM 2,2'-azino-bis(3-

ethylbenzothiazoline-6-sulphonic acid) (ABTS), 50 mM NaOAc, pH 5.5) per sample were added and the absorption was determined spectrophotometrically at $\lambda = 405$ nm for 15 min. Concentrations of converted ABTS* were calculated using Lambert-Beer law $c = A\ (d\ \varepsilon_{405})^{-1}$ with detected absorption A_{405}, optical path length $d = 0.625$ cm (fluid level), $\varepsilon_{405} = 36.8$ mM^{-1} cm^{-1} (extinction coefficient of ABTS* according to the supplier) and plotted *versus* time. Control samples of 100 µL with unbound TMV as well as without biomaterial were prepared using equal conditions, and the latter was used to normalize any background absorption. Enzymatic activities of all samples were explored as technical triplicates.

3.3.7 Atomic force microscopic imaging of immune-labelled domains

To visualize individual domains of Cys-wt-Lys$_{Bio}$-TLPs (72-199-29) (prepared as described in ***section 3.2.8***), the sample was subjected to bio-affinity coupling of anti-biotin antibodies (A150-109A, Bethyl Laboratories Inc., Montgomery, TX, USA) and analyzed by AFM under guidance and support of Dr. Christophe Demaille, Dr. Agnès Anne and Dr. Arnaud Chovin at the University of Paris-Diderot, Laboratoire d'Electrochimie Moléculaire, CNRS, Paris, France.

The ultraflat gold surfaces on glass slides were prepared on the basis of a protocol reported in Hegner (1993) and described by Abbou et al. (2004). Adhesive Teflon tape was perforated and then glued to the substrate to provide a circular area (≈ 0.45 cm^2) of bare gold.

The sample preparation, backfilling with bovine serum albumin (BSA) and immunomarking was executed based on protocols previously described (Anne et al. 2018; Patel et al. 2017; Nault et al. 2015). Briefly, a 75 µL droplet of the DTLP sample (28 ng µL^{-1} dilution in 10 mM potassium phosphate buffer (PPB), pH 7.4) was incubated on the bare gold for 15 min at RT. It was washed multiple times with 10 mM PPB and finally with water by drop replacement. The water was removed, and the sample dried on the surface by low nitrogen flow and left in air for 5 min before rehydrating it in 75 µL PPB. The surface was backfilled with BSA (2 mg mL^{-1} in 10 mM PPB), incubated for 30 min at RT, then washed with PPB and left in contact with an anti-biotin IgG (20 µg mL^{-1} with 1 mg mL^{-1} BSA in 10 mM PPB) for 1 h. The sample was rinsed with water prior imaging.

AFM images were recorded *in situ* (*i.e.*, in PPB) by a Nanowizard II microscope (JPK, Germany) with triangular-shaped contact mode probes (MSNL, Bruker, D, spring constant 0.03 N m^{-1}, tip curvature: nom. 2 nm, max. 12 nm) in tapping mode. First degree flattening was applied to the images. Images were analyzed *via* software Gwyddion (http://gwyddion.net/) and JPK SPM data processing (JPK, Germany) and measurements compiled in Microsoft Excel. The height of nanotubes after BSA backfilling was calculated from cross-sections of ≈ 100 objects readily separated

from each other. Heights of the individual domains of DTLPs after immunomarking were determined by taking 5 to 10 particles of each type for the evaluation and averaged over the whole length of each domain.

3.4 Folding simulation and illustration

To investigate the local RNA accessibility, simulations of the secondary structure of RNA at diverse temperature were performed. Full-length wt-RNA was folded *via* the web-based software `RNAfold` (version 2.4.18, http://rna.tbi.univie.ac.at/cgi-bin/RNAWebSuite/RNAfold.cgi; hereinafter referred to as `RNAfold`) (Gruber et al. 2008; Lorenz et al. 2011) at 30 °C, without hard or soft constraints using the *Turner 2004* energy parameter as described in (Lorenz et al. 2011).

To simulate the folding using selectable temperatures, the web server-based application `mfold` (version 2.3, http://www.unafold.org/mfold/ applications/rna-folding-form-v2.php; hereinafter called `mfold`) (Zuker 2003) was used that was limited to sequences up to 2400 nt. Folding was performed without hard or soft constraints using energy parameters as described in Walter et al. (1994) and default settings. Simulations were performed at 30 °C and 65 °C with ionic conditions for RNA that were fixed to 1 M NaCl and no divalent cations. Suboptimal foldings within 5 % from the minimum free energy were estimated.

The secondary structures of all simulations were visualized with the web based RNA2Drawer app (Johnson et al. 2019) using the *Vienna* format.

4 Results

4.1 Stop-and-go technique: Proof-of-concept

Major aim of this thesis was to verify the feasibility of the dynamic DNA-controlled assembly initially demonstrated for a stopper position 3' of the OAs and an *in vitro* transcribed RNA template by Eber (2012, dissertation, manuscript IV) (see ***section 2.2.3*** for further details) for the generation of TMV-like particles with two or three site-specifically defined longitudinal domains of distinct lengths and functionality.

In a first approach, the stop-and-go protocol as well as a convenient analytical method required adjustment to enable, demonstrate and investigate this step-by-step assembly. Preliminary results have shown that the differentiation of background products from assembly intermediates, generated by encapsidation of stopper/RNA hybrids with wt-CP, was more reliable using wt-RNA as a template than *in vitro* transcribed RNAs. Thus, the viability of the stop-and-go procedure was evaluated using wt-RNA isolated from plant-derived TMV.

Some results of the optimized stop-and-go procedure, extensive data for a statistical analysis of the assembly states as well as a proof-of-concept experiment to visualize TMV-like nanotubes with two precisely defined CP domains have been published in Schneider et al. (2016) and are referred to it at the relevant paragraphs.

4.1.1 Hybridization of DNA strands to wt-RNA

To first examine an efficient route to stably hybridize stoppers to the desired position at the RNA, the application of two stoppers, S3'$_1$ and S3'$_2$, designed to bind 3' of the TMV-OAs, was investigated systematically (Schneider et al. 2016). The complementary part of S3'$_1$ and S3'$_2$ to TMV-RNA contains 23 and 22 deoxynucleotides (nt), respectively (see ***Tab. 3-2***). Each stopper is elongated at its 5' side by an additional 8 nt long sequence that is non-complementary to the wt-RNA serving as the toehold for the subsequent strand displacement reaction. In contrast to Eber (2012), hybridization of stoppers to the RNA was performed with an initial denaturation at 65 °C for 5 min, followed by cooling down to 30 °C with a rate of 0.1 °C in 75 mM SPP (pH 7.2) supplemented with a lower concentration of $MgCl_2$ (1.5 mM). To maintain the hybridized state, the mixture was stored on ice until further use.

An RNase H assay was performed with subsequent analysis by denaturing gel electrophoresis, to investigate the hybridization efficiencies at the desired position. Since RNase H cleaves the RNA at the RNA/DNA duplex position, no full-length RNA portion but two smaller fractions will be obtained, up- and downstream of the binding site of the stopper, if binding efficiency is almost 100 %. The site of each stopper in respect to wt-RNA is schematically illustrated in ***Fig. 4-1a*** (see ***Tab. 4-1*** for fragment sizes). Hybridization was examined for two different molar excesses of stopper over RNA, 5- and 25-fold, respectively (***Fig. 4-1b***). A reaction without any stoppers was prepared that showed only one RNA comparable in length to the untreated wt-RNA and confirmed the conditions used do not impact the RNase H assay. A negative control reaction was performed by adding a non-complementary oligonucleotide (C_1) instead of a stopper. This control clearly verified that oligonucleotides without any binding capability have no impact on the reaction as full-length RNA was visualized. The gel analysis revealed that S3'$_1$ hybridized to almost 100 % of RNA and full cleavage was obtained at only 5-fold molar excess over RNA. In comparison, stopper S3'$_2$ required a higher molar excess over RNA to fully bind to RNA as visualized by the two potential fractions 5692 nt and 703 nt, respectively. However, S3'$_1$ showed two additional fractions of hydrolyzed RNA (white asterisks in ***Fig. 4-1b***), besides the expected fragments (5555/840 nt). In a study on the mechanism of RNase H substrate recognition, it was proposed that four adjacent deoxyribonucleotides hybridized to an RNA strand interact with the enzyme, followed by cleavage of the RNA at this position into a 5' phosphate and a 3' hydroxyl (Nakamura et al. 1991). According to this, the sequence of wt-RNA was analyzed in respect of a binding region of S3'$_1$ with a minimum of four successive nucleotides *via* A plasmid editor (ApE, v2.0.61, *http://biologylabs.utah.edu/jorgensen/wayned/ape*). At RNA region 1551-1573, two parts of S3'$_1$ can hybridize (for statistical probability of this second binding site see *Appendix **A1***) with four adjacent deoxyribonucleotides and eight mismatches (strikethrough, greyish nucleotides illustrate mismatches in stopper sequence: 5' CTCT~~T~~TTTC~~C~~CGG~~TTC~~GA~~G~~AT~~CG~~ 3'). Stopper binding to this site 5' of the OAs might result in the two additional RNA fractions (estimated to 1550 nt and 4005 nt) found after RNase H cleavage. However, whether this binding site may result in an additional blocking position during the assembly process requires further investigation (evidence for this additional blocking position was depicted in ***section 4.3.3***).

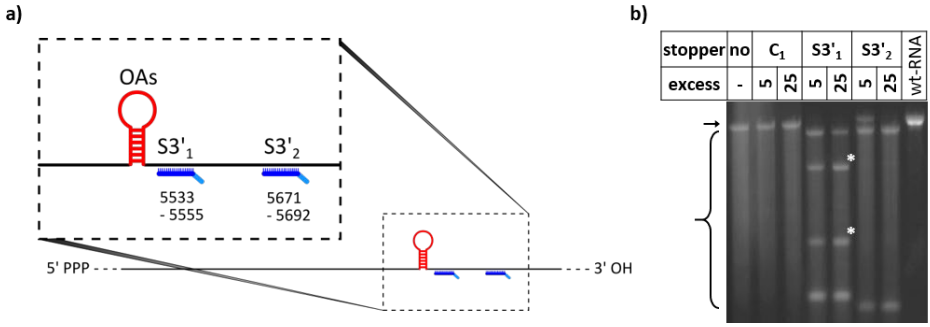

Figure 4-1 Hybridization of stopper DNA oligomers to wt-RNA. **(a)** Scheme of the binding sites of the different stoppers (S3'$_x$) on RNA in relation to the OAs position (symbolized as red hairpin). The dark blue lines represent the stopper portions complementary to the RNA (positions in relation to TMV sequence are indicated below each stopper), and the light blue lines toehold overhangs. Schemes are not to scale. **(b)** Agarose gel electrophoretic separation of the RNA portions after RNase H cleavage of DNA/RNA hybridization products. Fragments were separated on 1% under denaturing conditions. Stoppers were hybridized to the RNA in 5- and 25-fold molar excess, prior to RNase H treatment. The arrow denotes the bands of undigested RNA, and brackets the range of fragments expected after digestion. The white asterisks label additional fragments occurring upon RNase H incubation. Adapted from Schneider et al. 2016 according to the Creative Commons Non-Commercial Attribution 3.0 International Public License.

4.1.2 Impact of stoppers on the self-assembly with CP and visualization of assembly states

To figure out whether and how the RNA-directed self-assembly of nucleoprotein tubes is affected by hybridizing the different stoppers, a CP preparation with preformed 20 S disk formation (Butler 1972) was added to the RNA samples with and without hybridized stoppers, followed by incubation at 25 °C for 3 h (for a scheme see ***Fig. 4-2a***). It was expected that the as-produced TMV-like particles (TLPs) differ in the partially encapsidated nucleoprotein tube size as well as in their length of protruding RNA, depending on the stopper binding site (illustrated in ***Fig. 4-2b***). Hence, the analysis method should depict both, the nucleoprotein tube, and the RNA. To visualize the RNA tail protruding from the incompletely assembled TLPs *via* electron microscopy, spreading of ribonucleic acid and subsequent platin shadowing of assembly products prior transmission electron microscopic (TEM) imaging are required. However, this technique is cost-intensive, time-consuming and the analyses of the protein tube as well as the RNA length require a high number of measured structures. In contrast, a simple, rapid, and inexpensive method to visualize TMV and TMV-like particles including the protruding RNA tail is their separation by gel electrophoresis without prior denaturation of the sample. The native gel electrophoresis in 50 mM SPP (pH 7.2) leads to separation of assembly products in their native form depending on their negative net charge (pI$_{TMV}$ 3.5) (Oster 1951; Alonso et al. 2013) due to the nearly neutral pH of the buffer

system (Hogue and Asselin 1984; Eiben et al. 2014; Geiger et al. 2013). When the particles differ in size but exhibit the same relative net charges (f. e. RNAs of different length fully assembled with wt-CP), smaller ones depict a higher electrophoretic mobility than longer nanotubes. However, when the RNA is incompletely assembled with CP due to a successfully bound blocking element, the unencapsidated RNA enhances the negative net charge of the nucleoprotein complex and thus increases the electrophoretic mobility additionally to its smaller encapsidated domain. Hybridization of different 3' stoppers to a similar RNA type of a defined length in individual samples, followed by partial assembly with CP, resulted after separation in a native gel system in a linear correlation of the differently sized nanotubes with their corresponding varying residual RNA lengths. Hence, this method was adjusted to be able to reliably distinguish the desired fractions. To prevent degradation of the residual RNA of the partially assembled tubes, all experimental procedures were performed using RNase free conditions. Ethidium bromide (EtBr) was added to the whole system (gel and buffers) to visualize the protruding RNA tail of partially encapsidated products as well as the different assembly-incompetent RNA folding states. The gel was run for 19 h with buffer circulation and imaged using a ChemiDoc Imaging system by UV light. Subsequently, the proteins were stained by Coomassie Brillant Blue. Both images were compiled and by comparing the EtBr signal with the Coomassie Brillant Blue staining, the partially assembled tubes were dependably highlighted and differentiated from other assembly products (***Fig. 4-2c***) (Schneider et al. 2016). The longer the residual RNA tail, the higher was the electrophoretic shift in respect of the fully assembled particles without any stopper in the reaction (no, C_1). The full-length of assembled nanotubes was confirmed by a comparison with native TMV particles.

Since the RNase H assays implied that the molar excess of stopper over RNA depends on the individual stopper, *i.e.*, that an optimum of molar excess can shift the equilibrium toward a higher blocking yield, different molar excesses over RNA were also compared for the assembly experiments. Blocking with S3'$_1$ showed a similar trend in respect of the molar excesses as it was observed in the hybridization assay: at ≥ 5-fold molar excess the assembly was almost completely stopped at the desired RNA/DNA duplex position. Furthermore, only one fraction of partially assembled tubes was found under the conditions applied (***Fig. 4-2c***), that means that the second binding site of S3'$_1$ depicted by the RNase H assay did not stall the encapsidation at this position. On the one hand the probability of binding to the 5' position is lower than at the desired 3' position and on the other hand the assembly rate into 5' direction is higher and may lead to shearing off S3'$_1$ bound with eight mismatches at RNA position 1551-1573 under the conditions used here.

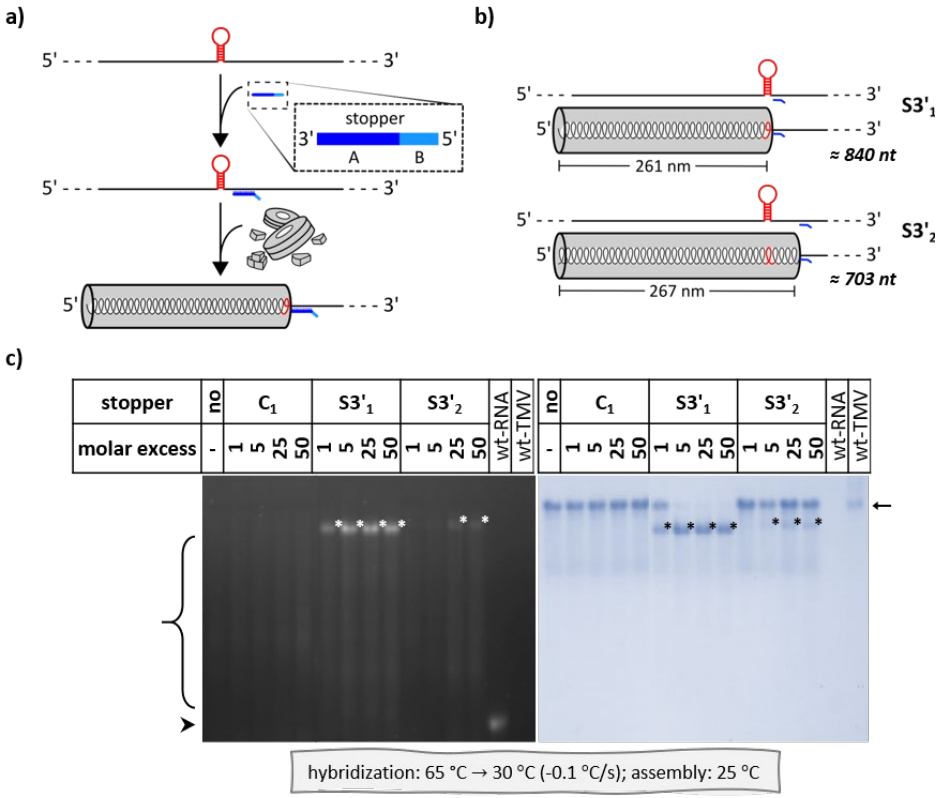

Figure 4-2 Influence of stoppers, S3'$_1$ and S3'$_2$, on the self-assembly of CP with wt-RNA. **(a)** Scheme (not to scale) of partial ribonucleoprotein tube assembly, initiated at the OAs, arrested by a stopper (blue) containing a 3' portion (A) that hybridizes to the RNA scaffold, and a 5' non-complementary portion (B) serving as a toehold. **(b)** Cartoons (not to scale) illustrating the distinct types of stalled nanotubes with a non-encapsidated RNA portion expected to arise upon effective blocking of their assembly by the different stoppers, S3'$_1$ and S3'$_2$, hybridized 3' of the OAs on RNA. **(c)** Nanoparticle separation of the "stopped" products in a native agarose gel in comparison to control reaction products. Two different control samples were prepared: "no", *i.e.*, fully assembled nanotubes scaffolded by RNA devoid of stoppers, and "C$_1$", *i.e.*, fully assembled nanotubes obtained in the presence of a DNA oligomer with no complementarity to the RNA. Hybridization was performed with variable molar excess of stopper over RNA followed by assembly as depicted below the image. TMV and wt-RNA serve as markers. The gel was first stained with EtBr (left), followed by Coomassie Brilliant Blue-staining (right). The arrow (upper right) indicates bands of fully assembled tubes as confirmed by the TMV particles. Black/white asterisks (*) label bands with higher electrophoretic mobility. Bracket depicts non-encapsidated RNA states that are unequal to full-length, native form of RNA (➤). Adapted from Schneider et al. 2016 according to the Creative Commons Non-Commercial Attribution 3.0 International Public License.

The reaction with stopper S3'$_2$ showed a different trend concerning the use of different molar excesses of stopper. Although the RNase H assay implied that the stopper S3'$_2$ was fully hybridized to RNA at 25-fold molar excess, the self-assembly could only be stalled in a minor fraction of growing particles – even at 50-fold molar stopper excess (***Fig. 4-2c***).

To compare the results of RNase H assay and assembly reaction, the gel images were analyzed *via* the software ImageJ (Rasband 1997-2011) and the corresponding percentual yields obtained at a 25-fold molar excess of stopper over RNA were compiled in ***Tab. 4-1***. While the RNase H assay implied 100 % hybridization of both stoppers to the RNA, the assembly reaction resulted in 100 % and 30 % yield of nanotubes stalled by stopper S3'$_1$ and S3'$_2$, respectively. As both, the length as well as the melting temperatures (T_m) of both stoppers are identic (T_m = 66 °C), it is unlikely that the stopper completely binds to the RNA but is sheared off during assembly. It is more presumably that secondary structures of the complementary RNA region, or intermolecular tertiary interactions interfere the amenability of the S3'$_2$ target sequences under the conditions used. Computational folding of a part of the RNA sequence (nt 4396-6395) by `mfold` (version 2.3, at 65 °C, http://www.unafold.org/mfold/applications/rna-folding-form-v2.php) (Zuker 2003) showed that S3'$_1$ target sequence is accessible at a wider single-strand region with 11 successive nucleotides that may mediate the unfolding of the target RNA structure (further details on simulation see ***section 4.3.4***). In contrast, S3'$_2$ interacts only with four adjacent nucleotides to a small hairpin loop of RNA, that is sufficient as a recognition site of RNase H, *i.e.*, the enzyme can cleave the RNA at this position. Hence, RNase H assay is useful to preselect stoppers, but the final functionality can only be evaluated after the assembly reaction.

Table 4-1 Hybridization and blocking efficiencies of stoppers S3'$_1$ and S3'$_2$ hybridized to RNA.

Stopper		Expected RNA length (nt) [b]	Hybridization efficiency [c]	Expected tube length (nm) [d]	Blocking efficiency [e]
name	**position** [a]				
no/C	-	6395	-	300	-
S3'$_1$	5533 - 5555	5555/840	100 %	260	100 %
S3'$_2$	5671 - 5692	5692/703	100 %	267	30 %

[a] in respect of the sequence position in RNA; [b] calculated from binding sites (5'/3' portions); [c] reflected by the amount of cleaved RNA in relation to the non-cleaved RNA deduced from the RNase H assay; [d] estimated for wt-RNA as scaffold in the presence of the respective stopper DNA; [e] equates to the amount of partially assembled products calculated by analyzing nanotube separation in native gels. All amounts were determined at a 25-fold molar excess of stopper over RNA (see in *Appendix **A2*** for details).

The adjusted native gel system with SPP in combination with EtBr illustrated also differences of folding states of non-encapsidated RNAs that were unequal to the secondary structure of full-length, native RNA (***Fig. 4-2c***). Identification of the various folding states was not possible, but relative and quantitative changes were visualized. As the stoppers were hybridized at 65 °C and during slow cooling down to 30 °C, the RNA was only partially denatured prior assembly. This procedure may generate assembly-incompetent secondary and/or tertiary structure formation of RNA that did not participate in the assembly reaction. Furthermore, the RNA may also be degraded to some extent, and shorter segments containing the OAs, assemble into smaller tubes with low Coomassie Brillant Blue signal.

Based on these findings, comparison of different hybridization procedures to bind S3'$_1$ to RNA (65 °C, 5 min; 50 °C, 5 min; 42 °C, 16 h) and distinct concentrations of the supplemented $MgCl_2$ (0, 1.5, 3 mM) as well as defined assembly temperatures (15, 20, 25 °C) were tested in respect of the final yield of blocked nanotubes. It was shown that the assembly-competence was dependent on the hybridization procedure since different but reproducible EtBr signals and distinct total assembly yields for the various protocols, respectively, were found (data not shown). However, the highest blocking yield of S3'$_1$ was achieved after binding the stopper to RNA after a partial denaturation step at 65 °C in 75 mM SPP, supplemented with 1.5 mM $MgCl_2$ followed by assembly at 25 °C as described in the previous section. Indeed, it was found that different stoppers require individual conditions to provide optimal blocking results. Further evaluation of the conditions for individual stoppers are described in **Chapter 4.3**.

To confirm the results of native gel analysis that S3'$_1$ blocked the assembly efficiently at the desired position to produce one domain of the expected length, the assembly reaction products in the presence or in the absence of S3'$_1$ were explored by TEM. Mainly straight tubes were determined in both samples. Most particles were about 30-40 nm shorter in the presence of stopper S3'$_1$ (stop, ***Fig. 4-3***) than the fully assembled nanotubes in the control sample (no). The reduced length of around 260 to 270 nm verifies the expectations for an S3'$_1$ binding site-specific stalling of the assembly (Schneider et al. 2016).

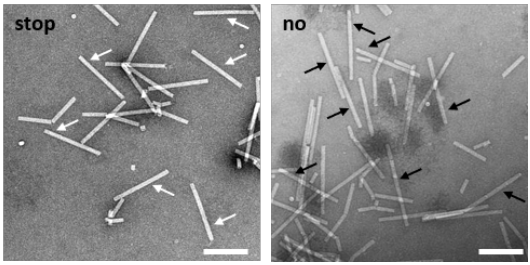

Figure 4-3 Visualizing the "stop" state of TLP assembly in the presence of stopper S3'$_1$ hybridized to wt-RNA during the self-assembly with wt-CPs. TEM analysis of the respective nanotubular products. "stop": partial, stalled assembly directed by S3'$_1$/RNA. White arrows show the resulting particles with lengths in the range of 260 to 270 nm. "no": assembly directed by RNA without any stopper. The black arrows show fully assembled nanotubes with lengths between 300 and 310 nm. Scale bars: 200 nm. Reprinted from Schneider et al. 2016 according to the Creative Commons Non-Commercial Attribution 3.0 International Public License.

4.1.3 Stop-and-go assembly

To determine whether and under which conditions the assembly could be re-activated after stalling the encapsidation, various stop-and-go experiments were performed.

In an initial trial, in the absence of CP, the removal of stopper S3'$_1$ by a ten-fold excess of the release oligomer R3'$_1$ was investigated by an RNase H assay and denaturing gel electrophoresis (see *Appendix* ***Fig. A-1***). Stopper S3'$_1$ was hybridized as mentioned before and the complementary strand R3'$_1$ was added to the sample and incubated for four hours at 25 °C. Complete removal of stopper S3'$_1$ was verified, as undigested full-length RNA was obtained, confirmed by an untreated RNA control sample (Schneider et al. 2016).

To visualize the various assembly intermediates, a step-by-step investigation of the stop-and-go assembly in the presence of CPs (for a scheme see ***Fig. 4-4a***) was performed. The suitable stopper S3'$_1$ was hybridized to RNA using the before-mentioned temperature-gradient protocol and finally mixed with preformed CP disks at 25 °C to initiate the assembly. After three hours a sample was stored at 4 °C, to conserve this assembly intermediate state prior toehold-mediated release of S3'$_1$. To restart the temporarily blocked encapsidation, another part of the sample was mixed with a ten-fold excess of the release oligomer R3'$_1$ over S3'$_1$. Another sample served as negative release control: a ten-fold excess of DNA strand C_2, lacking complementarity to S3'$_1$ was added to the partially assembled tubes. Those aliquots were again incubated at 25 °C for 4 h and subsequently analyzed *via* native gel electrophoresis and TEM in comparison to a sample assembled in the absence of a blocking element (no, ***Fig. 4-4b-c***).The native gel illustrates "stopped" samples (S3'$_1$/– in ***Fig. 4-4b***) with the expected shift of the partially assembled nucleoprotein tubes, whereas the sample after

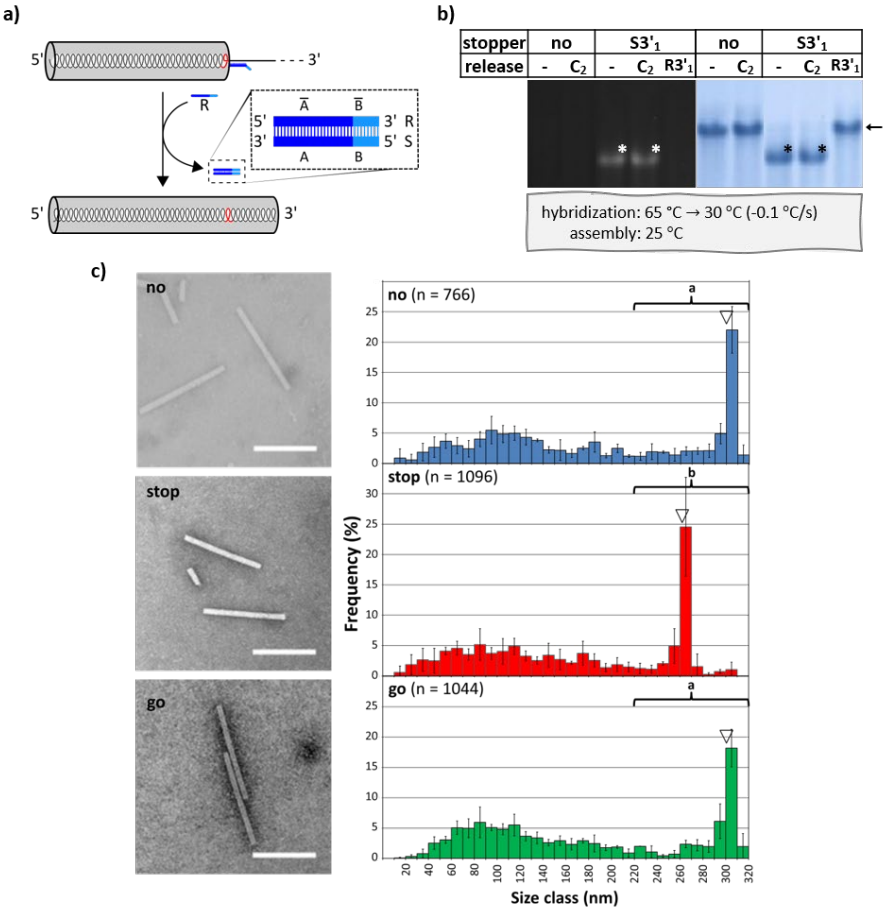

Figure 4-4 "Stop-and-go": controlled stop of the RNA-directed self-assembly of wt-CP by hybridization of stopper S3'$_1$ to RNA, and its subsequent displacement by toehold-release with the DNA "fuel" oligomer R3'$_1$. Reprinted from Schneider et al. 2016 according to the Creative Commons Non-Commercial Attribution 3.0 International Public License. **(a)** Scheme of the "stop-and-go" principle (not to scale). **(b)** Native agarose gel of products in the "stop", "release" and "control" reaction states, *i.e.*, after incubation at 25 °C to allow assembly of nucleoprotein tubes in the absence (no) or presence (S3'$_1$) of the stopper, or after its subsequent release by a suitable oligomer (R3'$_1$) in contrast to an oligomer C_2 non-complementary to S3'$_1$. The arrow indicates the bands of fully assembled tubes as confirmed by comparison with TMV particles. Black/white asterisks (*) label bands of increased electrophoretic mobility, reflecting stalled nanotubes. **(c)** Analysis of the resulting nanotube length distributions. "no": assembly directed by RNA without any stopper; "stop": temporarily stopped assembly directed by S3'$_1$/RNA; "go": assembly directed by S3'$_1$/RNA first, after subsequent addition of R3'$_1$. Left: TEM images; scale bars: 200 nm. Right: Corresponding histograms with *n* structures analyzed. Triangles indicate the expected nanotube lengths. The frequencies of three independent experiments were averaged for every length class, error bars show the standard deviations. The cumulated length data under the brackets were tested for significant differences (Mann-Whitney Rank Sum Test, $p < 0.001$) between the applications. The same lower case alphabetic characters indicate no significant difference.

incubation with the complementary release DNA strand (S3'$_1$/R3'$_1$) showed the same electrophoretic mobility than the samples without addition of any stopper (no/–). Hence, the native gel analysis indicated the successful restart of assembly by a toehold-mediated release of the stopper. Furthermore, TEM imaging confirmed the results of native gel electrophoresis: The electron micrographs (***Fig. 4-4c***) illustrate nucleoprotein complexes exemplarily of each class: stopped (stop) and re-initiated (go) encapsidation as well as assembly in the absence of a stopper (no). As expected from the previous TEM analyses, the uninterrupted growth (no) yielded predominant particle length of 300 nm. The reproducibility of three independent experiments was investigated and their analyses showed no significant difference (see *Appendix* ***Fig. A-2***). Consequently, the total measurements of almost 1000 nanotubes per class were cumulated and depicted in the histograms with the corresponding standard deviation (***Fig. 4-4c***) (Schneider et al. 2016). Blocking the assembly was highly efficient with stopper S3'$_1$, since measurements of the stopped assembly revealed a major fraction of nanotubes with a length of 260 to 270 nm. Restart of the before-stalled nanotubes by toehold-mediated removal of the stopper (go) could be confirmed by a length distribution comparable to continuously grown particles (no). In all assembly reactions a background of TMV-like tubes of heterogenous lengths was observed that usually resulted from stacked CP formations lacking the RNA scaffold or interrupted assembly due to inappropriate RNA secondary structures (Wu et al. 2010; Eber et al. 2015, 2013; Geiger et al. 2013). Nucleoprotein tubes longer than fully assembled TLPs originate from head-to-tail complexes or CP aggregates attached to full-length tubes (Zimmern 1983).

Since the predominant length class of the stopped group corresponded to the RNA portion that was calculated to be accessible between S3'$_1$ and RNA's 5' end (***Table 4-1***), it was assumed that the length of the forming nanotube population for other stopper sites is reliably predictable and with a complementary release strand the blockage is fully reversible under the conditions used. Consequently, TMV-like particles with two precisely defined, differently addressable, longitudinal CP domains (2-DTLPs) may be designed and generated with the stop-and-go technique.

4.1.4 Generation and visualization of 2-DTLPs

To prepare those DTLPs, a purification procedure was required that conserves the blockage of intermediate assembly products as well as the protruding RNA. It was found that assembly remained blocked by $S3'_1$ over a period of 24 h and 12 d, at 25 °C and 4 °C, respectively. Also, the encapsidation could be successfully reinitiated by the addition of the complementary release strand, *i.e.*, the RNA tail remained intact in the majority of particles (data not shown). Ultracentrifugation (UC) was investigated to find out whether it enables the removal of non-assembled CP excess and preserves assembly-competent intermediate products. For this purpose, wt-RNA was hybridized with the highly efficient stopper $S3'_1$ using the established protocol following assembly at 25 °C to form the first 5' domain with wt-CP. The mixture was centrifuged at 90500 *g* for 2 h in the 45 Ti rotor of Optima L90K (Beckman Coulter GmbH) to remove non-assembled wt-CPs and products ≥ 116 S were sedimented. A second CP variant was prepared after coupling of the bifunctional maleimide-PEG_{11}-biotin linker to TMV_{Cys} and subsequent complete removal of residual linker molecules as shown by Koch et al. (2015). The partial TLPs were mixed with this $CP_{Cys\text{-}Bio}$ variant (50 % biotinylation efficiency) and the corresponding release strand $R3'_1$ to initiate the formation of TLP's 3' domain at 25 °C for 16 h. To sediment the final assembly products, the sample was centrifuged *via* UC using similar parameters as above. Several samples (#1-8 in ***Fig. 4-5***) were taken to monitor the qualification of the procedure and analyzed *via* native gel electrophoresis. Successful blocking (#1) as well as restart of assembly (#2) after toehold-mediated release of $S3'_1$ was found with the usual efficiency. The supernatant of first UC (#3) contained non-assembled CP but also partially assembled tubes, *i.e.*, the desired product was not completely sedimented with parameters applied during UC. However, the resolved pellet clearly indicated stalled tubes prior (#4) and after addition of $R3'_1$ (#5), consequently, the first CP variant was fully removed by UC. When $CP_{Cys\text{-}Bio}$ was added in combination with the release strand (#6-8), fully-encapsidated particles were visualized by electrophoretic shift to the range of full-length nanotubes and lacking the EtBr signal. Fractions of less electrophoretic mobility found in samples #4-6 and #8 seemed to be formed after UC depending on concentration of nucleoprotein complexes. A CP cloud was shown in the supernatant (#7), but not in the resolved pellet (#8) indicating complete removal of the residual free $CP_{Cys\text{-}Bio}$. Around 50 % of the second CP variant was coupled with the maleimide-PEG_{11}-biotin linker (data not shown) resulting in diverse compositions of the formed 3' segment. As the negative net charge of CP_{Cys}, $CP_{Cys\text{-}Bio}$ and wt-CP differ, DTLPs of the same length but with various arrangements of the second domain (#6-8) yielded a broader fraction in native gels in contrast to completed nanotubes with

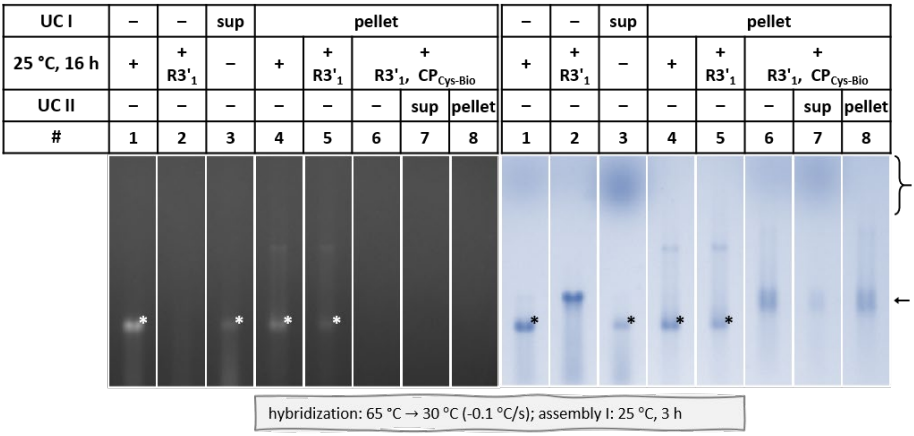

Figure 4-5 Monitoring the 2-DTLP preparation and purification procedure. Hybridization of S3'$_1$ to RNA followed by assembly of the first 5' domain with wt-CP were performed as depicted below the image. The following steps and the sample numbers (#) are depicted in the table (detailed description see text); sup = supernatant. Different samples of preparation were analyzed by nanoparticle separation in a native agarose gel. Black/white asterisks (*) label bands of increased electrophoretic mobility, reflecting stalled nanotubes. The arrow indicates the bands of fully assembled tubes and the upper bracket marks the residual free CPs.

wt-CP (#2). To analyze the lengths of the distinct domains *via* TEM, the tetrameric glycoprotein avidin was coupled to the exposed biotin of the as-produced wt-Cys$_{Bio}$-DTLPs. The subsequent TEM imaging showed only a faint coverage with avidin of the desired domain. Hence, the analysis of images resulted in unreliable length measurements between various nanotubes so that a clear delimitation of the distinct domains was not possible. This could be attributed to the low biotinylation efficiency (50 %) of the applied CP$_{Cys-Bio}$ preparation as it was expected from the used protocol (Koch et al. 2015) in combination with coupling of the small biomolecule avidin (≈ 66 kDa, 5.6 x 5.0 x 4.0 nm (Pugliese et al. 1993)). Although, the decoration of the CP$_{Cys-Bio}$ domain with a streptavidin-conjugated glucose oxidase (Koch et al. 2015) yielded better visualization by TEM due to the larger molecules, a concrete determination of length was inconclusive since no sharp borders were obtained (data not shown).

However, to reliably estimate the length of a domain, a higher number of biotin molecules accessible for small molecules, like avidin, appeared crucial. To constitute uniformly decorated segments that only expose the similar functional group, another CP variant was explored to enhance the density of biotin moieties.

For this purpose, TMV_{Lys} (Geiger et al. 2013) was covalently conjugated with a bifunctional NHS-PEG_{12}-biotin linker to the additional lysine residue on the outer surface of every CP in two parallel samples. In both cases, almost 100 % functionalized $CP_{Lys\text{-}Bio}$ were obtained (data not shown). 2-DTLPs containing the as-produced $CP_{Lys\text{-}Bio}$ were fabricated by hybridization of stopper $S3'_1$ to wt-RNA, followed by assembly with wt-CP, to generate the first 5'-terminal domain with a desired length of 261 nm. The ultracentrifugation procedure was further optimized by an increase of the rotational centrifugal force (113 000 *g*, 2 h) to fully sediment the desired nanotubes blocked at the $S3'_1$ site. Accordingly, free wt-CP and smaller TLP aggregates could be removed, and the partially assembled nanotubes and the residual RNA tail remained intact. The almost pure sample was mixed with the second $CP_{Lys\text{-}Bio}$ variant as well as with $R3'_1$. After toehold-mediated release of stopper and completion of the nanotubes, the desired assembly products were enriched by UC. The purified wt-Lys_{Bio}-DTLPs (261-39) were subjected to bio affinity coupling of avidin followed by a final sedimentation *via* UC and subsequent analysis by electron microscopy. TEM images showed indeed nanoobjects with two domains of different size. A longer, smooth domain formed with wt-CP as well as the avidin-decorated $CP_{Lys\text{-}Bio}$ part visualized by a uniform surrounding corona were found (***Fig. 4-6***).

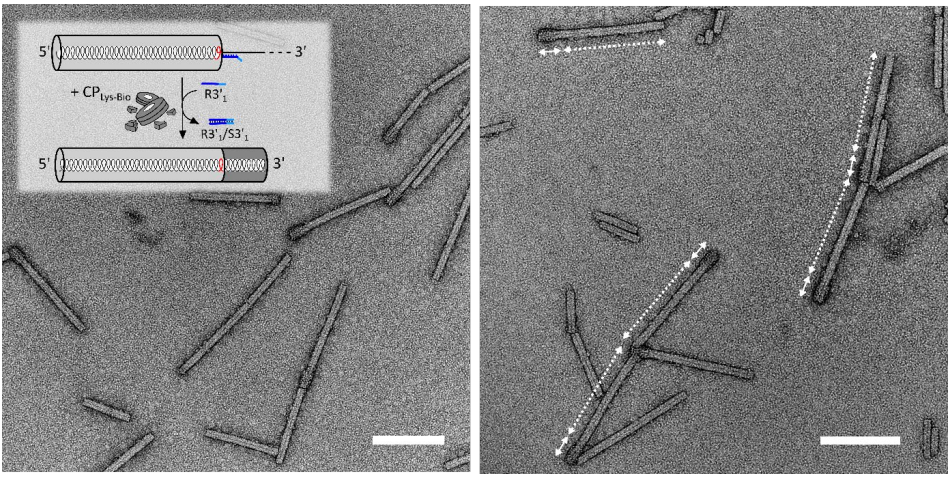

Figure 4-6 Electron micrographs of TMV-like nanotubes with two subdomains of distinct CP variants. These domain-TLPs were prepared through the stepwise, externally controlled stop-and-go procedure as it is schematically depicted in the inset (not to scale; adapted from Schneider et al. 2016 according to the Creative Commons Non-Commercial Attribution 3.0 International Public License). The dotted arrow denotes the smooth first assembled wt-CP domain, the small continuous arrow the adjacent avidin decorated $CP_{Lys\text{-}Bio}$ domain. Scale bars: 200 nm.

Determination of the individual segments based on 70 nanotubes of a total length ranging from 285 nm to 320 nm bearing two discriminable domains. The longer 5' part had an average length of 260 nm, whereas the avidin-decorated segment resulted in 45 nm. The increase of the 3'-terminal domain by 5 nm attributed to the length of the biotin-linker-attached avidin (Pugliese et al. 1993). Those results confirm the successful fabrication of the desired TMV-like particles with two different precisely separated CP regions (Schneider et al. 2016).

4.2 Universality of dynamic DNA-controlled assembly

To explore whether the stop-and-go technique is limited to binding sites of stoppers in the original TMV-RNA or if it can be expanded to arbitrary sequences, three distinct plasmid constructs were prepared for the generation of heterologous RNAs (hRNAs). Subsequently, the universality of the dynamic DNA-controlled assembly of TLPs could indeed be shown with the variable hRNA scaffolds and corresponding stoppers (Schneider et al. 2016).

4.2.1 Production and evaluation of assembly-competent scaffolds with heterologous sequences

The individual DNA constructs were designed and generated by discrete cloning procedures, each containing the cDNA sequence of TMV-OAs with variable surrounding context and different non-TMV sources (schematically shown in ***Fig. 3-1***). Construct I, based on the vector pGEM®-T Easy as well as the smallest inserted TMV-OAs portion (nt 5350-5531), was linearized with DraIII and, subsequently, hRNA I was produced by *in vitro* transcription using T7 RNA polymerase. During investigations on construct I and the corresponding hRNA I, a T7 RNA polymerase transcription terminator sequence was identified at position 1262-1301 (Jeng et al. 1992). This resulted in a mixture of two RNA fractions: a terminated product with a length of 1262 nt and the read-through hRNA I with 2748 nt (see *Appendix* ***Fig. A-3a***). The second plasmid consists of a eukaryotic background construct (full-length of AbMV DNA A, for details see **Chapter 3**) inserted into pLITMUS 28i and a short TMV sequence including its OAs (nt 5211-5584). Transcription of the SacI-HF-linearized construct II yielded pure hRNA II with a length of 2982 nt. The longest TMV sequence (nt 4253-6398) was inserted into pBlueScript II SK (+) and served as the third vector construct. The template was linearized with ScaI-HF and transcribed by T3 RNA polymerase. The resulting hRNA III was 3303 nt in length and produced with high purity and yield. All hRNA scaffolds were confirmed by denaturing gel electrophoresis (see *Appendix* ***Fig. A-3a***).

The various hRNAs served as examples for the possibility to encapsidate scaffolds with different coding and non-coding RNA sequences of prokaryotic and bacteriophage sources (in hRNA I/III), RNA portions with eukaryotic ORF origin in coding and reverse orientation (elements of AbMV DNA in hRNA II) as well as non-coding intergenic regions (in all hRNAs). To investigate the assembly-competence, hRNAs were incubated with TMV-CP at 25 °C and the assembly products were compared in respect of their nanotube sizes after separation by native gel electrophoresis (***Fig. A-3b***). hRNA I showed two fractions of various electrophoretic mobility, corresponding to

fully encapsidated nanotubes of different lengths, since no EtBr signal was found. That means that both, the read-through (2748 nt) as well as the terminated hRNA I (1262 nt), were assembled into nucleoprotein complexes with high efficiency. hRNA II resulted in diverse assembly products, some of them with residual free RNA tails as visualized by EtBr. hRNA III yielded a major fraction of fully encapsidated tubes as well as one faint signal of partially assembled tubes. Furthermore, to compare the usual assembly reaction (iva) with the conditions during the stop-and-go process, another sample was prepared with a denaturation step at 65 °C prior assembly, corresponding to the hybridization procedure lacking a stopper (no). Native gel electrophoretic analysis of assembled hRNA I and II illustrated only minor differences of both procedures (iva and no in ***Fig. A-3c***). In contrast to nucleoprotein complexes formed by hRNA I and II, the assembly products of hRNA III with (no in ***Fig. A-3c***) and without prior denaturation (iva) differed: A third product with the highest electrophoretic mobility was produced, additionally to the before-mentioned fully and partially encapsidated tubes during imitating the hybridization procedure (no).

The following TEM analysis of assembly products without addition of a stopper (no) were performed to better understand the individual fractions. The broader size distribution of nanotube lengths (***Fig. 4-7***) scaffolded by all hRNAs compared to assembly of wt-RNA was confirmed. However, TEM imaging revealed the formation of nucleoprotein rods with a diameter of 18 nm comparable to native TMV.

TLPs scaffolded by hRNA I resulted in a major length class ranging from 60-65 nm, corresponding to fully encapsidated terminated hRNA I, whereas no prominent class in the size of completely assembled read-through product (129 nm) was found. Furthermore, the background of smaller aggregates was higher than it is known from assembly products of wt-RNA. Analysis of assembly products of hRNA II also revealed around 50 % small nanotubes ranging between 35-75 nm. The findings of TEM and native gel were in agreement and indicated that those smaller objects were aborted assembly products with protruding RNA, that however was not visible by negative staining in TEM. The size class correlating with predicted full-length particles (140 nm) scaffolded by hRNA II yielded a frequency of 7 %. Analysis of TMV-like tubes, templated by hRNA III, resulted in the prominent size classes 150-155 nm and 155-160 nm, respectively, representing fully encapsidated nucleoprotein tubes with an expected length of 155 nm. This was conformed with the predominant fragment observed in native gels. Furthermore, classes ranging between 90-120 nm showed a frequency of around 25 % that could lead to the background seen in gel analysis, however, an additional concrete fraction was not found.

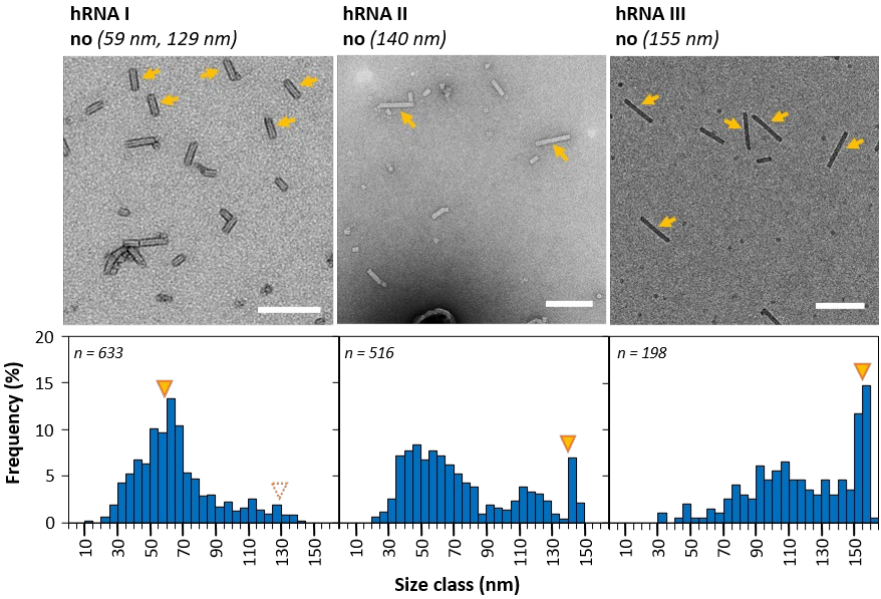

Figure 4-7 Investigation on the self-assembly with wt-CPs of the distinct hRNAs lacking a stopper (no). **TEM analysis:** Expected particle lengths (nm) are illustrated above each TEM image. Orange asterisks illustrate TLPs of the desired length in the respective class. Scale bars: 200 nm. **Length distribution:** histograms with *n* structures analyzed. The orange triangles indicate the expected nanotube lengths, the dotted orange triangle depicts the assembly product of the read-through hRNA I. Adapted from Schneider et al. 2016 according to the Creative Commons Non-Commercial Attribution 3.0 International Public License.

Although the distribution of nucleoprotein tube length was higher than for encapsidation of wt-RNA, the assembly-competence of all hRNAs was confirmed.

4.2.2 Analysis of blocking the encapsidation at different heterologous RNA sites and its reinitiation

As the assembly-competence of the different hRNA templates with wt-CP was shown, it was now explored whether the encapsidation of hRNAs could be interrupted with corresponding stoppers complementary to distinct heterologous sequences. For this purpose, four to five stoppers were designed to target in distinct non-TMV sequences downstream of the OAs (see ***Fig. 4-8a*** for binding sites and ***Tab. 3-2*** for characteristics). Individual experiments were performed using the same conditions as established for wt-RNA with and without the various stoppers hybridized to hRNA I, II and III, respectively, and analyzed *via* gel electrophoresis (***Fig. 4-8b-d***). All stoppers binding to hRNA I interfered with the assembly resulting in additional bands of higher electrophoretic mobility with intense EtBr signal unlike full-length TLPs (***Fig. 4-8b***). hI-S3'$_3$ showed the highest blocking

effect with a low fraction of fully encapsidated tubes. Another trend was found for hRNA II: hII-S3'$_5$ strongly blocked the encapsidation, stoppers hII-S3'$_1$ and hII-S3'$_4$ stalled the assembly to a minor extent, respectively, whereas hII-S3'$_{2\text{-}3}$ had no impact or could not be differentiated from background fractions, that were obtained for all samples (***Fig. 4-8c***).

All combinations of stopper/hRNA III showed fully assembled nanotubes as well as the additional partially assembled TLPs (***Fig. 4-8d,*** depicted by the curly brackets) that were seen in the experiments without any stopper (no). Precise stalling of the assembly by a DNA strand was only successful using h-S3'$_1$. Here, a distinct isolated fragment was detected by protein as well as RNA detecting agents that evidently differed from the sample lacking a stopper.

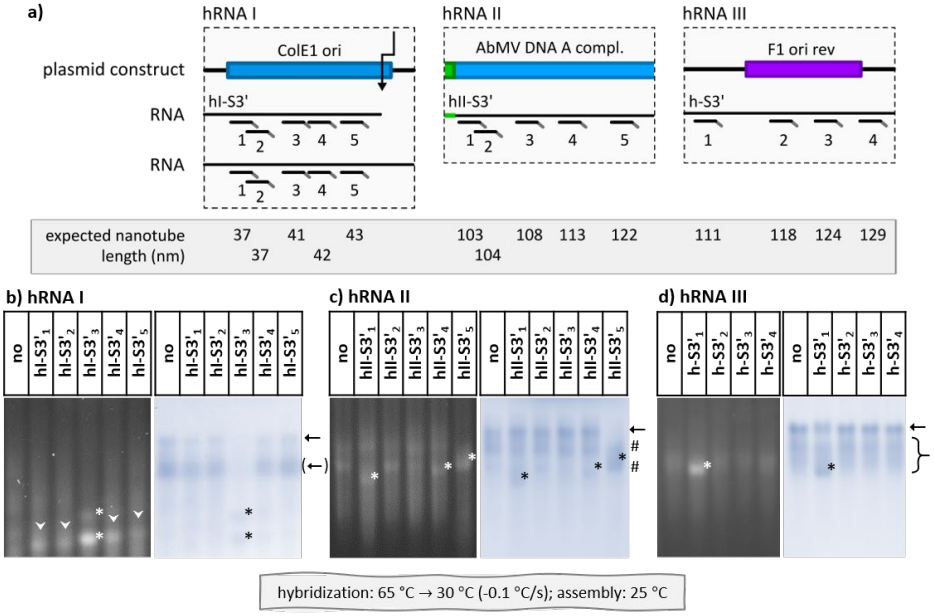

Figure 4-8 Impact of various stoppers on the assembly of hRNAs with TMV-CP. **(a)** Scheme illustrates binding sites of stoppers on the RNA in respect of regions in the plasmid construct and are in accordance with ***Fig. 3-1***. Drawings are not to scale. **(b-d)** Electrophoretic separation of the assembly products scaffolded by heterologous RNA I to III in 1.5 % native agarose gels. Control samples (no) were prepared under the same conditions, *i.e.*, fully assembled nanotubes scaffolded by hRNAs devoid of stoppers. The arrow indicates bands of fully assembled tubes as confirmed by the control sample. Black/white asterisks (*) label concrete bands with higher electrophoretic mobility. White triangles indicate EtBr signals corresponding to these bands, and residual free RNA, however, their Coomassie Brilliant Blue signal is too low to visualize concrete fractions. The arrow in the brackets shows the terminated product of hRNA I (b). The hash marks (c) and the bracket (d) denote the range of (background) fragments additionally obtained in all samples using the conditions depicted below the image.

Since the denaturing gel electrophoresis clearly indicated only one RNA species in the sample, the additional fragments arose during assembly.

As a brief reminder, native gel electrophoresis visualizes a linear correlation of blocked nanotubes with intact residual RNA when the total RNA length as well as the blocking side in respect of the OAs are similar. Thus, various 3' stoppers that were known to reliably block the assembly at binding sites within the TMV sequence were hybridized to hRNA III, followed by assembly with wt-CP, to generate a ladder for determining the nucleoprotein tube size as well as the protruding RNA length (***Fig. A-4***). Analyses of three independent sets of samples without a stopper separated in native gels revealed that the additional fragments with higher electrophoretic mobility correlate with a partially assembled nucleoprotein rod of ≈ 138 nm and ≈ 122 nm with the residual RNA length of ≈ 360 nt and ≈ 690 nt, respectively. The incompletely encapsidated product of ≈ 122 nm, that resulted after performing the hybridization procedure at 65 °C, might be aborted in the region that originates from the F1 origin sequence.

To investigate whether the most competent stoppers have additional binding sites of lower specificity, stoppers hI-S3'$_3$, hII-S3'$_5$ and h-S3'$_1$ were hybridized to hRNA I, II and II, respectively, using the standard procedure (65 °C, 5 min → 30 °C (-0.1 °C/s)) followed by RNase H cleavage. Analysis *via* denaturing gel electrophoresis confirmed that the stopper bound efficiently to the RNA and no unspecific stopper binding resulted under conditions used (data not shown), supporting the findings that specific RNA sequence interrupted the assembly with CP. Furthermore, initial investigations to completely remove the individual hybridized stopper by a ten-fold excess of the corresponding release oligomers were performed in the absence of CP at 25 °C for 4 h. Subsequently, those samples were also incubated with RNase H, separated on denaturing gels, and verified the complete removal of stopper for each scaffold (data not shown).

To explore full stop-and-go experiments, the most competent stoppers, hI-S3'$_3$, hII-S3'$_5$ and h-S3'$_1$ were hybridized to the respective hRNAs, followed by assembly with wt-CP. The corresponding release DNA strands to restart the assembly, were mixed with the sample without exchanging the CP variant.

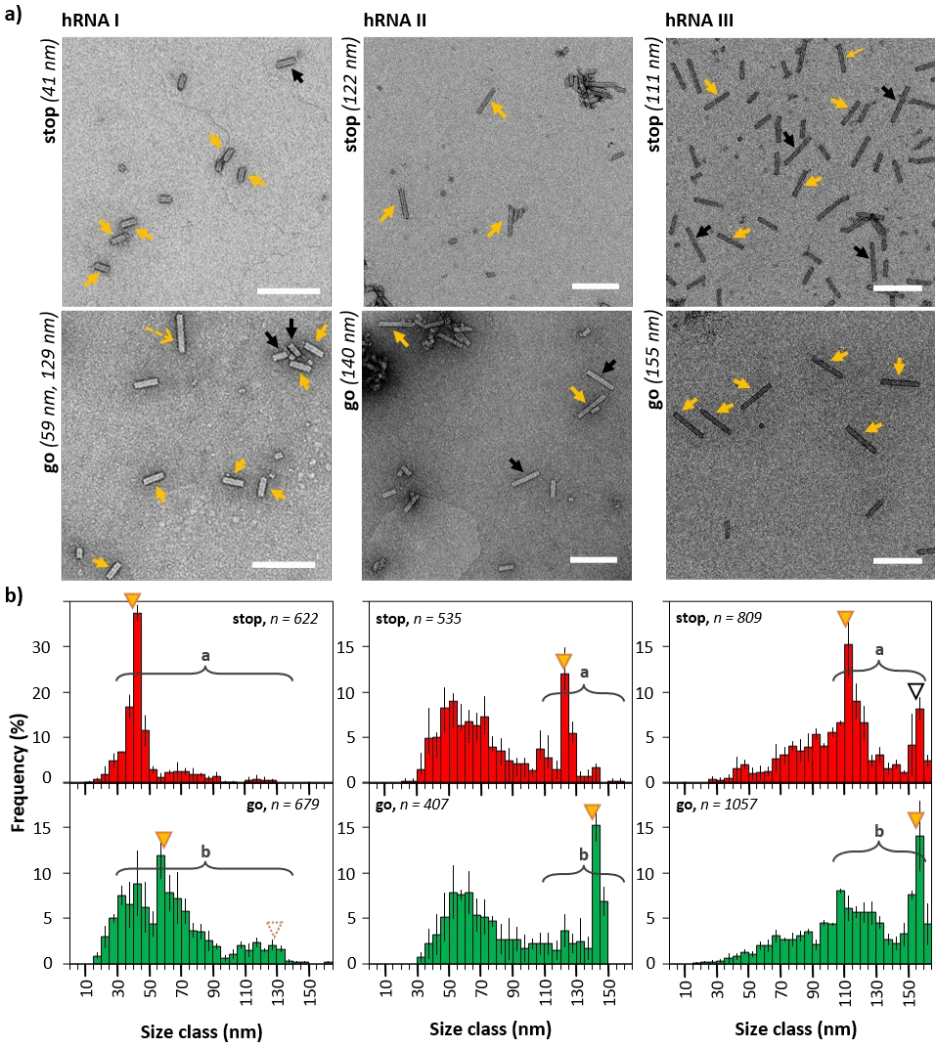

Figure 4-9 Investigation on the controlled RNA-directed self-assembly of wt-CPs by annealing the functional stoppers to the distinct hRNAs (stop), and its subsequent displacement by toehold-release with the release DNA oligomer (go). **(a)** TEM analysis: Expected particle lengths (nm) for the various classes are illustrated at the left side of each TEM image. Orange asterisks illustrate TLPs of the desired length in the respective class. Black asterisks depict the non-blocked as well as the remaining stalled nanotubes within the "stop" and "go" samples. The dotted arrow shows a full-length TLP of the read-through hRNA I (go). Scale bars: 200 nm. **(b)** Statistic comparisons (as described for ***Fig. 4-4***): The orange triangles indicate the expected nanotube lengths, the dotted orange and the black triangle depicts the assembly product of the read-through hRNA I and the non-stalled fraction of hRNA III, respectively. Adapted from Schneider et al. 2016 according to the Creative Commons Non-Commercial Attribution 3.0 International Public License.

The stop-and-go competence was analyzed by qualitative and quantitative TEM imaging. Electron micrographs represent nucleoprotein complexes exemplarily of the different groups of stopped (stop) and re-initiated (go) encapsidation (***Fig. 4-9a***). Three replicated independent experiments were analyzed. Since the individual experiments of each group were not significantly different (see *Appendix* ***Fig. A-5***), the findings were accumulated and illustrated in the histograms with the corresponding standard deviation (***Fig. 4-9b***). Equivalent results were observed for hRNA I and II: Stoppers strongly blocked the assembly and resulted in nanotubes (stop) of the desired length classes, 40-45 nm and 120-125 nm, for hI-S3'$_3$/hRNA I and hII-S3'$_5$/hRNA II, respectively, as implied by electrophoretic analysis. The background of small assembly products of hII-S3'$_5$/hRNA II was similar to the sample lacking the stopper (no), whereas hI-S3'$_3$/hRNA I showed only minor fractions of lengths > 50 nm indicating that the stopper efficiently stalled the assembly for both, the terminated as well as the read-through hRNA I. The assembly-reinitiation of before-blocked nanotubes by the toehold-mediated release of stopper *via* the complementary release strand (go) was confirmed by the shift of major fractions to the sizes of expected full-length particles and a length distribution comparable to continuously grown particles (no). As it was expected from native gels as well as from the sample lacking the stopper (no), only a minor fraction of fully encapsidated read-through hRNA I was found, exemplarily visualized in the TEM image (go) by the dotted yellow arrow. The assembly of hRNA III in the presence of h-S3'$_1$ (stop) yielded a maximal frequency of 15 % for size class 110-115 nm correlating with the predicted length of arrested tubes (111 nm). Blocking the encapsidation of hRNA III by h-S3'$_1$ was not highly efficient as another prominent class was obtained in the range of completely assembled tubes consistent to the findings of native gel analysis. However, the complete restart of assembly was verified for a major fraction of nanotubes in the size class of full-length particles (155-160 nm) after DNA-mediated release of the stopper (go). A significant difference of "stop" and "go" groups, was found for all RNA scaffolds (***Fig. 4-9b***).

The results based on three heterologous RNA sequences, containing the TMV-OAs to various extent, have verified the universality of the stop-and-go technique (Schneider et al. 2016) and gave an insight into the blocking competence of stoppers in regions of non-TMV origin and the challenges of secondary structures of such RNA sequences during assembly with CP.

4.3 Challenges of stopping the nucleoprotein tube assembly

The previous chapters present results with 3' stoppers that block the assembly of wt-RNA as well as of hRNAs with wt-CP. Furthermore, the arrested nanotubes could be completed by another CP variant after the toehold-mediated release of stoppers. 3' stopping of wt-RNA resulted in different amounts of partially assembled particles, depending on the stopper's 3' position at the RNA, that means that the yield of subsequent generation of desired TMV-like particles with multiple domains is affected. The following studies will reveal deeper insights into blocking capabilities of various stoppers complementary to 3' sites in respect of the OAs during DNA-controlled assembly of RNA with CP and additionally investigate the use of 5' positions, *i.e.*, upstream the OAs (for schematic details see ***Fig. 4-10***).

4.3.1 Influence of RNA structure on stopper competence

As some results indicated that the spatial RNA structure hinders hybridization of a stopper, the correlation of binding competence, and thus the stop-ability of a stopper and the distinct RNA sequence were evaluated. For this purpose, various sets of 3' stoppers each complementary to the same RNA region were selected. Stoppers were designed using similar characteristics than for the suitable stopper S3'$_1$, with three sets of partially overlapping stopper sequences within the same regions of interest. The overlap lengths varied, as detailed in ***Table 3-2***.

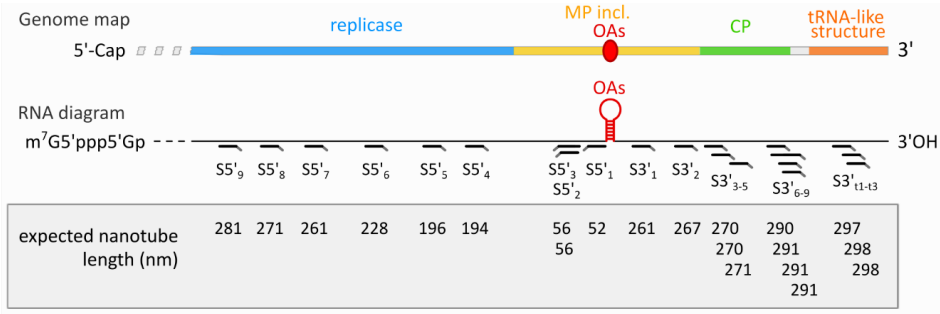

Figure 4-10 Schematic details of stopper binding sites on the wt-RNA in respect of regions in the genome (not to scale). The genome map illustrates the regions, coding for the different proteins as well as areas forming the OAs or the tRNA-like structure, respectively, in respect of the stopper binding regions illustrated in the RNA diagram. In the diagram the binding sites of the different stoppers on RNA in relation to the origin of assembly (OAs) position (symbolized as a hairpin, red) are depicted. The expected nanotube length (grey box) is calculated using wt-RNA as scaffold for the self-assembly with CP in the presence of the respective stopper.

The following three sets of stoppers were investigated: S3'$_{3\text{-}5}$ and S3'$_{6\text{-}9}$ are complementary to two different RNA regions within the CP coding sequence (Guilley et al. 1979), nt 5733-5784 and nt 6159-6205, respectively, and S3'$_{t1\text{-}3}$ target position 6323-6359, that forms the tRNA-like structure (TLS) (Guilley et al. 1975) (binding sites depicted in ***Fig. 4-10***, for sequences and characteristics see ***Table 3-2***).

Newly designed 3' stoppers were evaluated using the above-mentioned standard protocol. Briefly, stoppers were hybridized to RNA by an initial denaturation at 65 °C for 5 min, followed by cooling down to 30 °C with a rate of 0.1 °C. The nucleoprotein tube assembly was initiated by the addition of wt-CP to the stopper/RNA mixture, followed by an incubation at 25 °C for 5 h. The assembly products were analyzed *via* native gel electrophoresis. Stoppers S3'$_{3\text{-}5}$ arrested the nanotube growth, visualized by higher electrophoretic mobility and an explicit EtBr signal associated with the free RNA tail than full-length TLPs (***Fig. 4-11***).

However, stoppers S3'$_{3\text{-}5}$ varied in their blocking efficiencies. Approximately 85 %, 50 % and 95 % partially encapsidated tubes resulted from blocking the assembly with S3'$_3$, S3'$_4$ and S3'$_5$, respectively. Stoppers complementary to the tRNA-like region also differed in their stop-competence. S3'$_{t1}$ blocked the assembly to a minor degree that was too small to distinguish from full-length particles, whereas S3'$_{t2}$ and S3'$_{t3}$ yielded ≈ 100 % stalled TLPs. Calculations of the yields at 25- and 40-fold molar excess *via* the software ImageJ obtained no relevant differences.

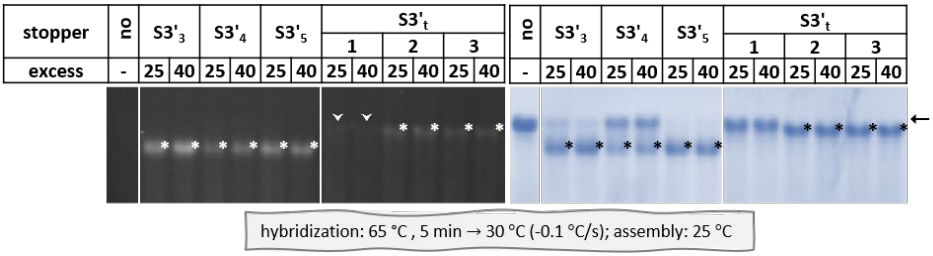

Figure 4-11 "3' Stop": the influence of distinct 3' stoppers on the self-assembly of wt-CP with RNA using standard conditions: Hybridization was performed with two variant molar excesses of stopper over RNA for 5 min at 65 °C, cooling to 30 °C with a rate of 0.1 °C/s, followed by assembly for 5 h at 25 °C (depicted below the image). Visualization of "stop" state after nanoparticle separation in a native agarose gel. A control sample was prepared under the same conditions: "no", *i.e.*, fully assembled nanotubes scaffolded by RNA devoid of stoppers. The arrows indicate bands of fully assembled tubes as confirmed by the control sample. Black/white asterisks (*) label bands with higher electrophoretic mobility. White triangles indicate EtBr signals corresponding to these bands, and residual free RNA, however, the yield is too low to differ from full-length tubes.

Major differences in the blocking competence for the third set of stoppers (S3'$_{6, 8, 9}$) were found (see *Appendix* ***Fig. A-6a*** for results): S3'$_6$ did not block the assembly, whereas S3'$_8$ as well as S3'$_9$ resulted in 60 % and 100 % stopped nanotubes, respectively. To investigate whether an increased number of complementary nucleotides could enhance the strand displacement effect to unfold the secondary structure of RNA, S3'$_7$ was designed with an enhanced binding region (37 nt) that partially overlap with the non-efficient S3'$_6$ and completely with the suitable stoppers S3'$_8$ and S3'$_9$. However, native gel analysis showed that only 60 % of encapsidated nanotubes were blocked by S3'$_7$ (***Fig. A-6a***). Even hybridization after a partially denaturation treatment at elevated temperature adjusted for the higher T_m, followed by a temperature ramp with a second plateau (75 °C, 3 min → 70 °C, 3 min → 30 °C (-0.1 °C/s)) did not enhance the blocking efficiency above 60 % (data not shown).

In comparison of the blocking efficiencies of these three sets of stoppers with the low differences of characteristics between the individual stoppers, no trend of T_m, %GC and binding length in respect of stop-ability was revealed. However, the results implied that the specific binding position has the highest impact due to the individual spatial RNA structure. The site-specific effects on the accessibility of RNA will be investigated in ***section 4.3.4***.

Nevertheless, as a whole, ten out of twelve 3' stoppers were found to stall the assembly with different efficiencies using the established standard conditions.

4.3.2 Effect of the deviant 5' CP assembly mechanism on blocking nanotube growth upstream the TMV-OAs

The previous parts focused on the RNA region downstream (3') the OAs, that amounts to 40 nm of the fully assembled nucleoprotein tube. In contrast, the next section investigates whether and how the upstream portion might be manipulated during its self-assembly. Since 3' and 5' direction relative to the OAs differ in their assembly rate and elongation mechanism (Butler and Lomonossoff 1980; Butler 1999) (see ***section 2.2.1*** for further details), the influence of the bidirectional, asymmetric assembly of TMV-RNA will be discussed.

In a first approach, two stoppers (S5'$_1$ and S5'$_2$) addressing sites 5' of the OAs were investigated in respect of their hybridization efficiency. Both stoppers possess a TMV-RNA-complementary part of 22 nt and a 3' toehold. The binding sites are adjacent to the OAs region with sequences resulting in distinct characteristics of both stoppers, although, their binding length is similar (for binding sites see ***Fig. 4-10***, for sequences and characteristics see ***Table 3-2***). Hybridization of stoppers to RNA was performed using the standard procedure (65 °C, 5 min → 30 °C (-0.1 °C/s)) and followed by

incubation with RNase H. After RNA cleavage with RNase H at the RNA/DNA duplex position, two defined fractions were found in the denaturing agarose gel for both stoppers, indicating efficient hybridization of the DNA strands to RNA (***Fig. 4-12a***) (Schneider et al. 2016). To test whether the stoppers also blocked the self-assembly of wt-CP with RNA, the established procedure was executed. However, the assembly of the hybridization mixture with wt-CP at 25 °C yielded only about 25 % or 5 % of partially assembled TLPs, blocked by S5'$_2$ or S5'$_1$, respectively (***Fig. 4-12b***) (Schneider et al. 2016). As the assembly rate into 5' direction is approximately 4-times higher than that of the 3' assembly and uses preformed CP disks in a cooperative manner (Butler 1999; Eber et al. 2015), it was assumed that the stoppers were sheared off the RNA during the assembly.

To examine whether the blocking capability at sites 5' of the OAs was only dependent on the assembly direction and thus mechanism, various stoppers complementary to different RNA sites 5' of the OAs were configured (see S5'$_{3\text{-}9}$ in ***Fig. 4-10*** and ***Table 3-2***). S5'$_3$ features an extended binding length (by 9 nt of the sequence of S5'$_2$), to rule out if a higher binding strength hinders shearing of the stopper at similar position. In contrast, stoppers S5'$_{4\text{-}9}$ were designed with 5' toeholds (relative to their sequence) and with similar characteristics (T_M, %GC-content, binding length) as the suitable 3' stoppers. To explore this RNA region, the self-assembly in the presence of the newly designed 5' stoppers was first investigated using the established conditions. Native gel electrophoretic separation showed that stoppers S5'$_{4\text{-}9}$ did not stall the assembly process as efficiently as it was expected after the RNase H assay, whereas blocking with S5'$_3$ resulted in 25 % partially assembled tubes comparable to the blocking efficiency of S5'$_2$ (data not shown). As the findings of low blocking effect were similar to the previous observation in studies with stoppers S5'$_1$ and S5'$_2$ (Schneider et al. 2016), the experiments suggested consistently that the major impact on the ineffective 5' stopping resulted from the higher assembly rate into 5' direction that displaced the hybridized stoppers. To generate multiple domains despite a background of unwanted full-length tubes due to inefficient stopping, a higher yield of 5' stalled nucleoprotein tubes was required. Hence, further developments on the stop-and-go conditions were performed, to manipulate the assembly in the upstream direction of the OAs. As the assembly rate of TMV depends to a certain extent on the temperature, the stop-and-go procedure might be improved for 5' regions by decreasing the assembly temperature. For this purpose, the stoppers were hybridized to the RNA under standard hybridization conditions (65 °C, 5 min → 30 °C (-0.1 °C/s)). However, for both stopper variants, S5'$_2$ and S5'$_3$, the CP disk preparations were assembled with the RNA at temperatures of 25°C and 15°C, respectively, to compare the conditions (25 °C) used in 3' direction with a lower temperature.

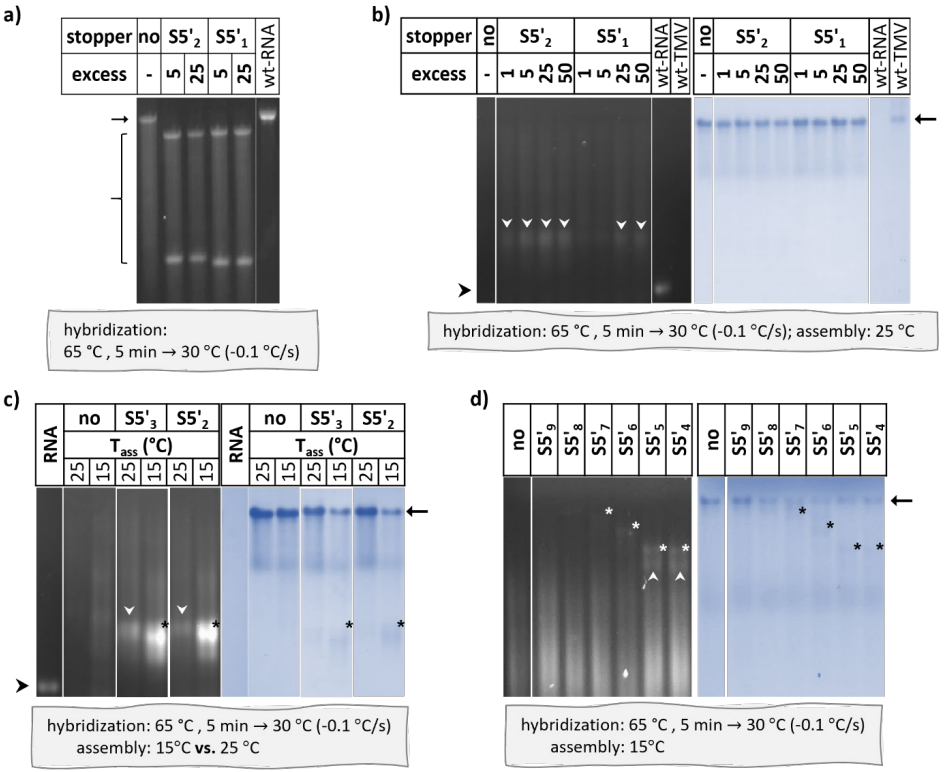

Figure 4-12 Stopping at sites 5' of the OAs. **(a)** Agarose gel electrophoretic separation (1 % agarose, under denaturing conditions) of the products after RNase H cleavage of DNA/RNA hybridization products of wt-RNA. Stoppers were hybridized to the RNA in 5- and 25-fold molar excess, prior to RNase H treatment. The arrows denote the bands of undigested RNA and brackets the range of fragments expected after digestion. **(b-d)** Visualization of "stop" state after nanoparticle separation in a native agarose gel. A control sample was prepared under the same conditions: "no", *i.e.*, fully assembled nanotubes scaffolded by RNA devoid of stoppers. TMV and/or wt-RNA serve as markers. The arrows indicate bands of fully assembled tubes as confirmed by the control sample. Black/white asterisks (*) label bands with higher electrophoretic mobility. White triangles indicate EtBr signals corresponding to these bands, and residual free RNA, however, their Coomassie Brilliant Blue signal is below the visualization limit. The arrow head (left side, c) depicts full-length form of RNA. Hybridization was performed followed by assembly as depicted below the image: variable molar excess of stoppers S5'$_1$ and S5'$_2$ over RNA using the standard procedure **(b),** stalling by S5'$_2$ and an elongated S5'$_3$ each in comparison of two different assembly temperatures (T_{ass}) **(c),** and investigation of further 5' stoppers at T_{ass} = 15 °C **(d)**. (a+b) are adapted from Schneider et al. 2016 according to the Creative Commons Non-Commercial Attribution 3.0 International Public License.

The blocking efficiencies at both temperatures were compared by nanotube separation *via* native gel electrophoresis (***Fig. 4-12c***). A brighter EtBr as well as Coomassie Brillant Blue signal depicted that stopping the assembly by S5'$_2$ as well as by S5'$_3$ at 15 °C was more efficient than at 25 °C and resulted in 65 % and 58 % of partially assembled TLPs, respectively. However, analysis of assembly at the lower temperature revealed that the total assembly yield was reduced by one-third in contrast to encapsidation at 25 °C. Since comparable blocking efficiencies were found for the assembly-stop with both, S5'$_2$ and S5'$_3$, respectively, at 25 ° and 15 °C, the extended binding part of S5'$_3$ did not increase the blocking effect.

Stopping at 5' sites of the OAs with stoppers S5'$_{4\text{-}9}$, showed the same trend using different assembly temperatures: The yield of stalled TLPs was higher after assembly at 15 °C compared to assembly at 25 °C, but the overall yield of nanotubes was reduced with the decreased assembly rate (***Fig. 4-12d***). Furthermore, so far, it was not conclusive, whether the 5' toehold of S5'$_{4\text{-}9}$ has an impact on the blocking efficiency due to an enhanced sterical hindrance for binding the next CP disk, as it was the first part that was pulled towards the inner disk channel in contrast to the 3' toehold of S5'$_{1\text{-}3}$.

4.3.3 Impact of the hybridization procedure on the assembly competence

To produce DTLPs in a multiple step procedure, the overall yield of correct intermediates and final nanotubes required an improvement, as introduced in the above section. Previous results had shown decreased total yields of nanotube assembly for hybridization protocols with an initial heating step to 50 °C or 65 °C, respectively (**Chapter 4.1**), in comparison to simple TLP assembly at 25 °C, that may have resulted from RNA refolding into assembly-incompetent secondary structures following its partial denaturation. To compare the influence of denaturation/hybridization temperatures, procedures under milder conditions were studied. The assembly of nucleoprotein tubes was performed, after employing milder conditions (25 °C or 30 ° for 2 h) for RNA pre-treatment and binding of S3'$_1$. Parallel samples were treated according to the standard procedure (65 °C, 5 min → 30 °C (-0.1 °C/s)) and the assembly products were analyzed by native gel electrophoresis. The background of different RNA folding states found after binding of S3'$_1$ to RNA in a partial denaturation step at 65 °C visualized by EtBr (curly bracket in ***Fig. 4-13a***) were not seen using the milder hybridization conditions (25 °C or 30 ° for 2 h). Furthermore, a higher amount of partially assembled tubes and a smaller portion of residual free CP were found, when the S3'$_1$/RNA hybrid was incubated at 25 °C or 30 ° for 2 h. Additionally, determination of nucleoprotein concentration by UV-Vis spectroscopy after sedimentation of products *via* ultracentrifugation, confirmed that the

1.5-fold number of nanotubes were assembled, when the RNA was not partially denatured prior assembly initiation at 65 °C. The experiments suggested that lower hybridization temperatures (25 °C or 30 ° for 2 h) avoid assembly-incompetent RNA folding states and improves the total assembly yield of the desired nucleoprotein tubes. Similar results were found for blocking the assembly at RNA sites 5' of the OAs at 15 °C after hybridizing the stoppers S5'$_{4\text{-}9}$ at 30 °C, 2 h: the 1.5-fold amount of assembled TLPs were generated (***Fig. 4-13b***). Furthermore, partially assembled particles, stalled by S5'$_6$ and S5'$_7$ were produced with a higher yield (60 % and 43 %) compared to the ones after hybridizing the stoppers at 65 °C (28 % and 24 %). As the yield of nanotube fractions blocked by stoppers S5'$_4$, S5'$_5$, S5'$_8$ and S5'$_9$ were roughly estimated to 10 %, those stoppers were not further evaluated. However, applying the milder conditions appropriate for hybridizing 5' stoppers (30 °C) to the blocking at different sites 3' of the OAs (S3'$_1$, S3'$_5$, S3'$_9$, S3'$_{t3}$), the number of suitable 3' stoppers was extremely reduced, as only S3'$_1$ and S3'$_5$ showed stopped TLPs (see *Appendix* ***Fig. A-6b***). The other 3' stoppers had no effect on the elongation with CP at 25 °C after hybridizing stoppers at 30 °C and resulted in fully encapsidated particles. Hence, it was implied that the RNA structure downstream of the OAs mostly required partial denaturation at 65 °C to make it accessible for the interaction with stoppers consistently with the previous study on several sets of 3' stoppers.

To combine 3' and 5' stoppers in a simultaneous procedure for generating multiple subdomains on TLPs, S3'$_1$ and S3'$_5$ that both efficiently hybridized to RNA at 30 °C were tested to find out whether they successfully stalled the encapsidation at the lower assembly rate enforced at 15 °C. Native gel electrophoresis indicated that the blocking efficiency of S3'$_5$ was slightly enhanced and resulted in ≈ 100 % of the desired fraction of partially assembled nanotubes (***Fig. 4-13c***). In contrast, assembly products of RNA/S3'$_1$ showed two incompletely encapsidated, smaller nucleoprotein tube fractions in addition to the usual one after native electrophoretic separation. If, however, S3'$_1$ was bound to the RNA with the standard procedure (65 °C, 5 min), subsequent encapsidation with CP at 15 °C resulted in stalled nanotubes of the desired form (see *Appendix* ***Fig. A-6c***). It was found that S3'$_1$ may hybridize to an additional 5' site at the wt-RNA (see ***Fig. 4.1b*** and *Appendix* ***A1***). Since the probability of binding to this additional site is enhanced using milder hybridization temperature, the additional smaller, partially assembled TLPs may result from the second blocking position induced by the unusual low hybridization temperature (30 °C) without the displacement of the stopper due to decreased assembly rate at 15 °C (***Fig. 4-13c***). In conclusion, different stoppers, targeting sites 5' and 3' of the OAs on wt-RNA, were studied in respect of their stop-competence using various temperature conditions for both partial denaturation/stopper hybridization and nucleoprotein tube

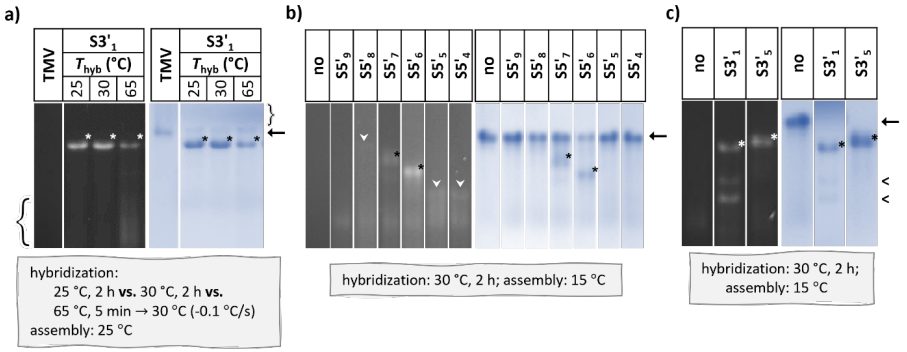

Figure 4-13 Application of milder reaction conditions. Visualization of "stop" state after nanoparticle separation on native agarose gels. Black/white asterisks (*) label bands with higher electrophoretic mobility. The arrows indicate bands of fully assembled tubes as confirmed by the individual control samples, TMV or fully assembled nanotubes scaffolded by RNA devoid of stoppers (no), respectively. **(a)** Comparison of three distinct protocols (depicted below the image, T_{hyb}: highest temperature during hybridization reaction) for binding S3'$_1$ to RNA. The brackets at the lower left side indicate RNA in assembly-incompetent folding state, whereas the brackets at the upper right side highlight residual free CP. Fragments were separated on a 1.5 % agarose gel. **(b+c)** Milder hybridization of the various stoppers, 5' **(b)** as well as 3' **(c)** of OAs, followed by lower assembly temperature was performed as depicted below the gel. White triangles indicate a faint EtBr signal corresponding to those bands, however, their Coomassie Brilliant Blue signal is below the visualization limit. The two arrow heads indicate the additional two fragments with higher electrophoretic mobility.

elongation.

Four (S5'$_{2, 3, 6, 7}$) out of nine 5' stoppers were unequivocally identified to stall the elongation of the nucleoprotein complex with efficiencies ranging from 43 % to 65 % using respective stop-and-go conditions. In contrast, ten out of twelve 3' stoppers were found to influence the self-assembly with varying performance (ranging from 30 % to 100 %) using standard conditions. The milder the temperature during hybridization, the higher the overall assembly yield independent of the blocking site, but only S5'$_6$, S5'$_7$, S3'$_1$ and S3'$_5$ were found to bind to RNA at 30 °C most likely due to the formation of complex RNA secondary structures. Reducing the assembly rate enhanced the blocking efficiency of hybridized 5' stoppers and thus the portion of stalled TLPs (see ***Table 4-2*** for a compilation of blocking efficiencies). The values of blocking efficiencies were averaged over minimally three independent experiments. Different RNA and CP preparations were tested with the respective conditions in hybridization and assembly, however, stopper aliquots of only one stopper stock were used. Thus, the individual differences in blocking efficiencies between the various stoppers could be concomitant with individual stopper stocks that might not be perfect (Temsamani et al. 1995). All stoppers were configured using design rules adapted from PCR primer (Dieffenbach et al. 1993) as well as from strand displacement design (Yurke and Mills 2003; Zhang and Winfree

2009). Those rules seemed to be insufficient for the prediction of suitable stopper positions due to various reasons. On the one hand, secondary structures within the long RNA sequence may be insufficiently denatured so that even if a stopper is partially bound by a few nucleotides to the RNA the RNA-RNA intramolecular hybridization could not be displaced in the relevant native folded structures. On the other hand, even if the stopper could completely bind to the desired position, the assembly rate plays a crucial role in a successful blocking event. The effect of the assembly rate was experimentally investigated using different denaturation/stopper hybridization and CP assembly conditions as well as various divalent cation concentrations. A route was found to stabilize the DNA/RNA hybrids during self-assembly with CP to stop nanotube growth at the predicted sites, in order to generate multiple domains in directions 5' and 3' of the OAs (*e.g.*, S5'$_6$, S3'$_5$). However, some stoppers did not efficiently stall the encapsidation using those conditions (***Table 4-2***). As the experimental trial-and-error method is challenging and time-consuming, a better prediction for useful stopper binding sites was required.

Tab. 4-2 Overview over blocking efficiencies of the various stoppers at the diverse workflows

Stopper			Blocking efficiency (%) [a]			
name	position [b]	T_{hyb} T_{ass}	65 °C 25 °C	65 °C 15 °C	30 °C 25 °C	30 °C 15 °C
S5'$_9$	405 - 426		-	0	-	0
S5'$_8$	613 - 634		-	5	-	10
S5'$_7$	827 - 848		-	24	-	43
S5'$_6$	1527 - 1548		-	28	-	60
S5'$_5$	2217 - 2239		-	18	-	10
S5'$_4$	2262 - 2283		-	14	-	10
S5'$_3$	5189 - 5219		25	65	-	-
S5'$_2$	5194 - 5215		25	58	-	-
S5'$_1$	5268 - 5289		5	25	-	-
S3'$_1$	5533 - 5555		100	100	100	84$^{\#}$
S3'$_2$	5671 - 5692		30	-	-	-
S3'$_3$	5733 - 5754		85	-	-	-
S3'$_4$	5739 - 5762		50	-	-	-
S3'$_5$	5761 - 5784		95	-	95	100
S3'$_6$	6159 - 6183		0	-	-	-
S3'$_7$	6169 - 6205		60	-	-	-
S3'$_8$	6178 - 6201		60	-	-	-
S3'$_9$	6183 - 6205		100	-	0	-
S3'$_{t1}$	6323 - 6344		0	-	-	-
S3'$_{t2}$	6333 - 6355		100	-	-	-
S3'$_{t3}$	6338 - 6359		100	-	0	-

[a] equates to the amount of partially assembled products calculated by analyzing nanotube separation in native gels. All amounts were determined at a 25-fold molar excess of stopper over RNA (see in *Appendix **A2*** for details). "-": not determined; [b] in respect of the sequence position in RNA; $^{\#}$ only the S3'$_1$-single-blocked assembly product was considered.

4.3.4 RNA accessibility – a folding simulation study

The previous results implied that the long wt-RNA sequence may site-specifically differ due to the secondary and tertiary intramolecular folding. Hence, the challenge to efficiently bind stoppers to their target is, to find sections in the RNA that are accessible for stoppers due to weak interactions with other RNA sequence parts or that more complex spatial structures could be unfolded, e.g., by way of a temperature-profile applied. This local RNA accessibility was therefore explored by correlating stop-and-go experiments with software-based folding simulations of the applied stopper binding positions, to improve the previously used design rules.

A wide range of RNA folding software with many different functions (simulation of secondary and tertiary structure, in-/excluding pseudoknots) is available.

Only a few of those tools enable simulation of long RNA sequences, like the web-based software `RNAfold` (version 2.4.18, http://rna.tbi.univie.ac.at/cgi-bin/RNAWebSuite/RNAfold.cgi; hereinafter referred to as `RNAfold`) (Gruber et al. 2008; Lorenz et al. 2011). `RNAfold` releases information about the minimal free energy (MFE) structure simulated at variable temperatures; but calculations that deviate far from 37 °C are unreliable. However, to enable a good correlation to experimental results, the RNA sequences required folding at various temperatures. For this purpose, the web server `mfold` (version 2.3, http://www.unafold.org/mfold/ applications/rna-folding-form-v2.php; hereinafter called `mfold`) (Zuker 2003) was used that simulate the folding using selectable temperatures, but is limited to sequences up to 2400 nt. As it is furthermore expected that larger RNA (> 6000 nt) folds into locally stable secondary formations which deviate from the MFE structure (Fallmann et al. 2017) and smaller RNAs (≤ 1000 nt) are predicted more accurately, in a first approach the wt-RNA sequence of interest and parts of this sequence of 1000 nt length were simulated to find the most stable secondary structure. This approach is adapted from Scherr et al. (2000) who confirmed with a computer-aided analysis experimental investigations on finding RNA sequences that were accessible for antisense nucleic acids to sequence-specific inhibit gene expression (Scherr et al. 2000; Patzel et al. 1999).

Since 5' stopping is dependent on the control over assembly rate, here, predominantly the 3' stopper positions were considered in the 4396-6395 nt RNA section. Additionally, eight intervals shifted by 250 nt were investigated: Five intervals of 1000 nt length, in contrast, the last three intervals were also shifted by 250 nt but with varying length of 750 nt, 500 nt and 250 nt, respectively (for a scheme see ***Figure 4-14a***). The stopper positions were covered each by five sequence sections. All simulations were performed by `mfold` at 65 °C, as extensive experimental data were gained for

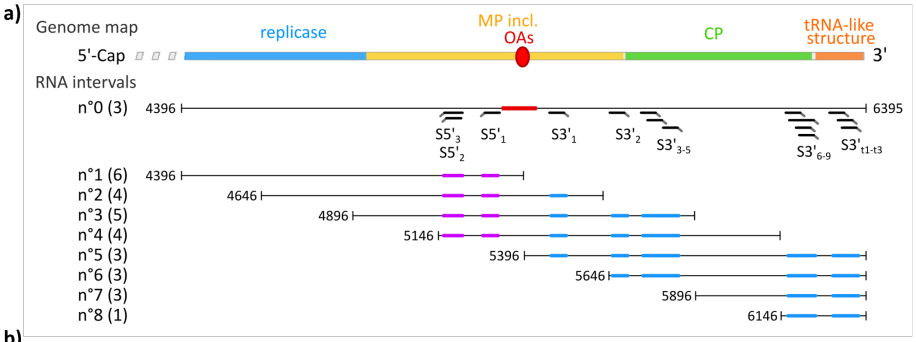

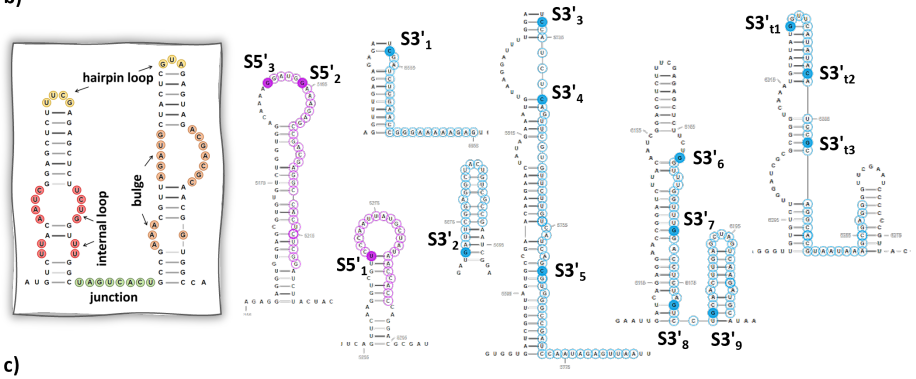

c)

Stopper name	S5'$_3$	S5'$_2$	S5'$_1$	S3'$_1$	S3'$_2$	S3'$_3$	S3'$_4$	S3'$_5$	S3'$_6$	S3'$_7$	S3'$_8$	S3'$_9$	S3't$_1$	S3't$_2$	S3't$_3$
Frequency (%) [a]	59	59	95	90	100	61	61	56	92	92	92	100	100	100	100
Stopper length (nt)	31	22	22	23	22	22	24	24	25	37	24	23	22	23	22
Number of nucleotides involved in diverse *structural elements*															
**hairpin loop*	12	7	14	-	4	-	-	-	-	5	5	5	3	-	-
**bulge/internal loop*	3-1-1	3-1	1	2	1-1	3-1-2	1-2-2-1	1	1-2-1-1	1-1-1-1	1	1-1	-	-	1
**junction*	-	-	-	11	-	-	-	12	1	1	1	-	-	6	6
accessible nt	17	11	15	13	6	6	6	13	6	10	7	7	3	6	7
double strand	14	11	7	10	16	16	18	11	19	27	17	16	19	17	15
Blocking efficiency [b]	25	25	5	100	30	85	50	95	0	60	60	100	0	100	100

Figure 4-14 (a) Scheme of RNA sequence interval in respect to the genome map. The cipher in brackets illustrates the total count of resulted structures of the respective interval number n°x. Stopper positions are depicted by colored lines. **(b)** Cartoon of exemplary structural elements (left). Predominant secondary structure of the individual stopper binding sequences, visualized with the web based RNA2Drawer app (Johnson et al. 2019) (right). The stopper binding sequences are highlighted by colors, the filled circles indicate the start of each sequence.**(c)** Overview over frequency of preferred secondary structure and nucleotides involved in the different structural elements. [a] Frequency of the predominant secondary structures resulted from the MFE and suboptimal structures for the sequence intervals; * types of structural elements accessible for hybridization; [b] equates to the amount of partially assembled products calculated by analyzing nanotube separation in native gels. All amounts were determined at a 25-fold molar excess of stopper over RNA (see in *Appendix **A2*** for details). Drawings not to scale.

the standard hybridization procedure. Folding the 3' terminal third (n°0: 4396-6395 nt) resulted in an MFE structure and two suboptimal structures. Comparing the three foldings within the region of interest, *i.e.*, at the stopper binding positions, those differed only to a minor degree. Simulation of the eight intervals resulted in MFE secondary structure as well as a different number of suboptimal foldings (3 to 6). All simulations were compared at the specific stopper sites in respect of the secondary structure elements.

As nucleotides involved in hairpin loops, bulges, internal loops, and junctions are presumed to be accessible in the hybridization event, whereas double-stranded regions are the most stable parts (pseudoknots and kissing hairpins were not considered in `mfold`), the mostly conserved secondary structure (***Figure 4-14b***) for each stopper target position was analyzed and represented with the frequency of appearance in ***Figure 4-14c***. Those structure formations that were more conserved may be of higher probability of being the preferred structure. The predominant secondary structure of the individual stopper binding site was found in all MFE structures.

The number of nucleotides that are presumed to be accessible for hybridization seemed to be a crucial factor. RNA sequences with > 6 nt distributed to bulges, internal loops, hairpin loops and/or junction were accessible for stopper binding and experimentally resulted in blocking efficiencies of 30 %, 85 % and 100 % for S3'$_2$, S3'$_3$ and S3'$_{t2}$, respectively. However, the target position of S3'$_6$ also showed six predicted, accessible nucleotides, but no effect on stalling during the assembly was found. Hence, not only the total number of nucleotides that are accessible is critical moreover the number of continuous accessible bases plays the key role. For example, S3'$_3$ and S3'$_4$ exhibit six accessible nucleotides but differ in their blocking efficiencies (85 % and 50 %). As three of the accessible nucleotides within the S3'$_3$ position were involved in a huge bulge, those nucleotides were presumably rather available for hybridization than two positions of two continuous nucleotides in a bulge of the target site of S3'$_4$, visualized by the interrupted notation in ***Fig. 4-14 c***.

Analysis of complementary positions of S5'$_{1,2,3}$ showed that sufficient nucleotides may be accessible when partially denatured. However, as it was shown in the previous part, blocking was only efficient when the assembly rate was reduced.

Since only minor differences were found between the smaller intervals of 1000 nt and the 3' terminal third region (4396-6395 nt), a further evaluation of this region in `mfold` at 30 °C was performed, to compare the secondary structures simulations with experimental results of hybridizing stopper S3'$_1$, S3'$_5$, S3'$_9$ and S3'$_{t3}$ at 30 °C. Furthermore, to evaluate differences between a full-length RNA simulation with the shorter section, additionally wt-RNA was folded in `RNAfold` at 30 °C. `RNAfold` simulation of full-length RNA resulted only in the MFE structure. In contrast, `mfold`,

calculated the MFE and 19 suboptimal structures. Here, the most conserved structures of stopper target sites S3'$_1$, S3'$_5$, S3'$_9$ and S3'$_{t3}$ varied in their frequencies (70 %, 89 %, 96 %, 44 %) but all were found in the MFE structures (see ***Tab. A-2***). `RNAfold` secondary structures differed from `mfold` simulation in respect of the target sites of S3'$_1$, S3'$_5$ and S3'$_{t3}$. Only the predicted secondary structure of S3'$_9$ site was identical for both, `RNAfold` and `mfold`, simulations and was like foldings at 65 °C. Applying the before-presumed rules, all stopper binding sites may accessible adapted from `mfold` calculations at 30 °C, which was contradictory to experimental results. However, S3'$_{t3}$ may not be accessible according to `RNAfold` structure confirming no blocking effect of this stopper concordantly with experimental results. Hence, `RNAfold` could likely give a better insight into foldings of a longer sequence, however, due to the lack of pseudoknot prediction the probably correct structure for all stopper sequences was not displayed.
In conclusion, comparing folding simulation data of secondary structures with experimental results at the various temperatures, did not offer concrete evidence for efficiently improved prediction routes for best-choice stopper sequences. Moreover, as no significant differences were found between the secondary structure elements simulated at 65 °C *versus* 30 °C, conformations like pseudoknots or kissing hairpins could have a major impact.

This chapter introduced the challenging and complex search for convenient stoppers. Diverse conditions were tested to hybridize stoppers to RNA as well as to produce partially assembled particles mediated by a stopper. The application of defined design rules for DNA oligonucleotides were insufficient to predict appropriate blocking elements. A complex RNA structure hinders binding of stoppers to particular sequences and so far, procedures to unravel those structures were not identified. However, it was shown that numerous DNA strands can effectively bind to specific sites, 5' as well as 3' of the OAs, using individual adapted procedures. Investigations on local RNA accessibility by web-based software tools in correlation with experimental results revealed deeper insight to RNA sequences that were available for stoppers during hybridization procedure. Consequently, a better approach for the prediction of suitable binding sites is the modulation of the RNA formation at local sites in combination to established design rules.
These studies pave the way for further exploration to generate multiple domains on a single TMV-like nanotube, by simultaneous stop-and-go assembly.

4.4 Development, analysis, and functionalization of multiple domains

The previous chapter revealed various viable 5' and 3' stoppers using respective stop-and-go conditions. However, to generate multiple domains on a single TMV-like nanotube, several stoppers need to be used in a concurrent and successive elongation process. In the following section, two routes for the simultaneous hybridization of two stoppers to wt-RNA and the subsequent stepwise stop-and-go assembly were developed towards the generation of nanotubes with three distinct and precisely defined CP domains (3-DTLPs). These custom tailored 3-DTLPs were used to explore their advantage to spatially order biomolecules for applications as templates for artificial multienzyme complexes or biosensors. Therefore, two types of differently arranged 3-DTLPs induced by two 3' stoppers as well as by a 5' and a 3' stopper, respectively, were site-specific conjugated with enzymes or antibodies and investigated in respect of the integrity and localization of selectively coupled biomolecules.

4.4.1 Two-enzyme cascade on Cys-wt-Lys$_{Bio}$-TLPs (261-30-9)

In a proof-of-concept experiments Cys-wt-Lys$_{Bio}$-TLPs (261-30-9) were explored whether they can serve as a suitable template for a two-enzyme cascade. For this purpose, two effective 3' stoppers, S3'$_1$ and S3'$_9$ (binding sites depicted in ***Fig. 4-10***, **Chapter 4.3**), were simultaneously hybridized to wt-RNA with their preferred procedure (65 °C → 30 °C (-0.1 °C/s)), followed by assembly of the first long 5' domain (261 nm) at 25 °C with CP$_{Cys}$. After UC purification (113 000 *g*, 2 h) the pellet was resolved, and the second domain of nucleoprotein tubes was formed by addition of wt-CP as well as the corresponding release strand R3'$_1$. The mixture was again centrifuged (95834 *g*, 2 h) to remove residual unbound wt-CP as well as the various DNA oligomers with the supernatant. To generate the last and shortest domain of 9 nm, S3'$_9$ was supplanted by R3'$_9$ to the resolved pellet and the preformed partially assembled tubes were incubated with CP$_{Lys\text{-}Bio}$ (see ***Fig. 4-15a*** *for a schematic illustration*). The final UC (95834 *g*, 1.5 h) removed residual CP$_{Lys\text{-}Bio}$ as well as displaced stopper and release strands.

In the preliminary studies, TEM analysis revealed reliable length data and differentiation of two divergent domains. However, large enzymes bound onto small domains with 50 % biotin moieties gave inconclusive results and even small molecules, like avidin were not clearly identified if coupled to short domains of 10 nm. Hence, to monitor the successive stop-and-go assembly *via* native gel electrophoresis, a control sample was prepared with wt-CP using the same conditions but without the exchange of proteins (***Fig. 4-15b***). The intermediate samples identified effective blocking

at the desired site of S3'$_1$ resulting in one major fraction of partially encapsidated tubes. After toe-hold-mediated release of this DNA strand by R3'$_1$, the assembly was again stopped at the S3'$_9$/RNA hybrid position visualized by an electrophoretic shift to longer tubes with residual RNA tail unlike from full-length TLPs. After the third assembly step, S3'$_9$ was effectively displaced by addition of the respective release oligomer R3'$_9$ as a concrete band of completely encapsidated TLPs was found. As the separation of the diverse intermediate products clearly indicated an effective stop-and-go assembly with a low possibility to form by-products using these stoppers and conditions, the as-produced Cys-wt-Lys$_{Bio}$-TLPs (261-30-9) were explored whether they could be applied as suitable templates in enzymatic cascade assays. A well-established two-enzyme system is the combination of glucose oxidase (GOx) with horseradish peroxidase (HRP) for the detection of glucose and it was intensely investigated immobilized to full-length TMV$_{Cys}$ in a colorimetric assay (Koch et al. 2015; Bäcker et al. 2017). To apply this two-enzyme system also to the 3-DTLPs, a heterobifunctional maleimide-PEG$_{12}$-NHS linker was covalently bound to the lysine residue of GOx ([mal]-GOx), whereas HRP was used as a commercially available streptavidin-conjugate ([s]-HRP). [s]-HRP and [mal]-GOx selectively addressed the biotin moieties of the smallest CP$_{Lys\text{-}Bio}$ domain as well as the long CP$_{Cys}$ part, respectively, in a simultaneous incubation at 22 °C, 2 h. Subsequently, the unbound enzymes were separated by UC. The presence as well as the integrity of enzymes on the adapter tubes were tested by a colorimetric assay in solution (Koch et al. 2015). Glucose and chromogenic ABTS served as educts and the final conversion into the colored oxidized ABTS* was spectrophotometrically analyzed at λ = 405 nm. The concentration of the end-product was estimated from absorbance values and illustrated over time (***Fig. 4-15c***). The absorption of TMV at λ = 405 nm in a solution of similar amounts was measured to define the background given by non-decorated TMV nanotubes. The samples containing the enzyme cascade resulted in increased ABTS* concentration with the time. A maximal detectable concentration of 160 µM was reached after 11.5 min for 200 ng of enzyme carriers, whereas in the same period the half amount of enzyme-bound DTLPs yielded 80 µM indicating that both measurements were consistent. This enzyme activity test confirmed the integrity of GOx and HRP after conjugation to the carrier sticks by a covalent thioether bond and affinity-coupling, respectively. Furthermore, those results provided indirect evidence of two enzyme-loaded domains separated by an interjacent third segment of 30 nm.

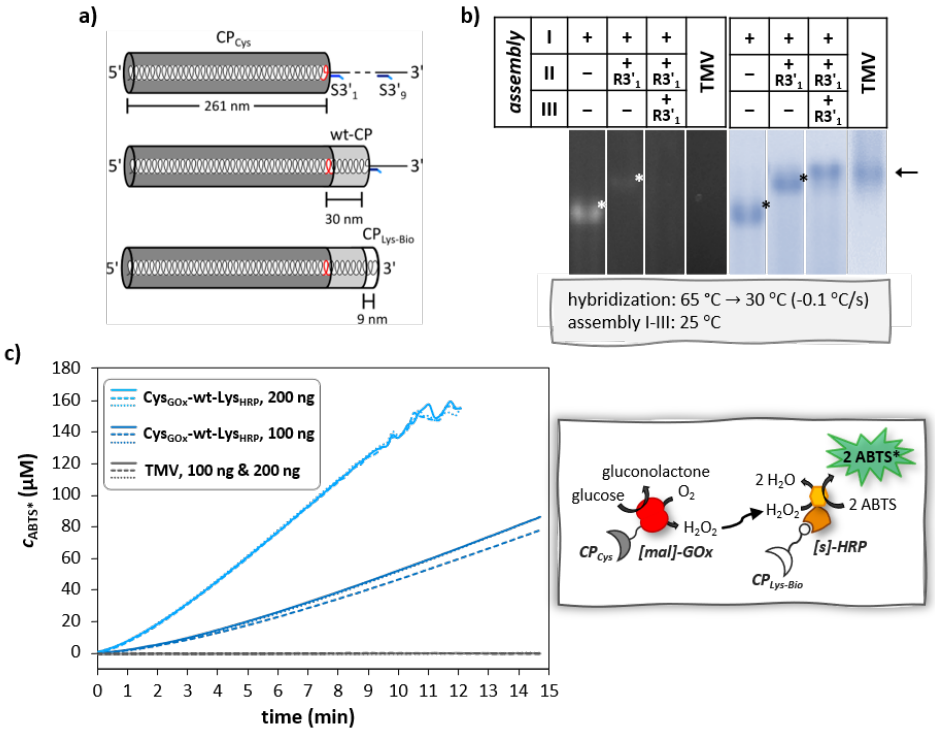

Figure 4-15 (a) Scheme illustrating the distinct states during the stepwise formation of nanotubes mediated by the different stoppers S3'$_1$ and S3'$_9$. The length as well as the protein type of the domains are depicted at each product. Drawings are not to scale. **(b)** The successive stop-and-go assembly was monitored by nanoparticle separation in a native agarose gel. Simultaneous hybridization of S3'$_1$ and S3'$_9$ as well as assembly were performed as depicted below the image. The arrow indicates bands of fully assembled tubes confirmed by TMV. Black/white asterisks (*) label bands with higher electrophoretic mobility. **(c)** Conversion of glucose and ABTS by the two-enzyme cascade GOx/HRP immobilized on 3-DTLPs, visualized in the cartoon (right). Left: Estimated concentration of ABTS* from measured A_{405} over 15 min. Three technical replicates of two different amounts of enzyme-conjugated 3-DTLPs as well as of the control sample (TMV) were determined. For further details see text.

4.4.2 Immunomarking and detection of distinct domains on Cys-wt-Lys$_{Bio}$-TLPs (72-199-29)

Immunomarking offers another route to generate artificial enzyme complexes on a carrier that is immobilized on a substrate. To ensure reliable visualization of different sections on those nanoobjects, TMV-like particles with three desired, asymmetric CP domains were prepared using a 5' and a 3' stopper that block the assembly with greatest impact using the same conditions. The highest blocking efficiencies at RNA positions, 3' as well as 5' of the OAs, using the combination of milder hybridization conditions and lower assembly temperature were achieved by S3'$_5$ (blocking efficiency: ≈ 100 %) and S5'$_6$ (blocking efficiency: ≈ 60 %), respectively (binding sites depicted in ***Fig. 4-10***, **Chapter 4.3**). The combination of both stoppers may generate 3-DTLPs with a 5' terminal, a center and the 3' domain of distinct length of 72 nm, 199 nm and 29 nm, respectively. This asymmetric formation enables the differentiation of antibody-conjugated domains *via* atomic force microscopy (AFM).

In the following, an appropriate protocol was developed, to combine both stoppers in a simultaneous reaction for producing 3-DTLPs. So far, the stop-competences of S3'$_5$ and S5'$_6$ were studied in individual samples using similar conditions. It was found that the as-produced assembly products differed in their sizes of the nucleoprotein domain as well as in the residual RNA length (for a scheme see ***Fig. 4-16a***). Since the 5' terminal RNA tail of the RNA/S5'$_6$ construct is folded back into the inner channel of the protein tube, the length is only roughly estimated (for an exemplarily calculation see *Appendix **A2***). However, the resulting arrested nanotubes might be discriminable *via* native gel electrophoresis due to the deviating sizes and the unequal negative net charges of the free RNA. The simultaneous hybridization of S3'$_5$ and S5'$_6$ to wt-RNA, followed by partial encapsidation may result in the shortest nucleoprotein tube with the highest negative charge in comparison with the singly arrested products. Hence, this desired, 3' and 5', blocked product might be distinguishable from the other fractions in the native agarose gels. As the findings of studies on 5' stopping indicated high temperature-dependence in respect of the blocking capability, a temperature-controlled release was preferred for S5'$_6$, whereas S3'$_5$ required a DNA-mediated release due to its temperature stability. To find the appropriate release parameters, the stop-and-go procedure was successively investigated (***Fig. 4-16b***). Hybridization was performed at 30 °C, 2 h with both stoppers simultaneously. The first assembly step (I) was executed at 15 °C, 16 h, whereas the following steps were tested systematically at 25 °C (II) and 30 °C (III) for various time periods. Also, the use of the release oligomer R3'$_5$ was examined under distinct conditions. Native gel electrophoretic separation revealed for the first time simultaneously blocked nanotubes at a 5' and a 3' site relative to OAs, respectively, as another nucleoprotein complex with higher electrophoretic shift

was found in contrast to singly stopped TLPs. Furthermore, a successful temperature-induced release of S5'$_6$ was proven, either at 25 °C for more than 6 h or at 30 °C, 16 h. In contrast, S3'$_5$ was released to a minor degree at 25 °C, that was comparable to the previous results, but the impact of temperature-induced release increased at 30 °C, 16 h. Nevertheless, a suitable stop-and-go procedure could be established for the generation of asymmetric 3-DTLPs, since stopper S3'$_5$ efficiently

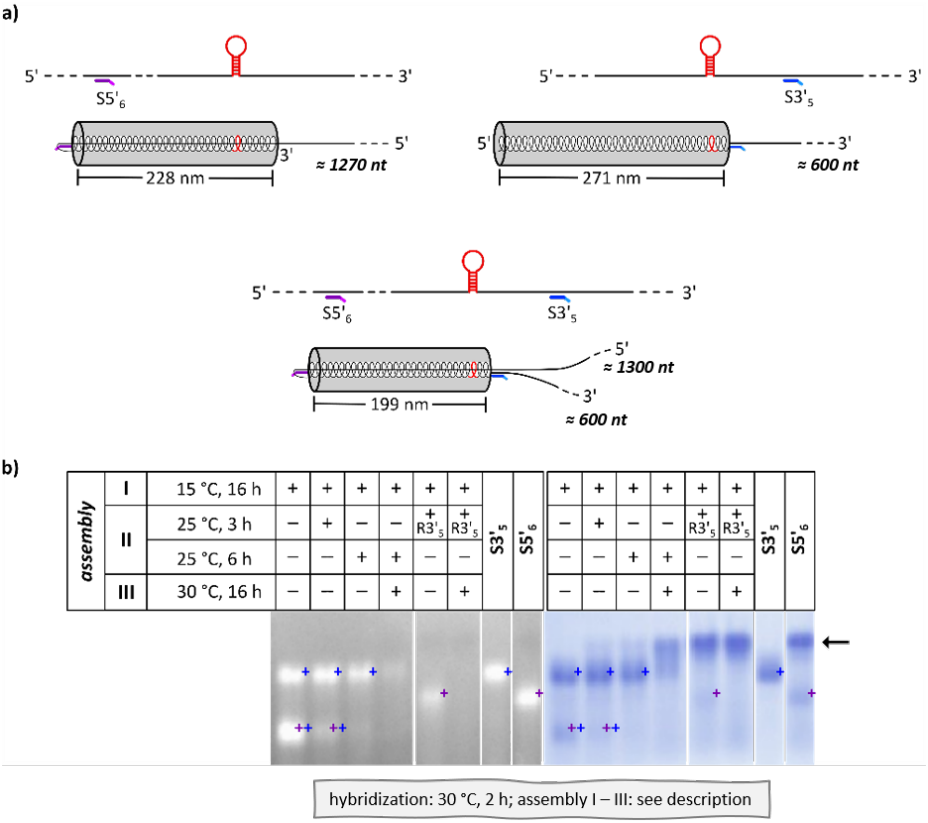

Figure 4-16 (a) Cartoons illustrating the distinct types of arrested nanotubes with the estimated non-encapsidated RNA portions (in nt) by the different stoppers S3'$_5$ and S5'$_6$, hybridized in single reactions and simultaneously to the RNA, respectively. The length of the partially assembled nucleoprotein tube is depicted below each product. Drawings are not to scale. **(b)** The "stop" and "go" states of 3-DTLP preparation were visualized by nanoparticle separation in a native agarose gel. Hybridization for all samples was performed as depicted below the image, followed by assembly indicated in the table. Two different control samples were prepared: partially assembled nanotubes, stalled by S3'$_5$ or S5'$_6$, respectively, assembled at 15 °C, 16 h. The arrow indicates bands of fully assembled tubes. Blue/purple "plus" label bands with higher electrophoretic mobility due to stopped assembly by S3'$_5$ (+), S5'$_6$ (+) or both, S5'$_6$ and S3'$_5$ (++).

arrested the encapsidation at 15 °C, 16 h and could be removed by a fully complementary release oligomer R3'$_5$ at 25 °C, concomitantly with stably blocking the assembly by S5'$_6$ at its 5' position. In a subsequent step, S5'$_6$ was displaced temperature-induced 16 h at 30 °C. Here, the procedure for stop-and-go using S3'$_5$ and S5'$_6$ was examined without any purification step in between, thus, particles were filled up with the residual wt-CP, that was still present in the reaction solution.

To generate DTLPs with three differently addressable CP domains, tightly defined in their longitudinal length and arrangement, a proof-of-concept experiment using the before-examined reaction conditions complemented by purification steps (to exchange the CP variants) was performed. In the following section, the experimental procedure as well as the partial products and intermediates are described (for a scheme see ***Fig. 4-17a***).

Simultaneous hybridization of S3'$_5$ and S5'$_6$ to RNA was performed at 30 °C, for 2 h, followed by assembly at 15 °C with wt-CP (*step I*). Previous investigations on UC conditions have shown that the protruding RNA does not degrade and remains assembly-competent after resuspension of the intermediate products. Consequently, a first attempt using UC with increased speed was performed, to certainly sediment the different assembly products and to remove the non-assembled wt-CP as well as other small aggregates with a sedimentation coefficient below 89 S. As findings of native gel electrophoresis have shown, two different types of stalled tubes were produced: the desired ones (**I.1** in ***Fig. 4-17***) blocked at both sites, 5' and 3' as well as the by-product **I.2**, nanotubes only locked by S3'$_5$. The *assembly step II* was initiated by a toehold-mediated release of S3'$_5$, using the fully-complementary release-oligomer R3'$_5$ and the addition of CP$_{Lys\text{-}Bio}$ at 25 °C. Thus, the desired partially assembled nanotubes **II.1** with two different domains and an unencapsidated RNA portion due to successful assembly blockage by S5'$_6$ (wt-CP, 199 nm and CP$_{Lys\text{-}Bio}$, 29 nm) as well as two different by-products, **II.2** and **II.3** were assembled. **II.2** resulted from S3'$_5$-arrested tubes and were completed with the second CP domain (2-DTLPs: wt-CP, 271 nm and CP$_{Lys\text{-}Bio}$, 29 nm), whereas **II.3** was constituted when S5'$_6$ was supplanted from its site 5' of the OAs due to the temperature increase in this second assembly step. Subsequently, the particles were completed, 5' as well as 3', with CP$_{Lys\text{-}Bio}$ (**II.3**, 3-DTLPs: CP$_{Lys\text{-}Bio}$, 72 nm; wt-CP, 199 nm; CP$_{Lys\text{-}Bio}$, 29 nm). In the third assembly step (*assembly step III)*, S5'$_6$ was detached using the temperature-induced release at 30 °C and CP$_{Cys}$ was added to form the last differently addressable domain of the desired product **III.1** (3-DTLPs: CP$_{Cys}$, 72 nm; wt-CP, 199 nm; CP$_{Lys\text{-}Bio}$, 29 nm). All nanotubes were concentrated *via* UC, whereas the residual CP$_{Cys}$ aggregates as well as other molecules below 110 S were removed. The concentration of the nucleoprotein tube mixture was estimated by UV-Vis spectrophotometry and yielded 140 µg. This was equivalent to 14 % of the possible assembly product, calculated in

respect to the utilized RNA (50 µg). To evaluate the percentual composition of the individual assembly steps, three independent equivalent samples were prepared in parallel without exchanging the CP variant in between the procedure and were analyzed *via* native gel electrophoresis. The percentual amount of each assembly product was estimated from the distinct gel images *via* the software ImageJ (***Fig. 4-17b***).

a)

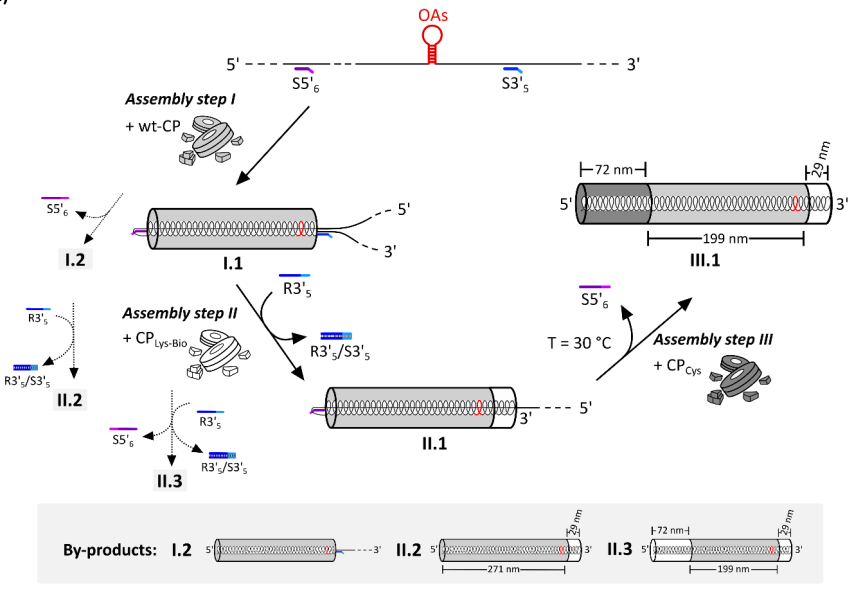

b)

assembly step I			*assembly step II*			*assembly step III*		
fraction [a]	product [b]		fraction [a]	product [b]		fraction [a]	product [b]	
60 %	60 %		84 %	60 %		100 %	60 %*	
40 %	40 %			24 %			24 %	
			16 %	16 %			16 %*	

Figure 4-17 Evaluation of stop-and-go protocol with 5' and 3' stoppers. **(a)** Scheme of the procedure for 3-DTLPs preparation (not to scale). The assembly steps *I* to *III* are illustrated with the individual addition of CP variants. Potential routes of producing the by-products are depicted in grey with numbers I.2, II.2 and II.3 and are illustrated below the scheme. See text for further details. **(b)** Estimation of product yield from native gels *via* the software ImageJ, averaged from three independent experiments. [a] percentual amount/fraction (particles with the same size), for an exemplarily calculation see *Appendix* ***A2***. [b] percentual amount of product: in respect to the before estimated product/fraction, *both products cannot be distinguished *via* AFM.

Since the behavior of the various intermediates and by-products during ultracentrifugation was not simply predictable, the arrested nanotubes of *assembly step I* were centrifuged using the diverse parameters that were also utilized for generating 3-DTLPs (for a scheme and results see *Appendix **Fig. A-7***), to prove whether the predicted configurations were still present in the mixture. The resulting pellets as well as supernatants were subsequently separated by native gel electrophoresis. Although the rotational speed of the first centrifugation step provides the lowest *g*-force, the resuspended pellet **#2** showed fractions of both arrested nucleoprotein products **I.1** and **I.2**, whereas the supernatant contained the residual CP (**#3**). This supernatant was centrifuged again with higher *g*-force in a second step. Here, no visible pellet was obtained (**#4**) by removal of the liquid (**#5**). However, the UC glass was filled with resuspension buffer and an aliquot was applied to native gel. The similar behavior was observed for the third centrifugation step (**#6** and **#7**). As the samples **#3** to **#7** did not show any fraction of nucleoprotein tubes, the yield of arrested tubes in the resuspend pellet **#2** was roughly estimated by UV-Vis spectrometry that confirmed that the total yield was sedimented with the parameters used after the first assembly step. This indicated that the sedimentation coefficient of all intermediates and by-products seems to be ≥ 110 S. Consequently, all products and by-products remained in the reaction mixture with the before-established procedure of generating 3-DTLPs. The residual RNA tail of the individual intermediates may shift the sedimentation coefficient to increased *S* values, so that smaller tubes with long residual RNA sedimented faster than fully assembled nanotubes of comparable length. However, the as-performed process was suitable to purify the mixture from the free CP variants, indeed as a mixture of 2- and 3-DTLPs. Further investigations on appropriate purification methods are necessary to generate pure samples of desired DTLPs by the separation of the diverse intermediates and by-products. Existing techniques to purify nucleoprotein complexes, for instance density-gradient centrifugation, analytical UC or size exclusion chromatography require studies using non-denaturing conditions as well as materials and parameters to protect the protruding RNA remaining the assembly-competence.

To explore the application of 3-DTLPs for the *in situ* fabrication of enzyme-cascades for atomic force electrochemical microscopy (AFM-SECM), the as-produced mixture of Cys-wt-Lys_{Bio}-TLPs (72-199-29) was analyzed stepwise *via* atomic force microscopy in tapping mode. The sample was diluted to visualize individual items of adsorbed nanotubes. Preliminary trials of *in situ* AFM imaging with various dilutions revealed that DTLPs were not present on the gold substrate (data not shown) when the sample remained in potassium phosphate buffer (PPB, pH 7.4) from incubation until imaging, as it was suggested for subsequent functional bio-affinity studies (Patel et al. 2017). These findings were in agreement with results found for TMV in PPB, pH 7.4 (Knez et al. 2004).

TMV is negatively charged using the before-mentioned condition and resulted in only small coverage on gold substrates.

Hence, to adhere DTLPs to the surface, the mixture was incubated 15 min at room temperature followed by washing, drying, and rehydration in PPB. This procedure enabled the visualization of DTLPs on the gold substrate *via* tapping mode by AFM imaging in buffer. However, the particles were not sufficiently stably adhered to the surface as the nanotubes were cut or detached by the AFM tip. This problem increased with higher resolution, thus, DTLPs were analyzed using lower resolution. The height of the well-adhered nanotubes was ≈ 15 nm that is smaller than the diameter of 18 nm determined by TEM. Since estimating the height of soft biomolecules *via* AFM imaging depends on the substrate as well as pH used, underrated heights typically appeared from objects compressed by the tip or by adhesive forces (Knez et al. 2004; Nault et al. 2015).

As an antibody-based method was used to visualize the $CP_{Lys\text{-}Bio}$ domain, blocking with bovine serum albumin (BSA) was applied to avoid unspecific binding of antibodies to the gold surface (for a scheme see ***Fig. 4-18a***). The sample was scanned in liquid *via* AFM after backfilling to serve as a reference and the rough surface showed successful binding of BSA (Patel et al. 2017). Various nanotubes were analyzed using the software Gwyddion in respect of their width and resulted in increased values (≈ 75 nm, see *Appendix* ***Fig. A-8a***) compared to TMV's native diameter. This overestimation of width is a characteristic tip convolution effect, an AFM artifact, induced by tip geometry. However, for further evaluation of DTLPs the width was not of high interest, and, in contrast, the length measurements were only affected to a minor degree. Full-length nanotubes were predominantly found after length measurements *via* the software ImageJ that revealed a median length of 300 nm and a size distribution similar to TEM analysis (for a histogram see *Appendix* ***Fig. A-8b***).

After analyzing the cross sections of particles, the measurements exhibited a height of ≈ 11 nm (exemplarily shown for particles 1, 2 and 3 in ***Fig. 4-18b***). In contrast to the height prior BSA coating, here it was reduced by ≈ 4 nm that is comparable to the dimension of a BSA monolayer that embedded the virus-like particles (Sugio et al. 1999; Wadu-Mesthrige et al. 1996; Patel et al. 2017). Furthermore, it seems as if BSA enhanced the stability of immobilization since fewer tubes seemed to be cut or detached by the AFM tip from the surface.

Immunomarking with an anti-biotin IgGs (α-biotin IgG) was applied to the same DTLP sample and various areas on the gold substrate were analyzed *via in situ* AFM imaging (***Fig. 4-18c***). In contrast to the native gel analysis, particles smaller than 300 nm with one highlighted domain were found (depicted by orange arrow heads in ***Fig. 4-18c***) indicating that the particles were damaged either

during preparation of the sample for AFM imaging or by the tip during scanning the surface. However, full-length particles with uniform heights as well as with terminal domains of enhanced size were found. Increased domains verified successful binding of α-biotin IgG to terminal $CP_{Lys\text{-}Bio}$ domains compared to the segment containing a CP variant lacking the biotin moiety. Consequently, drying the sample to immobilize nanotubes at the surface did not affect the biological functionality.

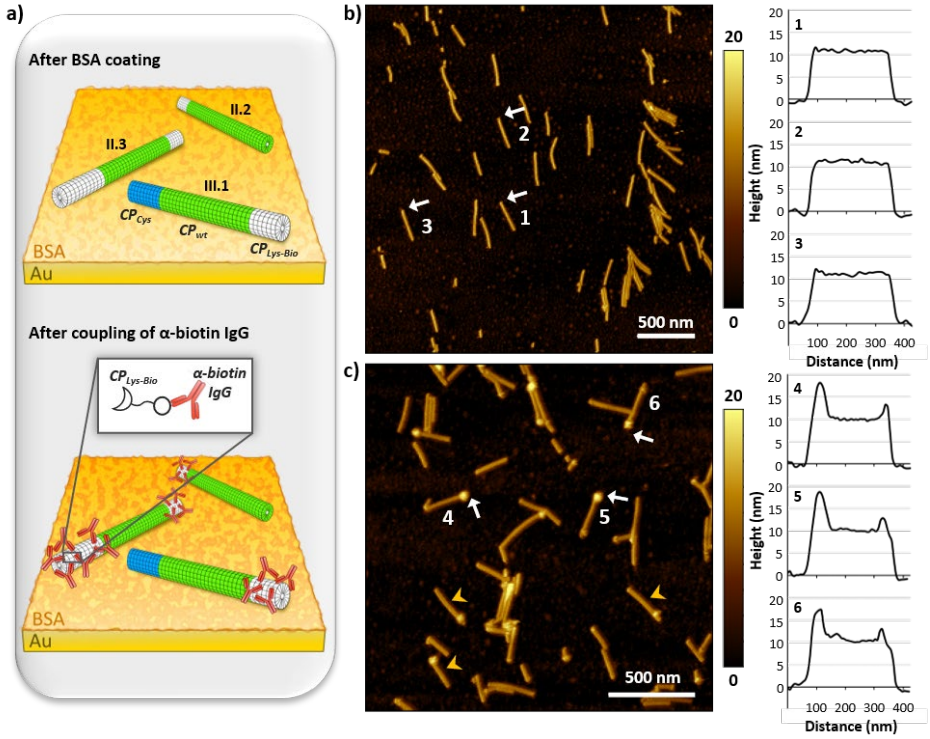

Figure 4-18 Visualization of $CP_{Lys\text{-}Bio}$-domain of TLPs by an antibody-based method *via* atomic force microscopy. **(a)** Schematic representation (not to scale) of DTLPs on the gold surface after BSA coating and after coupling of α-biotin IgG, respectively (from top to bottom). Numeration II.2, II.3 and III.1 are in accordance with ***Fig. 4-17*** and depict the various 2- and 3-DTLPs. **(b+c)** AFM images and exemplary height measurements of nanotubes adhered to a gold surface. The surface was blocked by BSA followed by washing with Milli-Q-water and immediate AFM imaging in PPB buffer (b). Subsequently, the sample was incubated with α-biotin IgG followed by washing with Milli-Q-water and immediate AFM imaging in PPB buffer (c). 1 to 6 indicate full-length DTLPs exemplarily analyzed, the white arrows show the starting point of the corresponding cross sections. The brighter signal in the topographic image and thus an increase of height confirms successful binding of anti-biotin IgG to the $CP_{Lys\text{-}Bio}$ domain. Orange arrow heads depict DTLPs smaller than 300 nm, lacking one terminal domain.

Based on the estimation of the resulting DTLP classes after native gel analysis (***Fig. 4-17***), around three-fourths of the full-length particles expose the shorter $CP_{Lys\text{-}Bio}$ domain, amenable to α-biotin IgG.

Since both types – DTLPs with three different CP variants (**III.1**) as well as the ones, only blocked by $S3'_5$ (**II.2**) – resulted in objects with one enhanced terminal domain after immunomarking, they cannot be identified using this method.

As a whole, the successful production of three defined domains on one single TMV-like particle was confirmed for nanotubes with two, 5' and 3' terminal, $CP_{Lys\text{-}Bio}$ domains (**II.3**) (exemplarily shown by DTLPs 4, 5 and 6 in ***Fig. 4-18c***). The analysis depicted an overall length of ≈ 300 nm as well as increased heights and widths of both terminal domains as expected. Furthermore, the fabrication of asymmetrical 5' and 3' terminal domains enabled the differentiation of both ends, although the detecting agent was the same. Topographic cross-sections visualized that the longer domain was concomitant with enhanced height (≈ 16 nm) in contrast to the smaller one (h ≈ 13 nm) caused by various number of coupling moieties due to their distinct lengths, 72 nm *versus* 29 nm. The longer interjacent parts of the nanotubes resulted in a similar height (≈ 11 nm) as prior affinity coupling and supported the previous completed formation of a BSA monolayer when backfilling the surface (Jeyachandran et al. 2009; Jeyachandran et al. 2010).

5 Discussion

The great need for nanoscaffolds that can carry different molecules at a tunable lateral distance in defined regions was highlighted in detail in the introduction and served as the basic motivation for this thesis. The straight TMV-like particles introduced here with their stiffness and two or three regions of selective reactivity to diverse coupling possibilities are good suitable building blocks to address these challenges of bionanotechnological applications. This work showed how dynamic DNA nanotechnology could be deployed to control the *in vitro* RNA-directed self-assembly of distinct viral CP types to generate "striped" DTLPs in a stepwise process. The established stop-and-go method uses DNA oligonucleotides (stopper) that bind reversibly at predefined sites at the RNA template to stop the encapsidation with TMV-CP at this DNA/RNA duplex position, and to allow CP exchange prior to stopper removal and resuming the assembly process. Dynamic DNA nanotechnology is usually used to build nucleic acid-based nanostructures for molecular sensing, drug delivery or as DNA nanomachines (see review: Bath and Turberfield 2007). To the best of my knowledge, this study was the first to combine strand displacement reaction with viral self-assembly to generate TMV-like nanotubes with two or three well-defined subdomains, which were evaluated for their suitability for two bionanotechnological applications, as an artificial two-enzyme complex in solution and as multiplex biosensors immobilized on gold surfaces in preliminary experiments. In addition to application-related aims of this thesis, the mechanisms of RNA-directed self-assembly and site-selective hybridization of DNA strands were further elucidated to better predict suitable stopper binding sites and reaction conditions for future work.

All in all, using wild type TMV-RNA and also heterologous RNA sequences, it was proven that it is indeed possible to stop RNA-assisted self-assembly of TMV-CPs in a site-selective manner using nucleic acid based technology, without covalent cross-linking of the DNA complement with the RNA, as it was previously reported in a study of TMV assembly (Fairall et al. 1986). This high stability of blocking already makes the stop method interesting for other applications, besides the generation of multiple domains. Using the blocking capability of stopper S3'$_9$, 291 nm long partially assembled tubes with accessible 3'-RNA tails were successfully produced for coupling with an organic synthesized branching element to produce 3D tetrahedral structures (see DNA stopper S2 in Wenz et al. 2018) and even the preparation of a short 10 nm 3' domain was possible. Also, S3'$_{t3}$ was used to produce nucleoprotein tubes with an exposed free RNA end at the 3' terminus for coupling

of further macromolecule types (see DNA stopper S1 in Wenz 2018, dissertation, manuscript III, p. 103).

Assembly termination on extensive secondary structures

To investigate the limitations of using the stop-and-go technique, in addition to small (< 10 nm) terminal and interjacent domains, the universality of the method was also investigated. Therefore, stoppers addressing a heterologous sequence of the *in vitro* transcribed hRNAs were used and investigated with respect to their stop-and-go competence. Three hRNAs were designed and the performed experiments showed stable blockage by a 3' stopper and successful restart of assembly after toehold-mediated displacement of the stopper by a respective release strand. However, assembly of hRNAs with TMV-CP revealed some additional by-products. Densitometric evaluation of the assembly products of hRNA III using the native gels revealed that the assembly truncation originated in the region transcribed from the F1 origin sequence. As this sequence pattern forms a hairpin in its native function (Hill and Petersen 1982; Ravetch et al. 1977; Tomizawa et al. 1977), it is indicated that it might form a spatial RNA structure that aborts the complete assembly as it has already been suggested in previous work that extensive secondary structures hinder a complete packaging of the RNA (Sleat et al. 1986; Gaddipati and Siegel 1990). This spatial structure could in addition impede the accessibility for h-S3'$_{2\text{-}4}$ to bind in this region since those stoppers aim fully or partially at this F1 sequence portion (schematically depicted in ***Fig. 4-8a***). Since the binding site of h-S3'$_1$ is upstream of this sequence, this stopper could stall the encapsidation. Nevertheless, these first experiments with hRNAs showed that RNA of TMV-foreign origin can be controlled in its self-assembly with TMV-CP by means of the same dynamic DNA-assisted procedures, provided that the hRNA itself is assembly-competent. Using appropriate purification methods for the isolation of the desired partially assembled nanotubes, oligodomain particles can also be prepared from synthetically designed RNAs.

5' stopping

In addition to successful stopping at hRNA as well as wt-RNA sites 3' of the OAs, suitable 5' stoppers were also identified to stall the assembly of nucleoprotein tubes scaffolded by wt-RNA when applying a reduced assembly rate by lowering the assembly temperature. For the mechanism of stopping in the 5' direction, it was assumed that the DNA/RNA duplex region cannot be pulled into the inner channel of the growing nanotube, as shown in a previous study (Fairall et al. 1986). However, clear length measurements by TEM of partially assembled nanotubes blocked at a 5' site are not available, so that the assumption could not be confirmed.

Challenges of analytical method

The stop-and-go technique bears a number of challenges, and the experimental methods as well as theoretical approaches possess limitations.

The analytical method, *i.e.*, native gel electrophoresis, that was used here preferentially reached its resolution limit at two points. Stoppers that produce small partially assembled tubes with low blocking efficiencies (*e.g.*, S5'$_1$ and S5'$_4$) could only be visualized by EtBr staining but the overlayed Coomassie Brillant Blue signal was not significant. In contrast, stoppers that blocked the assembly close to the RNA termini with low stalling capability (*e.g.*, S5'$_9$ and S3'$_{t1}$) showed stained protein, but this was not clearly distinguishable from the full-length tubes and lacked the RNA signal likely due to the short length of the RNA tail. Thus, the stoppers with inconclusive results were not further evaluated. Nevertheless, with this native gel electrophoretic protocol a fast overview over conditions applicable for the respective stoppers was achieved and gave insights into different intermediate states of the assembly as well as a quantitative impression of incomplete blocking and/or assembly events, most likely due to unfavorable RNA folding states.

Experimental view of RNA accessibility

As stoppers were designed using guidelines adapted from PCR primers (Dieffenbach et al. 1993) secondary structures, like hairpin formation and self-dimerization of stoppers were avoided (Kibbe 2007), sequences with melting temperatures were selected to achieve $T_m \approx 60$ °C and the length of stopper sequences was forced to have high selectivity and specificity. In contrast the strength of hybridization supported by a GC content > 50 % was dependent on the desired site, but had to be selected in a way that a subsequent release of stopper by a strand displacement reaction was possible and even the toehold length and composition was designed as it was suggested for strand displacement reactions (Zhang and Seelig 2011; Yurke et al. 2000; Yurke and Mills 2003).

As a whole, determination of blocking efficiencies showed that stopping was mainly independent of T_m values, binding lengths, and GC content of stoppers, but obviously had to consider the interaction of various parameters specific for every stopper site. Stalling the assembly at RNA sites 3' of the OAs indicated a site-specific effect on hybridization possibility, whereas the efficiency of 5' stopping most likely depended on the assembly rate, *i.e.*, the speed and forces achieved during the cooperative addition of pre-formed CP disks (Schneider et al. 2016). That means, that hybridization and stalling is strongly site- and region-specific (regarding the local sequence context and its relative position up- or downstream the OAs) concomitant with an extreme temperature-dependency. Even a presumed increase of sterical hindrance and disruption of further CP disk attachment by 5' stoppers with a 5' toehold was not confirmed.

In contrast to other DNA-based technologies, for instance PCR, *in situ* or microarrays hybridization assays, the temperature of hybridizing stoppers to RNA cannot be enhanced to completely denature secondary and tertiary structures in the RNA as well as the DNA oligomer. As a lower assembly yield was found after a partial denaturation step at 65 °C preceding hybridization of stopper S3'$_1$ to RNA (in comparison to a more efficient assembly after treatment at 30 °C), this indicated incorrect backfolding, *i.e.*, the generation of assembly-incompetent RNA folding states. Unfavorable secondary structures might be heat-induced and likely include intragenomic long-range RNA-RNA base paring as it is known for positive-sense RNA viruses that build such long-range interactions to modulate viral processes (for a review see Nicholson and White 2014). A lower assembly rate by using lower assembly temperatures decreased the overall yield of assembly products, but it was shown that more RNA molecules stayed intact to be integrated into the assembly process and finally enhanced the yield using milder denaturation/hybridization conditions before and during stopper binding. These results point at important roles of the RNA secondary structure during the *in vitro* self-assembly and may bring forward a deeper understanding.

Two aims require a compromise: the first one is to bind the DNA stably but reversibly to a defined site at the RNA, thus also the RNA has to lose secondary and tertiary structures, whereas the second goal is that the following refolding of RNA during the partial encapsidation with CP results in a sufficient yield. On the one hand, unfolding the RNA to enable binding of stoppers required increased temperature, on the other hand the enhanced temperature induced other folding intermediates that were likely complex and stable so that backfolding into assembly competent states was not possible. Furthermore, some RNA sites were stably folded in secondary and/or tertiary structures so that even heating could not unravel those folding states, which hindered binding of various stoppers.

To prevent heat-induced degradation of nucleic acids during denaturation and hybridization, another problem to consider, the T_m might be decreased by the reduction of divalent ions and by the addition of denaturing solvents (*e.g.*, urea, formamide) (Wetmur 1976). However, the latter would require a purification to an assembly-compatible solution prior encapsidation with CP, and potentially such agents may even compromise the assembly competence of the TMV components irreversibly. In a previously published study metastable structures were facilitated by a short so-called trigger RNA to refold into the thermodynamic stable structure, providing this desired structure for use as a sensor for micro RNAs (Kobori et al. 2019).

Implementation of such supporting DNA or RNA strands could avoid misfolding of the large RNA into kinetically trapped structures during the backfolding process after hybridization of stoppers,

and thus enhances correctly folded, assembly-competent RNA to increase assembly efficiency of the desired nanotubes.

Simulation-based view of RNA accessibility

Rules established for PCR primer design as well as for strand displacement reaction were not sufficient for the prediction of suitable stopper target positions due to various reasons as discussed above. Hence, this study suggests a combination of computer-based and experimental methods to predict the accessibility of a target sequence at the RNA to efficiently block the self-assembly for the generation of multiple domains. The results of software-based folding using `mfold` and `RNAfold` suggested that RNA sequences with > 6 nt distributed to bulges, internal loops, hairpin loops and/or junctions were accessible for stopper binding and experimentally resulted in high blocking efficiencies, but the distribution of three to four continuous accessible nucleotide stretches was essential. As bulges and loops are often involved in long-range interactions (Nicholson and White 2014), temperature-induced new long-range interactions could also decrease accessibility. A study on toehold-length in strand displacement reactions by Zhang and Winfree (2009) revealed that the rate constant rapidly increased with increasing length for a typical toehold comprised of a mixture of all four bases. This supported the assumption that the RNA-RNA intramolecular folded structure can be resolved by a stopper in dependence on the number of continuous accessible nucleotides in the target sequence even if the RNA-RNA interaction is stronger than the RNA-DNA hybridization (Sugimoto et al. 1995; Searle and Williams 1993).

However, all software-based RNA foldings were limited to ionic conditions of 1 M Na^+, without considering divalent cations in contrast to experimental investigations. As a brief reminder, the experimental data compared to the software-based findings were performed as follows: stoppers were hybridized to RNA in 75 mM SPP (pH 7.2) supplemented with 1.5 mM $MgCl_2$ by an initial partially denaturation step for 5 min at 65 °C with a subsequent temperature gradient (0.1 °C s^{-1}) to 30 °C. Mg^{2+} ions, that were present in the hybridization procedure, stabilize folded intermediate states (Tinoco and Bustamante 1999). The negative charge of RNA molecules perturbs its folding into complex structure, whereas the addition of positive divalent ions (like Mg^{2+}) facilitates the folding, as those reduce the repulsion between the phosphates of RNA. In this study, various concentrations of $MgCl_2$ were applied to the assembly reaction and the assembly yields were compared. The predicted T_m of stoppers was increased by 5 °C to 8 °C in Mg^{2+} ranges from 0 mM to 3 mM (Sugimoto et al. 1995). However, a previous UV absorbance study revealed the transition temperatures of a pseudoknot into hairpin formation as well as the hairpin into single-stranded structure

(Gonzalez and Tinoco 1999; Tinoco and Bustamante 1999). Without the addition of Mg^{2+} ions, the first transition of the pseudoknot was found at 27 °C, in contrast the second transition from hairpin into single-stranded form required 63 °C. The addition of 50 µM Mg^{2+} shifted the transition to higher temperature. The pseudoknot melted at 68 °C, but the hairpin was stabilized by divalent ions and its melting temperature increased up to 90 °C. Thus, contradictory results of the comparative study "experiments *versus* simulation" were obtained, since `mfold` as well as `RNAfold` discount the addition of 1.5 mM $MgCl_2$ that was present in solution. The formed hairpins and/or pseudoknots were likely still stable at 30 °C or even at 65 °C. Furthermore, it verifies that the calculation of T_m only in respect of the stopper sequence is not sufficient, since it does not reflect the temperature to unfold a large RNA sequence with complex secondary and tertiary structure at the respective position.

A well-studied region of TMV-RNA with respect to its secondary structure is the 3' UTR. As this motif is known to form complex structures, five pseudoknots (nt 6211-6395), including the tRNA-like structure (van Belkum et al. 1985; Rietveld et al. 1984), it may be, that the partial denaturation at 65 °C for 5 min under the salt conditions used did not unlock the complex secondary structure of this RNA region and that only a few hybridized nucleotides of the individual stoppers ($S3'_{t1\text{-}t3}$) did not block the assembly sufficiently. The known predicted pseudoknot formation of TLS was correlated with the simulated RNA sequence of the $S3'_{t1\text{-}3}$ binding sites (***Fig. 5-1***). However, the structure predicted by `mfold` was found to be similar to the literature data and the pseudoknot formations did not bind additional nucleotides. This in turn supports the assumption that the stabilizing effect of Mg^{2+} ions was much stronger than expected by calculation of the T_M.

To adapt the software-based prediction to the experimental procedure, both software used in this study, `RNAfold` and `mfold`, offer the possibility to include experimental results as hard- or soft constraints, however, the integration of empirical data into the prediction requires careful handling, since it is not warranted that the resulting structures are accurate (Fallmann et al. 2017).

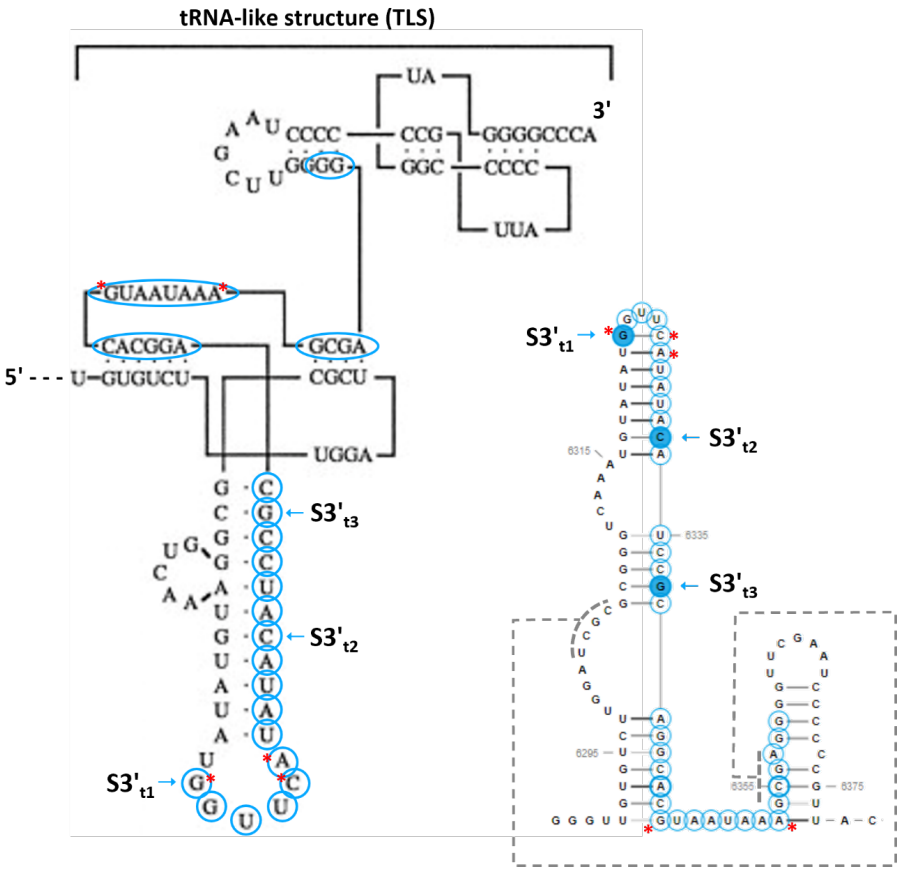

Figure 5-1 Secondary structure representation of the tRNA-like structure (left) (modified according to the Creative Commons Attribution 4.0 International Public License from Tanguay and Gallie 1996) versus the simulated secondary structure including the RNA sequences complementary to S3'$_{t1-3}$ (right). The blue outlined nt highlight the individual sequences complementary to the stoppers. The red asterisks (*) depict nt of interest that are different in the two structures. The greyish dotted line indicates pseudoknot binding, which results from the left structure.

Less manual evaluation of the simulated secondary structures would also facilitate more effective screening of the structure. One option would be the `IntaRNA` software (Richter 2012; Mann et al. 2017; Miladi et al. 2019), which calculates the accessibility of the RNA for hybridization of another RNA strand. Initial comparative experiments with `IntaRNA` revealed no trend of the 3' stoppers used with respect to the calculated energies for hybridization or for unfolding target or query. However, since the toehold was also considered in the calculations with `IntaRNA`, differences of some stoppers due to the toehold sequence in the interaction with RNA were revealed here. Another

advantage of IntaRNA is the prediction of the seed region of the interaction. However, this also did not provide any additional insights for the present study. To complete the calculations, the difference in binding of DNA to RNA would need to be contrasted with RNA-RNA attraction.

Consequently, the performed software-based calculations are a first approach to complement the previously used stopper design rules but are limited in validity. Further analysis of experimental results as well as further empirical data are required, to apply hard- or soft constraint to simulation. On the other hand, to reliably predict accessible stopper binding sites, a temperature-selectable secondary as well as tertiary structure folding tool for longer sequences including pseudoknot calculation might be helpful. In addition, an extended study on the application of $MgCl_2$ during the hybridization reaction could be carried out to bring reaction temperatures to an optimum with the amount of Mg^{2+} ions used. This in turn could allow more accurate prediction of RNA accessibility through software-based methods.
Another advantage of a preceding software-based folding studies in combination with the knowledge gained in this thesis is that long RNAs can be screened for potential additional stopper binding sites depending on the experimental conditions used to avoid further unwanted hybridizations like that of $S3'_1$ to nt 1551-1573.

Visualization, functionalization, and application-related investigations of DTLPs

A first proof-of-concept experiment visualized the generation of 2-DTLPs and confirmed the possibility to site-selectively functionalize one domain. For this purpose, avidin was bound to the biotinylated CP subdomain. A bifunctional NHS-PEG_{12}-biotin linker as well as a maleimide-PEG_{11}-biotin linker were applied to covalently couple to TMV_{Lys} and TMV_{Cys}, respectively, with conjugation efficiencies of 100 % and 50 % with the TMV particle preparations applied in this study. Depending on the application of such DTLPs, the biotinylation efficiency of 50 % of the as-produced nanotubes may be sufficient, *e.g.*, for binding large molecules like streptavidin-conjugated enzymes as it was recently used for biosensors (Koch et al. 2015; Bäcker et al. 2017; Koch et al. 2018). However, the use of smaller molecules (*e.g.*, avidin) to reliably visualize the subdomain *via* transmission electron or atomic force microscopy requires higher occupancy rates as it was found in this study for $CP_{Lys\text{-}Bio}$. Here, avidin (≈ 66 kDa, 5.6 x 5.0 x 4.0 nm (Pugliese et al. 1993)) could uniformly cover the subunit and enhanced its size to reliably measure its width and length.

Further investigations have provided the possibility to fabricate TLPs with three distinct, precise CP domains for the first time. Two routes were established and the as-produced 3-DTLPs were used in two different more application-related studies.

Cys-wt-Lys$_{Bio}$-TLPs (261-30-9) were used to prepare a two-enzyme cascade by site-selective binding of glucose oxidase (GOx) and horseradish peroxidase (HRP) for the detection of glucose in a colorimetric assay as it was intensely investigated immobilized to full-length TMV$_{Cys}$ (Koch et al. 2015; Bäcker et al. 2017). The maleimide linker-attached GOx ([mal]-GOx) addressed CP$_{Cys}$, whereas a streptavidin-conjugate of HRP ([s]-HRP) targeted the biotin moieties of the smallest CP$_{Lys\text{-}Bio}$ domain. The enzyme activity assay verified the integrity of the coupled enzyme on the nanocarrier surface as well as indirect proof was obtained of the production of two differently functionalized domains isolated from one another by a third segment. The determined turnover rates of the two-enzyme cascade built on 3-DTLP carriers were low compared to the values from the extensively investigated initial study (Koch et al. 2015). However, in the earlier study, an excess of carrier rods was incubated in the microtiter plate to immobilize them. Only after that, the enzymes were bound to the immobilized adapters. Due to the differences in immobilization of the nanocarriers, binding of the enzymes, and production of the TLPs, the data obtained from this thesis were not comparable to those obtained in the previous study (personal communication with C. Koch). Further investigation into the advantages of arranging enzymes brought into spatial proximity by the nanoscaffold and what sizes of domains are ideally suited must follow. In addition, a more ideal spatial arrangement of the viral nanocarrier, *e.g.*, by hybridization using nucleic acids covalently bound to solid surfaces or gold nanoparticles (Mueller et al. 2011; Eber et al. 2013), must now be carried out to further increase the efficiency of the enzyme cascade.

The AFM measurements of the 3-DTLPs presented in this thesis demonstrate the possibility to decorate multiple domains specifically with biomolecules and study them *in situ*. Thus, these results provide a good basis for further investigations of oligo- or multiple-DTLPs for the use in AFM-SECM approaches. In the recently submitted article 2-DTLP (Cys-Cys$_{Bio}$-DTLPs (261-39 nm)) immobilized on an ultra-flat silicon oxide surface generated a nanotubular scaffold to assemble a redox-enzymatic system, comprising the quinoprotein glucose dehydrogenase (PQQ-GDH) enzyme and its ferrocene (Fc)-PEG redox mediator (Paiva et al. 2022). The enzymatic activity was visualized by AFM-SECM measurements. The CP$_{Cys\text{-}Bio}$ domain allowed these to be decorated with only a few enzyme molecules (< 10), so that the highest spatial resolution of enzyme molecules studied by electrochemical microscopy to date could be achieved. While in this study the redox mediator was bound to the enzyme via antibodies, the Fc-PEG molecules could be bound to another domain in the next step to investigate the scaffolding effect of DTLPs (Conrado et al. 2008). Finally, this already suggests that oligo-DTLPs not only enable the binding of diverse enzyme variants, but also the coupling of ligands and co-factors into specific domains.

The dynamic DNA-controlled stop-and-go technique offers a high degree of flexibility to guide various segments of differently addressable CP domains. However, to reliably define the length of those segments, a better prediction method was required. The modulation of the folding formation of RNA sections gave an insight but it will never illustrate the behavior of the full sequence. Thus, other options for simulation of long sequences including pseudoknot formations to predict suitable binding sites require deeper evaluation.

The production of DTLPs with two, three or multiple domains delivers many options to use the predefined domains for functionalization with various biomolecules to use them for example in sensor applications. Moreover, the as-prepared TMV-like nanotubes with two or three domains are more defined in their position as well as in the length of the differentially addressable CP segments than previously published studies (Eiben et al. 2014; Eiben 2018; Fukuda et al. 1980; Geiger et al. 2013; Brown et al. 2021). Thus, the presented stop-and-go method provides a suitable basis to prepare single particles with oligo- or multiple CP domains, finely adapted to the desired bionanotechnological application.

6 Bibliography

Abbou, Jeremy; Anne, Agnès; Demaille, Christophe (2004): Probing the structure and dynamics of end-grafted flexible polymer chain layers by combined atomic force-electrochemical microscopy. Cyclic voltammetry within nanometer-thick macromolecular poly(ethylene glycol) layers. In *Journal of the American Chemical Society* 126 (32), pp. 10095–10108. DOI: 10.1021/ja0493502.

Alafeef, Maha; Dighe, Ketan; Moitra, Parikshit; Pan, Dipanjan (2020): Rapid, Ultrasensitive, and Quantitative Detection of SARS-CoV-2 Using Antisense Oligonucleotides Directed Electrochemical Biosensor Chip. In *ACS Nano*. DOI: 10.1021/acsnano.0c06392.

Allawi, Hatim T.; SantaLucia, John (1997): Thermodynamics and NMR of Internal G·T Mismatches in DNA. In *Biochemistry* 36 (34), pp. 10581–10594. DOI: 10.1021/bi962590c.

Alonso, Jose M.; Górzny, Marcin L.; Bittner, Alexander M. (2013): The physics of tobacco mosaic virus and virus-based devices in biotechnology. In *Trends in Biotechnology* 31 (9), pp. 530–538. DOI: 10.1016/j.tibtech.2013.05.013.

Amani, Hamed; Mostafavi, Ebrahim; Arzaghi, Hamidreza; Davaran, Soodabeh; Akbarzadeh, Abolfazl; Akhavan, Omid et al. (2019): Three-Dimensional Graphene Foams: Synthesis, Properties, Biocompatibility, Biodegradability, and Applications in Tissue Engineering. In *ACS biomaterials science & engineering* 5 (1), pp. 193–214. DOI: 10.1021/acsbiomaterials.8b00658.

Anne, Agnès; Chovin, Arnaud; Demaille, Christophe; Michon, Thierry (2018): Redox-Immunofunctionalized Potyvirus Nanoparticles for High-Resolution Imaging by AFM-SECM Correlative Microscopy. In Christina Wege, George P. Lomonossoff (Eds.): Virus-derived nanoparticles for advanced technologies. Methods and protocols. New York: Humana Press (Springer protocols, 1776), pp. 455–470.

Atanasova, Petia; Rothenstein, Dirk; Schneider, Jörg J.; Hoffmann, Rudolf C.; Dilfer, Stefan; Eiben, Sabine et al. (2011): Virus-templated synthesis of ZnO nanostructures and formation of field-effect transistors. In *Advanced Materials* 23 (42), pp. 4918–4922. DOI: 10.1002/adma.201102900.

Bäcker, Matthias; Koch, Claudia; Eiben, Sabine; Geiger, Fania C.; Eber, Fabian J.; Gliemann, Hartmut et al. (2017): Tobacco mosaic virus as enzyme nanocarrier for electrochemical biosensors. In *Sensors and Actuators B: Chemical* 238, pp. 716–722. DOI: 10.1016/j.snb.2016.07.096.

Bancroft, John B.; Hiebert, Ernest (1967): Formation of an infectious nucleoprotein from protein and nucleic acid isolated from a small spherical virus. In *Virology* 32 (2), pp. 354–356. DOI: 10.1016/0042-6822(67)90284-X.

Baranowska-Wójcik, Ewa; Szwajgier, Dominik; Oleszczuk, Patryk; Winiarska-Mieczan, Anna (2020): Effects of Titanium Dioxide Nanoparticles Exposure on Human Health-a Review. In *Biological trace element research* 193 (1), pp. 118–129. DOI: 10.1007/s12011-019-01706-6.

Bath, Jonathan; Turberfield, Andrew J. (2007): DNA nanomachines. In *Nature Nanotechnology* 2, pp. 275–284. DOI: 10.1038/nnano.2007.104.

Beren, Christian; Dreesens, Lisa L.; Liu, Katherine N.; Knobler, Charles M.; Gelbart, William M. (2017): The Effect of RNA Secondary Structure on the Self-Assembly of Viral Capsids. In *Biophysical Journal* 113 (2), pp. 339–347. DOI: 10.1016/j.bpj.2017.06.038.

Besong-Ndika, Jane; Wahlsten, Matti; Cardinale, Daniela; Pille, Jan; Walter, Jocelyne; Michon, Thierry; Mäkinen, Kristiina (2016): Toward the Reconstitution of a Two-Enzyme Cascade for Resveratrol Synthesis on Potyvirus Particles. In *Frontiers in Plant Science* 7, p. 89. DOI: 10.3389/fpls.2016.00089.

Braun, Erez; Eichen, Yoav; Sivan, Uri; Ben-Yoseph, Gdalyahu (1998): DNA-templated assembly and electrode attachment of a conducting silver wire. In *Nature* 391 (6669), pp. 775–778. DOI: 10.1038/35826.

Brown, Adam D.; Chu, Sangwook; Kappagantu, Madhu; Ghodssi, Reza; Culver, James N. (2021): Reprogramming Virus Coat Protein Carboxylate Interactions for the Patterned Assembly of Hierarchical Nanorods. In *Biomacromolecules* 22 (6), pp. 2515–2523. DOI: 10.1021/acs.biomac.1c00258.

Bruckman, Michael A.; Randolph, Lauren N.; VanMeter, Allen; Hern, Stephen; Shoffstall, Andrew J.; Taurog, Rebecca E.; Steinmetz, Nicole F. (2014): Biodistribution, pharmacokinetics, and blood compatibility of native and PEGylated tobacco mosaic virus nano-rods and -spheres in mice. In *Virology* 449, pp. 163–173. DOI: 10.1016/j.virol.2013.10.035.

Butler, P. Jonathan G. (1972): Structures and roles of the polymorphic forms of tobacco mosaic virus protein: VI. Assembly of the nucleoprotein rods of tobacco mosaic virus from the protein disks and RNA. In *Journal of Molecular Biology* 72 (1), pp. 25–35. DOI: 10.1016/0022-2836(72)90065-4.

Butler, P. Jonathan G. (1999): Self-Assembly of Tobacco Mosaic Virus. The Role of an Intermediate Aggregate in Generating Both Specificity and Speed. In *Philosophical Transactions: Biological Sciences* 354, pp. 537–550. DOI: 10.1098/rstb.1999.0405.

Butler, P. Jonathan G.; Durham, Anthony C. H.; Klug, Aaron (1972): Structures and roles of the polymorphic forms of tobacco mosaic virus protein: IV. Control of mode of aggregation of tobacco mosaic virus protein by proton binding. In *Journal of Molecular Biology* 72 (1), pp. 1–18. DOI: 10.1016/0022-2836(72)90063-0.

Butler, P. Jonathan G.; Finch, John T.; Zimmern, David (1977): Configuration of tobacco mosaic virus RNA during virus assembly. In *Nature* 265 (5591), pp. 217–219. DOI: 10.1038/265217a0.

Butler, P. Jonathan G.; Lomonossoff, George P. (1980): RNA-protein interactions in the assembly of tobacco mosaic virus. In *Biophysical Journal* 32 (1), pp. 295–312. DOI: 10.1016/S0006-3495(80)84958-7.

Caldwell, W. Brett; Chen, Kaimin; Mirkin, Chad A.; Babinec, Susan J. (1993): Self-assembled monolayer films of fullerene C60 on cysteamine-modified gold. In *Langmuir* 9 (8), pp. 1945–1947. DOI: 10.1021/la00032a002.

Cardinale, Daniela; Carette, Noelle; Michon, Thierry (2012): Virus scaffolds as enzyme nano-carriers. In *Trends in Biotechnology* 30 (7), pp. 369–376. DOI: 10.1016/j.tibtech.2012.04.001.

Champness, John N.; Bloomer, Anne C.; Bricogne, Gérard; Butler, P. Jonathan G.; Klug, Aaron (1976): The structure of the protein disk of tobacco mosaic virus to 5A resolution. In *Nature* 259 (5538), pp. 20–24. DOI: 10.1038/259020a0.

Chandrasekaran, Arun Richard (2016): Programmable DNA scaffolds for spatially-ordered protein assembly. In *Nanoscale* 8 (8), pp. 4436–4446. DOI: 10.1039/c5nr08685j.

Chapman, Sean N. (1998): Tobamovirus isolation and RNA extraction. In *Methods in molecular biology (Clifton, N.J.)* 81, pp. 123–129. DOI: 10.1385/0-89603-385-6:123.

Chen, Junghui H.; Seeman, Nadrian C. (1991): Synthesis from DNA of a molecule with the connectivity of a cube. In *Nature* 350 (6319), pp. 631–633. DOI: 10.1038/350631a0.

Chiang, Chia-Ying; Epstein, Jillian; Brown, Adam D.; Munday, Jeremy N.; Culver, James N.; Ehrman, Sheryl (2012): Biological templates for antireflective current collectors for photoelectrochemical cell applications. In *Nano Letters* 12 (11), pp. 6005–6011. DOI: 10.1021/nl303579z.

Chu, Sangwook; Brown, Adam D.; Culver, James N.; Ghodssi, Reza (2018): Tobacco Mosaic Virus as a Versatile Platform for Molecular Assembly and Device Fabrication. In *Biotechnology Journal* 13 (12), e1800147. DOI: 10.1002/biot.201800147.

Chu, Sangwook; Gerasopoulos, Konstantinos; Ghodssi, Reza (2016): Tobacco mosaic virus-templated hierarchical Ni/NiO with high electrochemical charge storage performances. In *Electrochimica Acta* 220, pp. 184–192. DOI: 10.1016/j.electacta.2016.10.106.

Chujo, Tetsuya; Ishibashi, Kazuhiro; Miyashita, Shuhei; Ishikawa, Masayuki (2015): Functions of the 5'- and 3'-untranslated regions of tobamovirus RNA. In *Virus Research*. DOI: 10.1016/j.virusres.2015.01.028.

Conrado, Robert J.; Varner, Jeffrey D.; DeLisa, Matthew P. (2008): Engineering the spatial organization of metabolic enzymes: mimicking nature's synergy. In *Current Opinion in Biotechnology* 19 (5), pp. 492–499. DOI: 10.1016/j.copbio.2008.07.006.

Cooper, Bret (2014): Proof by synthesis of tobacco mosaic virus. In *Genome Biology* 15 (5), R67. DOI: 10.1186/gb-2014-15-5-r67.

Dieffenbach, Carl W.; Lowe, Todd M.; Dveksler, Gabriela S. (1993): General concepts for PCR primer design. In *PCR methods and applications* 3 (3), S30-7. DOI: 10.1101/gr.3.3.s30.

Donis-Keller, Helen (1979): Site specific enzymatic cleavage of RNA. In *Nucleic Acids Research* 7 (1), pp. 179–192. DOI: 10.1093/nar/7.1.179.

Drexler, K. Eric (1981): Molecular engineering: An approach to the development of general capabilities for molecular manipulation. In *Proceedings of the National Academy of Sciences* 78 (9), pp. 5275–5278. DOI: 10.1073/pnas.78.9.5275.

Drexler, K. Eric (2004): Nanotechnology: From Feynman to Funding. In *Bulletin of Science, Technology & Society* 24 (1), pp. 21–27. DOI: 10.1177/0270467604263113.

Durham, Anthony C. H.; Finch, John T.; Klug, Aaron (1971): States of aggregation of tobacco mosaic protein. In *Nature New Biology* 229, pp. 37–42. DOI: 10.1038/newbio229037a0.

Durham, Anthony C. H.; Klug, Aaron (1971): Polymerization of Tobacco Mosaic Virus Protein and its Control. In *Nature New Biology* 229 (2), pp. 42–46. DOI: 10.1038/newbio229042a0.

Eber, Fabian J. (2012): RNA-directed formation of nanostructures. Self-assembly of novel nucleoprotein architectures using plant viral building blocks. Dissertation. Universität Stuttgart, Stuttgart. Biologisches Institut.

Eber, Fabian J.; Eiben, Sabine; Jeske, Holger; Wege, Christina (2013): Bottom-up-assembled nanostar colloids of gold cores and tubes derived from tobacco mosaic virus. In *Angewandte Chemie* 52 (28), pp. 7203–7207. DOI: 10.1002/anie.201300834.

Eber, Fabian J.; Eiben, Sabine; Jeske, Holger; Wege, Christina (2015): RNA-controlled assembly of tobacco mosaic virus-derived complex structures. from nanoboomerangs to tetrapods. In *Nanoscale* 7 (1), pp. 344–355. DOI: 10.1039/c4nr05434b.

Eiben, Sabine (2018): RNA-Directed Assembly of Tobacco Mosaic Virus (TMV)-Like Carriers with Tunable Fractions of Differently Addressable Coat Proteins. In Christina Wege, George P. Lomonossoff (Eds.): Virus-derived nanoparticles for advanced technologies. Methods and protocols. New York: Humana Press (Springer protocols, 1776), pp. 35–50. Available online at https://doi.org/10.1007/978-1-4939-7808-3_3.

Eiben, Sabine; Stitz, Nina; Eber, Fabian J.; Wagner, Jerrit; Atanasova, Petia; Bill, Joachim et al. (2014): Tailoring the surface properties of tobacco mosaic virions by the integration of bacterially expressed mutant coat protein. In *Virus Research* 180, pp. 92–96. DOI: 10.1016/j.virusres.2013.11.019.

Fairall, Louise; Finch, John T.; Hui, Cho-Fat; Cantor, Charles R.; Butler, P. Jonathan G. (1986): Studies of tobacco mosaic virus reassembly with an RNA tail blocked by a hybridised and cross-linked probe. In *European Journal of Biochemistry* 156 (3), pp. 459–465. DOI: 10.1111/j.1432-1033.1986.tb09604.x.

Fallmann, Jörg; Will, Sebastian; Engelhardt, Jan; Grüning, Björn; Backofen, Rolf; Stadler, Peter F. (2017): Recent advances in RNA folding. In *Journal of biotechnology* 261, pp. 97–104. DOI: 10.1016/j.jbiotec.2017.07.007.

Feynman, Richard (1960): There's Plenty of Room at the Bottom. An Invitation to Enter a New Field of Physics. In *Engineering and Science* 23 (5), pp. 22–36.

Fraenkel-Conrat, Heinz (1957): Degradation of tobacco mosaic virus with acetic acid. In *Virology* 4 (1), pp. 1–4. DOI: 10.1016/0042-6822(57)90038-7.

Fraenkel-Conrat, Heinz (1986): Tobacco Mosaic Virus The History of Tobacco Mosaic Virus and the Evolution of Molecular Biology. In Marc H. V. van Regenmortel, Heinz Fraenkel-Conrat (Eds.): The Plant Viruses. Boston, MA: Springer US, pp. 5–17.

Fraenkel-Conrat, Heinz; Williams, Robley C. (1955): Reconstitution of active tobacco mosaic virus from its inactive protein and nucleic acid components. In *Proceedings of the National Academy of Sciences* 41 (10), pp. 690–698. DOI: 10.1073/pnas.41.10.690.

Fromm, Simon A.; Bharat, Tanmay A. M.; Jakobi, Arjen J.; Hagen, Wim J. H.; Sachse, Carsten (2015): Seeing tobacco mosaic virus through direct electron detectors. In *Journal of structural biology* 189 (2), pp. 87–97. DOI: 10.1016/j.jsb.2014.12.002.

Fukuda, Megumi; Ohno, Takeshi; Okada, Yoshimi; Otsuki, Yoshiaki; Takebe, Itaru (1978): Kinetics of biphasic reconstitution of tobacco mosaic virus in vitro. In *Proceedings of the National Academy of Sciences* 75 (4), pp. 1727–1730. DOI: 10.1073/pnas.75.4.1727.

Fukuda, Megumi; Okada, Yoshimi; Otsuki, Yoshiaki; Takebe, Itaru (1980): The site of initiation of rod assembly on the RNA of a tomato and a cowpea strain of tobacco mosaic virus. In *Virology* 101 (2), pp. 493–502. DOI: 10.1016/0042-6822(80)90463-8.

Gaddipati, Jaya P.; Siegel, Albert (1990): Study of TMV assembly with heterologous RNA containing the origin-of-assembly sequence. In *Virology* 174 (2), pp. 337–344. DOI: 10.1016/0042-6822(90)90087-8.

Gallie, Daniel R.; Plaskitt, Kitty A.; Wilson, Tim Michael A. (1987): The effect of multiple dispersed copies of the origin-of-assembly sequence from TMV RNA on the morphology of pseudovirus particles assembled in vitro. In *Virology* 158 (2), pp. 473–476. DOI: 10.1016/0042-6822(87)90225-X.

Garmann, Rees F.; Comas-Garcia, Mauricio; Gopal, Ajaykumar; Knobler, Charles M.; Gelbart, William M. (2014): The assembly pathway of an icosahedral single-stranded RNA virus depends on the

strength of inter-subunit attractions. In *Journal of Molecular Biology* 426 (5), pp. 1050–1060. DOI: 10.1016/j.jmb.2013.10.017.

Geiger, Fania C.; Eber, Fabian J.; Eiben, Sabine; Mueller, Anna; Jeske, Holger; Spatz, Joachim P.; Wege, Christina (2013): TMV nanorods with programmed longitudinal domains of differently addressable coat proteins. In *Nanoscale* 5 (9), pp. 3808–3816. DOI: 10.1039/c3nr33724c.

Goelet, Philip; Lomonossoff, George P.; Butler, P. Jonathan G.; Akam, Michael E.; Gait, Michael J.; Karn, Jonathan (1982): Nucleotide sequence of tobacco mosaic virus RNA. In *Proceedings of the National Academy of Sciences* 79 (19), pp. 5818–5822. DOI: 10.1073/pnas.79.19.5818.

Gonzalez, Ruben L.; Tinoco, Ignacio (1999): Solution structure and thermodynamics of a divalent metal ion binding site in an RNA pseudoknot. In *Journal of Molecular Biology* 289 (5), pp. 1267–1282. DOI: 10.1006/jmbi.1999.2841.

Gooding, Guy V., Jr.; Hebert, Teddy T. (1967): A simple technique for purification of tobacco mosaic virus in large quantities. In *Phytopathology* 57 (11), p. 1285.

Goodman, Russel P.; Schaap, Iwan A. T.; Tardin, Catherine F.; Erben, Christoph M.; Berry, Richard M.; Schmidt, Christoph F.; Turberfield, Andrew J. (2005): Rapid chiral assembly of rigid DNA building blocks for molecular nanofabrication. In *Science* 310 (5754), pp. 1661–1665. DOI: 10.1126/science.1120367.

Green, Michael R.; Sambrook, Joseph (2012): Molecular cloning. A laboratory manual. 4 ed. Cold Spring Harbor, N.Y.: Cold Spring Harbor Laboratory Press.

Gruber, Andreas R.; Lorenz, Ronny; Bernhart, Stephan H.; Neuböck, Richard; Hofacker, Ivo L. (2008): The Vienna RNA websuite. In *Nucleic Acids Research* 36 (Web Server issue), W70-4. DOI: 10.1093/nar/gkn188.

Gu, Hongzhou; Chao, Jie; Xiao, Shou-Jun; Seeman, Nadrian C. (2009): Dynamic patterning programmed by DNA tiles captured on a DNA origami substrate. In *Nature Nanotechnology* 4 (4), pp. 245–248. DOI: 10.1038/nnano.2009.5.

Gu, Hongzhou; Chao, Jie; Xiao, Shou-Jun; Seeman, Nadrian C. (2010): A proximity-based programmable DNA nanoscale assembly line. In *Nature* 465 (7295), pp. 202–205. DOI: 10.1038/nature09026.

Guilley, Hubert; Jonard, Gérard; Hirth, Léon (1975): Sequence of 71 nucleotides at the 3'-end of tobacco mosaic virus RNA. In *Proceedings of the National Academy of Sciences* 72 (3), pp. 864–868. DOI: 10.1073/pnas.72.3.864.

Guilley, Hubert; Jonard, Gérard; Kukla, B.; Richards, Kenneth E. (1979): Sequence of 1000 nucleotides at the 3′ end of tobacco mosaic virus RNA. In *Nucleic Acids Research* 6 (4), pp. 1287–1308. DOI: 10.1093/nar/6.4.1287.

Guo, Peixuan (2010): The emerging field of RNA nanotechnology. In *Nature Nanotechnology* 5 (12), pp. 833–842. DOI: 10.1038/nnano.2010.231.

Hanewich-Hollatz, Mikhail H.; Chen, Zhewei; Hochrein, Lisa M.; Huang, Jining; Pierce, Niles A. (2019): Conditional Guide RNAs: Programmable Conditional Regulation of CRISPR/Cas Function in Bacterial and Mammalian Cells via Dynamic RNA Nanotechnology. In *ACS central science* 5 (7), pp. 1241–1249. DOI: 10.1021/acscentsci.9b00340.

Hegner, Martin; Wagner, Peter; Semenza, Giorgio (1993): Ultralarge atomically flat template-stripped Au surfaces for scanning probe microscopy. In *Surface Science* 291 (1-2), pp. 39–46. DOI: 10.1016/0039-6028(93)91474-4.

Hess, Henry; Bachand, George D.; Vogel, Viola (2004): Powering nanodevices with biomolecular motors. In *Chemistry (Weinheim an der Bergstrasse, Germany)* 10 (9), pp. 2110–2116. DOI: 10.1002/chem.200305712.

Hill, Diana F.; Petersen, George B. (1982): Nucleotide sequence of bacteriophage f1 DNA. In *Journal of Virology* 44 (1), p. 32. DOI: 10.1128/JVI.44.1.32-46.1982.

Hogue, Richard; Asselin, Alain (1984): Study of Tobacco Mosaic-Virus Invitro Disassembly by Sucrose Density Gradient Centrifugation and Agarose-Gel Electrophoresis. In *Canadian Journal of Botany-Revue Canadienne De Botanique* 62 (3), pp. 457–462. DOI: 10.1139/b84-069.

Hou, Xucheng; Zaks, Tal; Langer, Robert; Dong, Yizhou (2021): Lipid nanoparticles for mRNA delivery. In *Nature reviews. Materials*, pp. 1–17. DOI: 10.1038/s41578-021-00358-0.

Ishikawa, Masayuki; Meshi, Tetsuo; Motoyoshi, Fusao; Takamalsu, Nobuhiko; Okada, Yoshimi (1986): In vitro mutagenesis of the putative replicase genes of tobacco mosaic virus. In *Nucleic Acids Research* 14 (21), pp. 8291–8305. DOI: 10.1093/nar/14.21.8291.

Jeng, Shih-Tong; Gardner, Jeffrey F.; Gumport, Richard I. (1992): Transcription termination in vitro by bacteriophage T7 RNA polymerase. The role of sequence elements within and surrounding a rho-independent transcription terminator. In *The Journal of biological chemistry* 267 (27), pp. 19306–19312. DOI: 10.1016/S0021-9258(18)41775-9.

Jeyachandran, Yekkoni L.; Mielczarski, Ela; Rai, Beena; Mielczarski, Jerzy A. (2009): Quantitative and qualitative evaluation of adsorption/desorption of bovine serum albumin on hydrophilic and hydrophobic surfaces. In *Langmuir* 25 (19), pp. 11614–11620. DOI: 10.1021/la901453a.

Jeyachandran, Yekkoni L.; Mielczarski, Jerzy A.; Mielczarski, Ela; Rai, Beena (2010): Efficiency of blocking of non-specific interaction of different proteins by BSA adsorbed on hydrophobic and hydrophilic surfaces. In *Journal of colloid and interface science* 341 (1), pp. 136–142. DOI: 10.1016/j.jcis.2009.09.007.

Johnson, Philip Z.; Kasprzak, Wojciech K.; Shapiro, Bruce A.; Simon, Anne E. (2019): RNA2Drawer: geometrically strict drawing of nucleic acid structures with graphical structure editing and highlighting of complementary subsequences. In *RNA biology*, pp. 1–5. DOI: 10.1080/15476286.2019.1659081.

Jonard, Gérard; Richards, Kenneth E.; Guilley, Hubert; Hirth, Léon (1977): Sequence from the assembly nucleation region of TMV RNA. In *Cell* 11 (3), pp. 483–493. DOI: 10.1016/0092-8674(77)90066-6.

Kadri, Anan; Maiss, Edgar; Amsharov, Nadja; Bittner, Alexander M.; Balci, Sinan; Kern, Klaus et al. (2011): Engineered Tobacco mosaic virus mutants with distinct physical characteristics in planta and enhanced metallization properties. In *Virus Research* 157 (1), pp. 35–46. DOI: 10.1016/j.virusres.2011.01.014.

Kibbe, Warren A. (2007): OligoCalc. an online oligonucleotide properties calculator. In *Nucleic Acids Research* 35 (Web Server issue), W43-6. DOI: 10.1093/nar/gkm234.

Knez, Martin; Sumser, Martin P.; Bittner, Alexander M.; Wege, Christina; Jeske, Holger; Hoffmann, Dominik M. P. et al. (2004): Binding the Tobacco Mosaic Virus to Inorganic Surfaces. Langmuir. In *Langmuir* 20 (2), pp. 441–447. DOI: 10.1021/la035425o.

Kobori, Shungo; Nomura, Yoko; Yokobayashi, Yohei (2019): Self-powered RNA nanomachine driven by metastable structure. In *Nucleic Acids Research* 47 (11), pp. 6007–6014. DOI: 10.1093/nar/gkz364.

Koch, Claudia; Eber, Fabian J.; Azucena, Carlos; Förste, Alexander; Walheim, Stefan; Schimmel, Thomas et al. (2016): Novel roles for well-known players. From tobacco mosaic virus pests to enzymatically active assemblies. In *Beilstein journal of nanotechnology* 7, pp. 613–629. DOI: 10.3762/bjnano.7.54.

Koch, Claudia; Poghossian, Arshak; Schöning, Michael J.; Wege, Christina (2018): Penicillin Detection by Tobacco Mosaic Virus-Assisted Colorimetric Biosensors. In *Nanotheranostics* 2 (2), pp. 184–196. DOI: 10.7150/ntno.22114.

Koch, Claudia; Wabbel, Katrin; Eber, Fabian J.; Krolla-Sidenstein, Peter; Azucena, Carlos; Gliemann, Hartmut et al. (2015): Modified TMV Particles as Beneficial Scaffolds to Present Sensor Enzymes. In *Frontiers in Plant Science* 6, p. 1137. DOI: 10.3389/fpls.2015.01137.

Kroto, Harold W.; Heath, James R.; O'Brien, Sean C.; Curl, Robert F.; Smalley, Richard E. (1985): C60: Buckminsterfullerene. In *Nature* 318 (6042), pp. 162–163. DOI: 10.1038/318162a0.

Küchler, Andreas; Yoshimoto, Makoto; Luginbühl, Sandra; Mavelli, Fabio; Walde, Peter (2016): Enzymatic reactions in confined environments. In *Nature Nanotechnology* 11 (5), pp. 409–420. DOI: 10.1038/nnano.2016.54.

Laemmli, Ulrich K. (1970): Cleavage of structural proteins during the assembly of the head of bacteriophage T4. In *Nature* 227 (5259), pp. 680–685. DOI: 10.1038/227680a0.

Lam, Patricia; Gulati, Neetu M.; Stewart, Phoebe L.; Keri, Ruth A.; Steinmetz, Nicole F. (2016): Bioengineering of Tobacco Mosaic Virus to Create a Non-Infectious Positive Control for Ebola Diagnostic Assays. In *Scientific Reports* 6, p. 23803. DOI: 10.1038/srep23803.

Lebeurier, Geneviève; Nicolaieff, Anatole; Richards, Kenneth E. (1977): Inside-out model for self-assembly of tobacco mosaic virus. In *Proceedings of the National Academy of Sciences* 74 (1), pp. 149–153. DOI: 10.1073/pnas.74.1.149.

Lee, Young-Chul; Moon, Ju-Young (2020a): Fundamental of Biological Systems and Bionanotechnology. In Young-Chul Lee, Ju-Young Moon (Eds.): Introduction to bionanotechnology. Singapore: Springer Nature Singapore; Imprint Springer (Springer eBook Collection), pp. 15–31.

Lee, Young-Chul; Moon, Ju-Young (2020b): Introduction to Nanotechnology and Bionanotechnology. In Young-Chul Lee, Ju-Young Moon (Eds.): Introduction to bionanotechnology. Singapore: Springer Nature Singapore; Imprint Springer (Springer eBook Collection), pp. 1–14.

Liu, Jinny L.; Zabetakis, Daniel; Breger, Joyce C.; Anderson, George P.; Goldman, Ellen R. (2020): Multi-Enzyme Assembly on T4 Phage Scaffold. In *Frontiers in bioengineering and biotechnology* 8, p. 571. DOI: 10.3389/fbioe.2020.00571.

Lorenz, Ronny; Bernhart, Stephan H.; Höner zu Siederdissen, Christian; Tafer, Hakim; Flamm, Christoph; Stadler, Peter F.; Hofacker, Ivo L. (2011): ViennaRNA Package 2.0. In *Algorithms for Molecular Biology* 6 (1), p. 26. DOI: 10.1186/1748-7188-6-26.

Love, Andrew J.; Makarov, Valentine V.; Sinitsyna, Olga V.; Shaw, Jane; Yaminsky, Igor V.; Kalinina, Natalia O.; Taliansky, Michael E. (2015): A Genetically Modified Tobacco Mosaic Virus that can Produce Gold Nanoparticles from a Metal Salt Precursor. In *Frontiers in Plant Science* 6, p. 984. DOI: 10.3389/fpls.2015.00984.

Lucate, Joshua G.; Szuchmacher Blum, Amy (2017): The Importance of Calcium Ions in Poly-A RNA Mediated Tobacco Mosaic Virus-Like Rod Formation. In *Journal of nanoscience and nanotechnology* 17 (1), pp. 224–230. DOI: 10.1166/jnn.2017.13710.

Lustig, Alice; Levine, Arnold J. (1992): One hundred years of virology. In *Journal of Virology* 66 (8), pp. 4629–4631. DOI: 10.1128/jvi.66.8.4629-4631.1992.

Maharaj, Payal D.; Mallajosyula, Jyothi K.; Lee, Gloria; Thi, Phillip; Zhou, Yiyang; Kearney, Christopher M.; McCormick, Alison A. (2014): Nanoparticle encapsidation of Flock house virus by auto assembly of Tobacco mosaic virus coat protein. In *International Journal of Molecular Science* 15 (10), pp. 18540–18556. DOI: 10.3390/ijms151018540.

Mammen, Mathai; Choi, Seok-Ki; Whitesides, George M. (1998): Polyvalent Interactions in Biological Systems: Implications for Design and Use of Multivalent Ligands and Inhibitors. In *Angewandte*

Chemie 37 (20), pp. 2754–2794. DOI: 10.1002/(SICI)1521-3773(19981102)37:20<2754::AID-ANIE2754>3.0.CO;2-3.

Mann, Martin; Wright, Patrick R.; Backofen, Rolf (2017): IntaRNA 2.0: enhanced and customizable prediction of RNA-RNA interactions. In *Nucleic Acids Research* 45 (W1), W435-W439. DOI: 10.1093/nar/gkx279.

Mao, Chengde; Sun, Weiqiong; Shen, Zhiyong; Seeman, Nadrian C. (1999): A nanomechanical device based on the B-Z transition of DNA. In *Nature* 397 (6715), pp. 144–146. DOI: 10.1038/16437.

Markham, Nicholas R.; Zuker, Michael (2005): DINAMelt web server for nucleic acid melting prediction. In *Nucleic Acids Research* 33 (Web Server issue), W577-81. DOI: 10.1093/nar/gki591.

Medintz, Igor L.; Clapp, Aaron R.; Mattoussi, Hedi; Goldman, Ellen R.; Fisher, Brent; Mauro, J. Matthew (2003): Self-assembled nanoscale biosensors based on quantum dot FRET donors. In *Nature materials* 2 (9), pp. 630–638. DOI: 10.1038/nmat961.

Miladi, Milad; Montaseri, Soheila; Backofen, Rolf; Raden, Martin (2019): Integration of accessibility data from structure probing into RNA-RNA interaction prediction. In *Bioinformatics* 35 (16), pp. 2862–2864. DOI: 10.1093/bioinformatics/bty1029.

Mirkin, Chad A.; Letsinger, Robert L.; Mucic, Robert C.; Storhoff, James J. (1996): A DNA-based method for rationally assembling nanoparticles into macroscopic materials. In *Nature* 382 (6592), pp. 607–609. DOI: 10.1038/382607a0.

Mirkin, Chad A.; Ratner, Mark A. (1992): Molecular Electronics. In *Annual Review of Physical Chemistry* 43 (1), pp. 719–754. DOI: 10.1146/annurev.pc.43.100192.003443.

Mueller, Anna; Eber, Fabian J.; Azucena, Carlos; Petershans, Andre; Bittner, Alexander M.; Gliemann, Hartmut et al. (2011): Inducible site-selective bottom-up assembly of virus-derived nanotube arrays on RNA-equipped wafers. In *ACS Nano* 5 (6), pp. 4512–4520. DOI: 10.1021/nn103557s.

Mueller, Anna; Kadri, Anan; Jeske, Holger; Wege, Christina (2010): In vitro assembly of Tobacco mosaic virus coat protein variants derived from fission yeast expression clones or plants. In *Journal of Virological Methods* 166 (1-2), pp. 77–85. DOI: 10.1016/j.jviromet.2010.02.026.

Müller, Joachim; Niemeyer, Christof M. (2008): DNA-directed assembly of artificial multienzyme complexes. In *Biochemical and biophysical research communications* 377 (1), pp. 62–67. DOI: 10.1016/j.bbrc.2008.09.078.

Nakamura, Haruki; Oda, Yasushi; Iwai, Shigenori; Inoue, Hideo; Ohtsuka, Eiko; Kanaya, Shigenori et al. (1991): How does RNase H recognize a DNA.RNA hybrid? In *Proceedings of the National Academy of Sciences* 88 (24), pp. 11535–11539. DOI: 10.1073/pnas.88.24.11535.

Namba, Keiichi; Pattanayek, Rekha; Stubbs, Gerald (1989): Visualization of protein-nucleic acid interactions in a virus. In *Journal of Molecular Biology* 208 (2), pp. 307–325. DOI: 10.1016/0022-2836(89)90391-4.

Nault, Laurent; Taofifenua, Cecilia; Anne, Agnès; Chovin, Arnaud; Demaille, Christophe; Besong-Ndika, Jane et al. (2015): Electrochemical atomic force microscopy imaging of redox-immunomarked proteins on native potyviruses: from subparticle to single-protein resolution. In *ACS Nano* 9 (5), pp. 4911–4924. DOI: 10.1021/acsnano.5b00952.

Nicholson, Beth L.; White, K. Andrew (2014): Functional long-range RNA-RNA interactions in positive-strand RNA viruses. In *Nature Reviews Microbiology* 12 (7), pp. 493–504. DOI: 10.1038/nrmicro3288.

Oguro, Akihiro; Ohtsu, Takashi; Nakamura, Yoshikazu (2009): An aptamer-based biosensor for mammalian initiation factor eukaryotic initiation factor 4A. In *Analytical biochemistry* 388 (1), pp. 102–107. DOI: 10.1016/j.ab.2009.01.046.

Oster, Gerald. (1951): The isoelectric points of some strains of tobacco mosaic virus. In *The Journal of biological chemistry* 190 (1), pp. 55–59. DOI: 10.1016/s0021-9258(18)56044-0.

Owczarzy, Richard; Moreira, Bernardo G.; You, Yong; Behlke, Mark A.; Walder, Joseph A. (2008): Predicting stability of DNA duplexes in solutions containing magnesium and monovalent cations. In *Biochemistry* 47 (19), pp. 5336–5353. DOI: 10.1021/bi702363u.

Owczarzy, Richard; You, Yong; Moreira, Bernardo G.; Manthey, Jeffrey A.; Huang, Lingyan; Behlke, Mark A.; Walder, Joseph A. (2004): Effects of sodium ions on DNA duplex oligomers. improved predictions of melting temperatures. In *Biochemistry* 43 (12), pp. 3537–3554. DOI: 10.1021/bi034621r.

Paiva, Telmo O.; Schneider, Angela; Bataille, Laure; Chovin, Arnaud; Anne, Agnès; Michon, Thierry et al. (2022): Enzymatic activity of individual bioelectrocatalytic viral nanoparticles: dependence of catalysis on the viral scaffold and its length. In *Nanoscale* 14 (3), pp. 875–889. DOI: 10.1039/d1nr07445h.

Palukaitis, Peter; Zaitlin, Milton (1986): Tobacco Mosaic Virus Infectivity and Replication. In Marc H. V. van Regenmortel, Heinz Fraenkel-Conrat (Eds.): The Plant Viruses. Boston, MA: Springer US, pp. 105–131.

Papazoglou, Elisabeth S.; Parthasarathy, Aravind (2007): BioNanotechnology. In *Synthesis Lectures on Biomedical Engineering* 2 (1), pp. 1–139. DOI: 10.2200/S00051ED1V01Y200610BME007.

Patel, Anisha N.; Anne, Agnès; Chovin, Arnaud; Demaille, Christophe; Grelet, Eric; Michon, Thierry; Taofifenua, Cecilia (2017): Scaffolding of Enzymes on Virus Nanoarrays: Effects of Confinement and Virus Organization on Biocatalysis. In *Small (Weinheim an der Bergstrasse, Germany)*. DOI: 10.1002/smll.201603163.

Patzel, Volker; Steidl, Ulrich; Kronenwett, Ralf; Haas, Rainer; Sczakiel, Georg (1999): A theoretical approach to select effective antisense oligodeoxyribonucleotides at high statistical probability. In *Nucleic Acids Research* 27 (22), pp. 4328–4334. DOI: 10.1093/nar/27.22.4328.

Piner, Richard D.; Zhu, Jin; Xu, Feng; Hong, Seunghun; Mirkin, Chad A. (1999): "Dip-Pen" nanolithography. In *Science* 283 (5402), pp. 661–663. DOI: 10.1126/science.283.5402.661.

Pugliese, Luisa; Coda, Alessandro; Malcovati, Massimo; Bolognesi, Martino (1993): Three-dimensional structure of the tetragonal crystal form of egg-white avidin in its functional complex with biotin at 2.7 A resolution. In *Journal of Molecular Biology* 231 (3), pp. 698–710. DOI: 10.1006/jmbi.1993.1321.

Rasband, Wayne S. (1997-2011): ImageJ. Bethesda, Maryland, USA: US National Institutes of Health.

Ravetch, Jeffrey V.; Horiuchi, Kensuke; Zinder, Norton D. (1977): Nucleotide sequences near the origin of replication of bacteriophage f1. In *Proceedings of the National Academy of Sciences* 74 (10), pp. 4219–4222. DOI: 10.1073/pnas.74.10.4219.

Richter, Andreas S. (2012): Computational analysis and prediction of RNA-RNA interactions. Available online at http://www.bioinf.uni-freiburg.de/publications/richter-phdthesis-2012.pdf.

Rietveld, Krijn; Linschooten, Kees; Pleij, Cornelis W. A.; Bosch, Leendert (1984): The three-dimensional folding of the tRNA-like structure of tobacco mosaic virus RNA. A new building principle applied twice. In *The EMBO Journal* 3 (11), pp. 2613–2619. DOI: 10.1002/j.1460-2075.1984.tb02182.x.

Rosi, Nathaniel L.; Mirkin, Chad A. (2005): Nanostructures in biodiagnostics. In *Chemical Reviews* 105 (4), pp. 1547–1562. DOI: 10.1021/cr030067f.

Rothemund, Paul W. K. (2006): Folding DNA to create nanoscale shapes and patterns. In *Nature* 440 (7082), pp. 297–302. DOI: 10.1038/nature04586.

Royston, Elizabeth; Ghosh, Ayan; Kofinas, Peter; Harris, Michael T.; Culver, James N. (2008): Self-assembly of virus-structured high surface area nanomaterials and their application as battery electrodes. In *Langmuir* 24 (3), pp. 906–912. DOI: 10.1021/la7016424.

Scherr, Michaela; Rossi, John J.; Sczakiel, Georg; Patzel, Volker (2000): RNA accessibility prediction: a theoretical approach is consistent with experimental studies in cell extracts. In *Nucleic Acids Research* 28 (13), pp. 2455–2461. DOI: 10.1093/nar/28.13.2455.

Schneider, Angela N.; Eber, Fabian J.; Wenz, Nana L.; Altintoprak, Klara; Jeske, Holger; Eiben, Sabine; Wege, Christina (2016): Dynamic DNA-controlled "stop-and-go" assembly of well-defined protein domains on RNA-scaffolded TMV-like nanotubes. In *Nanoscale* 8 (47), pp. 19853–19866. DOI: 10.1039/C6NR03897B.

Schön, Astrid; Mundry, Karl W. (1984): Coordinated two-disk nucleation, growth and properties, of virus-like particles assembled from tobacco-mosaic-virus capsid protein with poly(A) or oligo(A) of different length. In *European Journal of Biochemistry* 140 (1), pp. 119–127. DOI: 10.1111/j.1432-1033.1984.tb08074.x.

Searle, Mark S.; Williams, Dudley H. (1993): On the stability of nucleic acid structures in solution: enthalpy-entropy compensations, internal rotations and reversibility. In *Nucleic Acids Research* 21 (9), pp. 2051–2056. DOI: 10.1093/nar/21.9.2051.

Seeman, Nadrian C. (2005): From genes to machines: DNA nanomechanical devices. In *Trends in biochemical sciences* 30 (3), pp. 119–125. DOI: 10.1016/j.tibs.2005.01.007.

Seeman, Nadrian C. (2010): Nanomaterials based on DNA. In *Annual review of biochemistry* 79, pp. 65–87. DOI: 10.1146/annurev-biochem-060308-102244.

Sherman, William B.; Seeman, Nadrian C. (2004): A Precisely Controlled DNA Biped Walking Device. In *Nano Letters* 4 (7), pp. 1203–1207. DOI: 10.1021/nl049527q.

Sit, Tim L.; Vaewhongs, Andrew A.; Lommel, Steven A. (1998): RNA-mediated trans-activation of transcription from a viral RNA. In *Science* 281 (5378), pp. 829–832. DOI: 10.1126/science.281.5378.829.

Sleat, David E.; Turner, Philip C.; Finch, John T.; Butler, P. Jonathan G.; Wilson, Tim Michael A. (1986): Packaging of Recombinant RNA Molecules into Pseudovirus Particles Directed by the Origin-of-Assembly Sequence from Tobacco Mosaic Virus RNA. In *Virology* 155, pp. 299–308. DOI: 10.1016/0042-6822(86)90194-7.

Smith, Mark L.; Corbo, Tina A.; Bernales, Jacqueline; Lindbo, John A.; Pogue, Gregory P.; Palmer, Kenneth E.; McCormick, Alison A. (2007): Assembly of trans-encapsidated recombinant viral vectors engineered from Tobacco mosaic virus and Semliki Forest virus and their evaluation as immunogens. In *Virology* 358 (2), pp. 321–333. DOI: 10.1016/j.virol.2006.08.040.

Steinmetz, Nicole F.; Lim, Sierin; Sainsbury, Frank (2020): Protein cages and virus-like particles: from fundamental insight to biomimetic therapeutics. In *Biomaterials science* 8 (10), pp. 2771–2777. DOI: 10.1039/d0bm00159g.

Stockley, Peter G.; Rolfsson, Ottar; Thompson, Gary S.; Basnak, Gabriella; Francese, Simona; Stonehouse, Nicola J. et al. (2007): A simple, RNA-mediated allosteric switch controls the pathway to formation of a T=3 viral capsid. In *Journal of Molecular Biology* 369 (2), pp. 541–552. DOI: 10.1016/j.jmb.2007.03.020.

Storhoff, James J.; Mucic, Robert C.; Mirkin, Chad A. (1997): Strategies for Organizing Nanoparticles into Aggregate Structures and Functional Materials. In *Journal of Cluster Science* 8 (2), pp. 179–216. DOI: 10.1023/A:1022632007869.

Su, Shi; Kang, Peter M. (2020): Recent Advances in Nanocarrier-Assisted Therapeutics Delivery Systems. In *Pharmaceutics* 12 (9). DOI: 10.3390/pharmaceutics12090837.

Sugimoto, Naoki; Nakano, Shu-ichi; Katoh, Misa; Matsumura, Akiko; Nakamuta, Hiroyuki; Ohmichi, Tatsuo et al. (1995): Thermodynamic parameters to predict stability of RNA/DNA hybrid duplexes. In *Biochemistry* 34 (35), pp. 11211–11216. DOI: 10.1021/bi00035a029.

Sugio, Shigetoshi; Kashima, Akiko; Mochizuki, Shinichi; Noda, Mariko; Kobayashi, Kumiko (1999): Crystal structure of human serum albumin at 2.5 A resolution. In *Protein engineering* 12 (6), pp. 439–446. DOI: 10.1093/Protein/12.6.439.

Tanguay, Robert L.; Gallie, Daniel R. (1996): Isolation and characterization of the 102-kilodalton RNA-binding protein that binds to the 5' and 3' translational enhancers of tobacco mosaic virus RNA. In *The Journal of biological chemistry* 271 (24), pp. 14316–14322. DOI: 10.1074/jbc.271.24.14316.

Temsamani, amal.; Kubert, Michael; Agrawal, Sudhir (1995): Sequence identity of the n-1 product of a synthetic oligonucleotide. In *Nucleic Acids Research* 23 (11), pp. 1841–1844. DOI: 10.1093/nar/23.11.1841.

Tenchov, Rumiana; Bird, Robert; Curtze, Allison E.; Zhou, Qiongqiong (2021): Lipid Nanoparticles-From Liposomes to mRNA Vaccine Delivery, a Landscape of Research Diversity and Advancement. In *ACS Nano*. DOI: 10.1021/acsnano.1c04996.

Tinoco, Ignacio; Bustamante, Carlos (1999): How RNA folds. In *Journal of Molecular Biology* 293 (2), pp. 271–281. DOI: 10.1006/jmbi.1999.3001.

Tomizawa, Jun-Ichi; Ohmori, Haruo; Bird, Robert E. (1977): Origin of replication of colicin E1 plasmid DNA. In *Proceedings of the National Academy of Sciences* 74 (5), pp. 1865–1869. DOI: 10.1073/pnas.74.5.1865.

Tseng, Ricky J.; Tsai, Chunglin; Ma, Liping P.; Ouyang, Jianyong; Ozkan, Cengiz S.; Yang, Yang (2006): Digital memory device based on tobacco mosaic virus conjugated with nanoparticles. In *Nature Nanotechnology* 1 (1), pp. 72–77. DOI: 10.1038/nnano.2006.55.

Turner, D. Richard; Butler, P. Jonathan G. (1986): Essential Features of the Assembly Origin of Tobacco Mosaic-Virus Rna as Studied by Directed Mutagenesis. In *Nucleic Acids Research* 14 (23), pp. 9229–9242. DOI: 10.1093/nar/14.23.9229.

Turner, D. Richard; McGuigan, C. J.; Butler, P. Jonathan G. (1989): Assembly of hybrid RNAs with tobacco mosaic virus coat protein. Evidence for incorporation of disks in 5'-elongation along the major RNA tail. In *Journal of Molecular Biology* 209 (3), pp. 407–422. DOI: 10.1016/0022-2836(89)90006-5.

van Belkum, Alex; Abrahams, Jan P.; Pleij, Cornelis W. A.; Bosch, Leendert (1985): Five pseudoknots are present at the 204 nucleotides long 3' noncoding region of tobacco mosaic virus RNA. In *Nucleic Acids Research* 13 (21), pp. 7673–7686. DOI: 10.1093/nar/13.21.7673.

van den Heuvel, Martin G. L.; Dekker, Cees (2007): Motor proteins at work for nanotechnology. In *Science* 317 (5836), pp. 333–336. DOI: 10.1126/science.1139570.

Wadu-Mesthrige, Kapila; Pati, Biswajit; McClain, W. Martin; Liu, Gang-Yu (1996): Disaggregation of Tobacco Mosaic Virus by Bovine Serum Albumin. In *Langmuir* 12 (14), pp. 3511–3515. DOI: 10.1021/la9508506.

Walter, Amy E.; Turner, Douglas H.; Kim, James; Lyttle, Matthew H.; Müller, Peter; Mathews, David H.; Zuker, Michael (1994): Coaxial stacking of helixes enhances binding of oligoribonucleotides and improves predictions of RNA folding. In *Proceedings of the National Academy of Sciences* 91 (20), pp. 9218–9222. DOI: 10.1073/pnas.91.20.9218.

Wang, Pengfei; Ko, Seung Hyeon; Tian, Cheng; Hao, Chenhui; Mao, Chengde (2013): RNA-DNA hybrid origami: folding of a long RNA single strand into complex nanostructures using short DNA helper strands. In *Chemical Communications* 49 (48), pp. 5462–5464. DOI: 10.1039/C3CC41707G.

Wei, Qixin; He, Sicong; Qu, Jianan; Xia, Jiang (2020): Synthetic Multienzyme Complexes Assembled on Virus-like Particles for Cascade Biosynthesis In Cellulo. In *Bioconjugate chemistry* 31 (10), pp. 2413–2420. DOI: 10.1021/acs.bioconjchem.0c00476.

Wenz, Nana L. (2018): Nucleinsäure-kontrollierte Integration von Tabakmosaikvirus-Derivaten in verzweigte Hybrid-Nanostrukturen: Nucleic acid-controlled integration of tobacco mosaic virus derivatives into branched hybrid nanostructures: Universität Stuttgart. Available online at https://books.google.de/books?id=QHk9zQEACAAJ.

Wenz, Nana L.; Piasecka, Sylwia; Kalinowski, Matthäus; Schneider, Angela N.; Richert, Clemens; Wege, Christina (2018): Building expanded structures from tetrahedral DNA branching elements, RNA and TMV protein. In *Nanoscale* 10 (14), pp. 6496–6510. DOI: 10.1039/C7NR07743B.

Wetmur, James G. (1976): Hybridization and renaturation kinetics of nucleic acids. In *Annual review of biophysics and bioengineering* 5, pp. 337–361. DOI: 10.1146/annurev.bb.05.060176.002005.

Wu, Na; Wang, Kun; Wang, Yi-Ting; Chen, Ming-Li; Chen, Xu-Wei; Yang, Ting; Wang, Jian-Hua (2020): Three-Dimensional DNA Nanomachine Biosensor by Integrating DNA Walker and Rolling Machine Cascade Amplification for Ultrasensitive Detection of Cancer-Related Gene. In *Analytical chemistry* 92 (16), pp. 11111–11118. DOI: 10.1021/acs.analchem.0c01074.

Wu, Zhenyu; Mueller, Anna; Degenhard, Sven; Ruff, S. Emil; Geiger, Fania C.; Bittner, Alexander M. et al. (2010): Enhancing the magnetoviscosity of ferrofluids by the addition of biological nanotubes. In *ACS Nano* 4 (8), pp. 4531–4538. DOI: 10.1021/nn100645e.

Yao, Dongbao; Bhadra, Sanchita; Xiong, Erhu; Liang, Haojun; Ellington, Andrew D.; Jung, Cheulhee (2020): Dynamic Programming of a DNA Walker Controlled by Protons. In *ACS Nano* 14 (4), pp. 4007–4013. DOI: 10.1021/acsnano.9b08166.

Yurke, Bernard; Mills, Allen P. (2003): Using DNA to Power Nanostructures. In *Genetic Programming and evolvable machines* 4, pp. 111–122. DOI: 10.1023/A:1023928811651.

Yurke, Bernard; Turberfield, Andrew J.; Mills, Allen P.; Simmel, Friedrich C.; Neumann, Jennifer L. (2000): A DNA-fuelled molecular machine made of DNA. In *Nature* 406 (6796), pp. 605–608. DOI: 10.1038/35020524.

Zaitlin, Milton (1998): The Discovery of the Causal Agent of the Tobacco Mosaic Disease. In Shain-Dow Kung, Shang-Fa Yang (Eds.): Discoveries in Plant Biology: WORLD SCIENTIFIC, pp. 105–110.

Zeenko, Vladimir V.; Ryabova, Lyubov A.; Spirin, Alexander S.; Rothnie, Helen M.; Hess, Daniel; Browning, Karen S.; Hohn, Thomas (2002): Eukaryotic elongation factor 1A interacts with the upstream pseudoknot domain in the 3' untranslated region of tobacco mosaic virus RNA. In *Journal of Virology* 76 (11), pp. 5678–5691. DOI: 10.1128/jvi.76.11.5678-5691.2002.

Zhang, David Y.; Seelig, Georg (2011): Dynamic DNA nanotechnology using strand-displacement reactions. In *Nature Chemistry* 3 (2), pp. 103–113. DOI: 10.1038/nchem.957.

Zhang, David Yu; Winfree, Erik (2009): Control of DNA strand displacement kinetics using toehold exchange. In *Journal of the American Chemical Society* 131 (47), pp. 17303–17314. DOI: 10.1021/ja906987s.

Zhang, Rufeng; Zhang, Jie; Qu, Xiaonan; Li, Shasha; Zhao, Yihan; Liu, Su et al. (2020): Efficient strand displacement amplification via stepwise movement of a bipedal DNA walker on an electrode surface for ultrasensitive detection of antibiotics. In *The Analyst* 145 (8), pp. 2975–2981. DOI: 10.1039/d0an00139b.

Zhong, Hong; Seeman, Nadrian C. (2006): RNA used to control a DNA rotary nanomachine. In *Nano Letters* 6 (12), pp. 2899–2903. DOI: 10.1021/nl062183e.

Zimmern, David (1977): The nucleotide sequence at the origin for assembly on tobacco mosaic virus RNA. In *Cell* 11 (3), pp. 463–482. DOI: 10.1016/0092-8674(77)90065-4.

Zimmern, David (1983): An extended secondary structure model for the TMV assembly origin, and its correlation with protection studies and an assembly defective mutant. In *The EMBO Journal* 2 (11), pp. 1901–1907. DOI: 10.1002/j.1460-2075.1983.tb01677.x.

Zimmern, David; Wilson, Tim Michael A. (1976): Location of the origin for viral reassembly on tobacco mosaic virus RNA and its relation to stable fragment. In *FEBS Letters* 71 (2), pp. 294–298. DOI: 10.1016/0014-5793(76)80954-4.

Zuker, Michael (2003): Mfold web server for nucleic acid folding and hybridization prediction. In *Nucleic Acids Research* 31 (13), pp. 3406–3415. DOI: 10.1093/nar/gkg595.

7 Acknowledgement

Ich danke Prof. Christina Wege für die Möglichkeit diese Arbeit im Bereich der Bionanotechnologie rund um TMV anzufertigen und für die Unterstützung diese auch im Anschluss an meine Tätigkeit am Institut fertig zu stellen. Vor allem bedanke ich mich herzlich für die großartige Motivation während meines Endspurts.

Prof. Björn Voß danke ich für die Übernahme des Zweitgutachtens und des kurzfristigen Austauschs über meine RNA-Zugänglichkeitsstudien, die mich durchaus motiviert haben, mit den Ergebnissen diese These noch abzurunden.

Für die experimentelle Unterstützung bedanke ich mich bei der gesamten ehemaligen Abteilung Molekularbiologie und Virologie der Pflanzen, unter der Leitung von Prof. (a.D.) Holger Jeske, dem ich besonders für seinen fachlichen Input rund um die Molekularbiologie, Elektronenmikroskopie und Statistik danke.

Für die Hilfsbereitschaft, den Spaß und die Motivation im Labor und in vielen Feierabend- und Geburtstagsrunden, möchte ich mich bei allen bedanken, die mich in der Zeit begleitet haben. Die täglichen Mittags- und Kaffeerunden, gemeinsames Kochen und der nicht-fachliche Austausch haben so manche nicht funktionieren Versuche schnell vergessen lassen. Der fachliche Austausch in diesen Runden hat aber doch immer wieder neue Ideen geliefert, so dass mein Ideenkatalog noch immer unendlich lang und längst nicht abgearbeitet ist.

Claudia Koch, Kathrin Richter und Nana Wenz: euch danke ich besonders für die Geduld, die ihr in den letzten Jahren doch immer wieder hattet, um euch mit meinem Thema auseinander zu setzen, meine Arbeit zu lesen und wertvolles Feedback, aber vor allem Motivation zu geben. Ich freue mich, dass ihr durch unsere gemeinsame Zeit am Institut gute Freunde geworden seid und mir als diese auch weiterhin zur Seite steht.

Meine Familie und Freunde machen mich zu einem sehr glücklichen Menschen, liefern die Ablenkung, Motivation und Energie, die nötig war, um diese vielen Seiten mit Worten zu füllen. Damit gilt jedem einzelnen von euch mein herzlichster Dank! Von Herzen danke ich besonders meinem Mann für das "Rücken-frei-halten", die bedingungslose Unterstützung, das Aushalten all meiner Launen, den Glaube an seine Nanostrukturwissenschaftlerin und vor allem für seine Liebe…denn zwei sind besser als einer allein…aber was sind dann erst drei?

Ein Kuss ist der Austausch von Bakterienkulturen, allerdings nicht zu Forschungszwecken. - Karl Farkas

Appendix

A1 Additional binding site of S3'$_1$ to wt-RNA

To prove the assumption of an additional binding position, the TMV-RNA sequence was analyzed *via* A Plasmid Editor (ApE, v2.0.61, available at: http://biologylabs.utah.edu/jorgensen/wayned/ape.). Various positions were identified with mismatches varying between eight to nine nucleotides. All sequences were analyzed by DINAMelt with the Two-hybrid model (http://www.unafold.org/Dinamelt/applications/hybridization-of-two-different-strands-of-dna-or-rna.php) (Markham and Zuker 2005). Only position 1551-1573 nt (upstream of the OAs) showed significant hybridization and thus was identified as an additional binding region considering eight mismatches.

	S3'$_1$ *vs.* RNA position **1551-1573**	**S3'$_1$** *vs.* RNA position **5533-5555**
Sequence		
RNA (5' > 3')	GCAUUUCCCUCCGUGAAAGAGAG	CGAUCUCGAACCGGGAAAAAGAG
Stopper (3' > 5')#	~~GC~~TA~~G~~AG~~CTT~~GGC~~C~~CTTT~~T~~TCTC	GCTAGAGCTTGGCCCTTTTTCTC
Important numbers*		
T_M (Conc)	49.2°C	50.9°C
ΔG	5.1 kcal/mol	6.4 kcal/mol
ΔH	34.7 kcal/mol	39.4 kcal/mol
ΔS	109.2 cal/mol/K	122.3 cal/mol/K
T_M (C_p)	48.9 °C	71.2 °C
T_M (Ext1)	47.9 °C	69.6 °C
T_M (Ext2)	46.1 °C	54.3 °C

#greyish, strikethrough nucleotides depict the mismatch in the stopper sequence; *from 0 °C by 1 °C to 100 °C as DNA; [A_0] = 3.5e-06 M, [B_0] = 1.4e-07 M; [Na^+] = 0.075 M, [Mg^{2+}] = 0.0015 M.

If the hybridization temperature is below the calculated $T_m \approx 47$ °C, the statistically probability of binding to this position might be enhanced.

A2 Example of estimating the yield of nucleoprotein tubes from a native gel

The formation of proteins stained are similar for each nucleoprotein tube independent from its length. Quantitation of product per sample was estimated by analyzing the fractions of one lane *via* the software ImageJ. The estimation is exemplarily shown for the mixture of full-length (300 nm) and partially assembled particles (S3'$_2$/RNA, 267 nm). The pixel intensity of Coomassie Brillant Blue staining was calculated in percent (a). Given that the sum of both protein tubes equates to 100 % protein in this sample, it follows the percentaged protein amount/fraction (b). Comparing the measured pixel intensity with the amount of protein per fraction (c), the percentaged amount of product tubes was calculated (d).

Table A-1 Example of estimating the yield of nucleoprotein tubes from gel.

S3'$_2$/RNA	tube length	(a) intensity	(b) protein	(c) intensity/protein	(d) product
	300 nm	72 %	53 %	1.4	70 %
	267 nm	28 %	47 %	0.6	30 %

(a) pixel intensity of Coomassie Brillant Blue staining; (b) percentaged protein amount/fraction; (c) ratio of pixel intensity to amount of protein per fraction; (d) percentaged amount of product tubes

A3 Stop-and-go with S3'$_1$

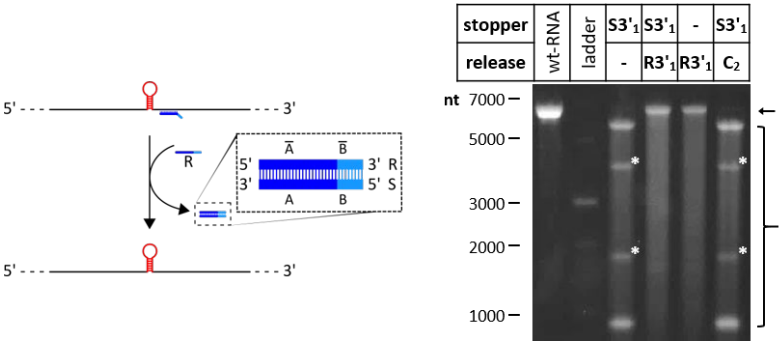

Figure A-1 Reversibility of stopper S3'$_1$ hybridization to the RNA scaffold through its displacement by toehold-release achieved with DNA oligomer R3'$_1$. Adapted from Schneider et al. 2016 according to the Creative Commons Non-Commercial Attribution 3.0 International Public License. **Left:** Scheme of the release process (in the absence of CPs, not to scale). **Right:** Agarose gel electrophoretic separation of the products after RNase H cleavage of DNA/RNA hybridization products of RNA. Fragments were separated on a 1 % agarose gel under denaturing conditions. Arrows denote bands of undigested RNA, brackets the range of fragments expected after RNase H digestion. White asterisks label additional fragments occurring upon RNase H incubation.

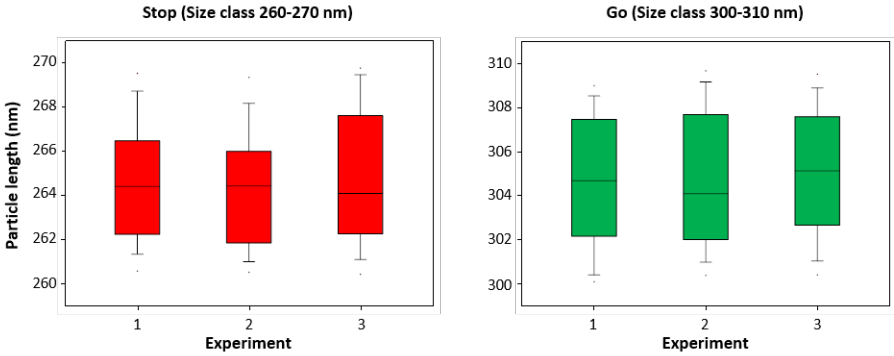

Figure A-2 Comparative statistical analysis of the "stop"- and "go"-classes obtained in three experiments performed with stopper S3'$_1$. The expected "stop"-class of 260-270 nm (left) as well as the "go"-class of 300-310 nm (right) length did not differ significantly between all independent experiments (p = 0.630 and p = 0.752, respectively). Data are presented as boxplots (line: median, box boundaries: 25/75 % quartiles, whiskers: 10/90 % percentiles, dots: 5/95 % percentiles). Reprinted from Schneider et al. 2016 according to the Creative Commons Non-Commercial Attribution 3.0 International Public License.

A4 Stop-and-go using hRNAs as scaffolds

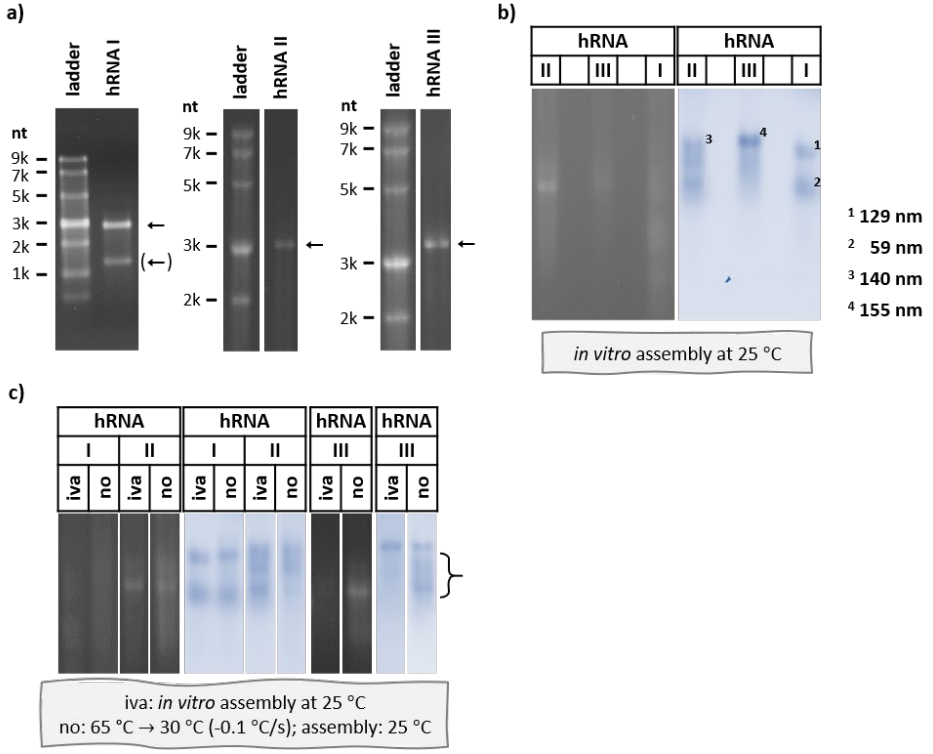

Figure A-3 (a) Electrophoretic analyses of the *in vitro* transcribed heterologous RNA scaffolds I to III (a-c) in 1.5 % denaturing agarose gels (adapted from Schneider et al. 2016 according to the Creative Commons Non-Commercial Attribution 3.0 International Public License). The sizes of the corresponding ladder fractions are depicted at the left side of each gel, whereas the desired product length is illustrated by an arrow. The arrow in the brackets shows the terminated product of hRNA I. (b) Native agarose gel analysis of *in vitro* assembled hRNA scaffolds with predicted nanotube length (c) Native agarose gel analysis of *in vitro* assembled hRNA scaffolds: iva *versus* no stopper. The curly bracket indicates additional by-product of assembly.

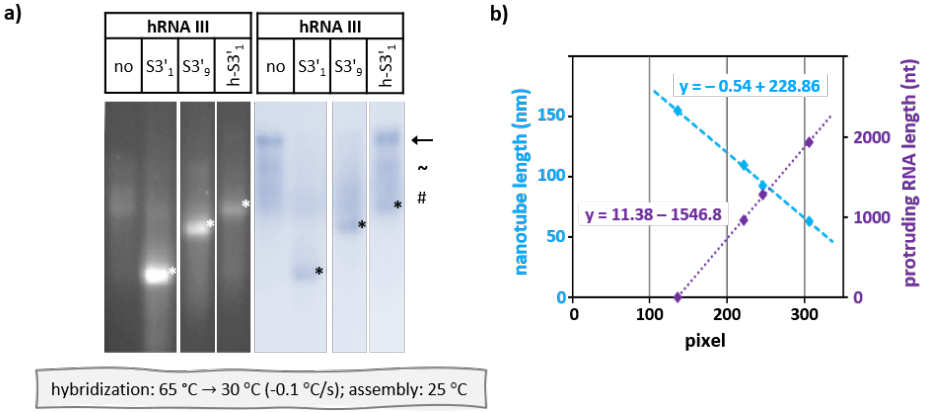

Figure A-4 (a) Visualization of various stop states of hRNA III after nanoparticle separation in a native agarose gel (b) Analysis of densitometrical determination of the native gel (a) to estimate nanotube sizes and protruding RNA lengths of the various assembly states.

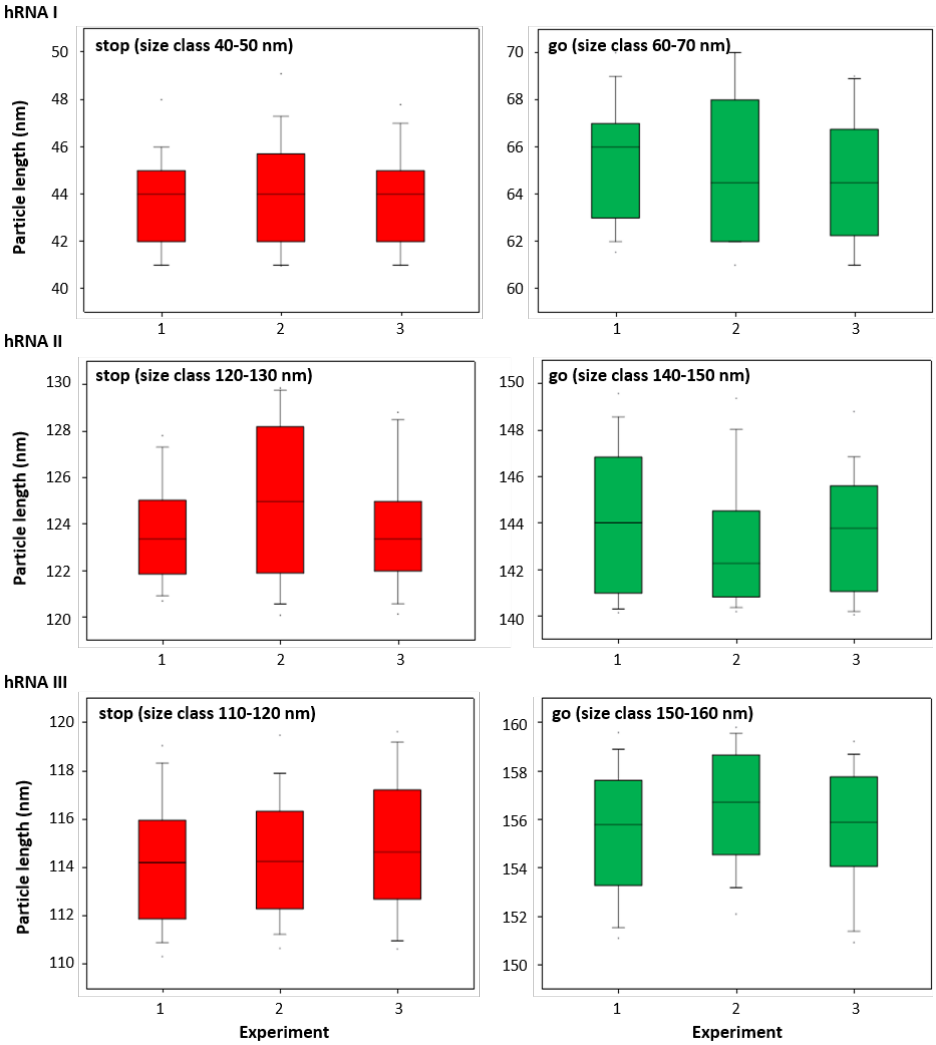

Figure A-5 "Stop-and-go": Statistical analysis of the "stop"- and "go"-classes obtained in three experiments each performed with three different heterologous RNAs. Both the expected "stop"-class (left) and the "go"-class (right) did not differ significantly between the independent experiments for each hRNA. Data are presented as boxplots (line: median, box boundaries: 25/75 % quartiles, whiskers: 10/90 % percentiles, dots: 5/95 % percentiles). Reprinted from Schneider et al. 2016 according to the Creative Commons Non-Commercial Attribution 3.0 International Public License.

A5 Evaluation of temperature conditions using wt-RNA as scaffold

Additionally, previously identified 3' stoppers S3'$_{1,\ 5,\ 9,\ t3}$ that bind under denaturing hybridization conditions and efficiently block the assembly at 25 °C were tested whether they are convenient at milder conditions. To discriminate the effects of milder conditions, in a first approach, the hybridization was performed using 30 °C, 2 h, followed by assembly at 25 °C. S3'$_1$ and S3'$_5$ stalled the assembly to the usual extent. However, not each of these 3' stoppers arrested the encapsidation after hybridization at 30 °C, for 2 h (***Fig. A-6b***). This verified that the complex secondary structure requires almost complete denaturation prior assembly to successful bind the stopper (Guilley et al. 1975; Rietveld et al. 1984).

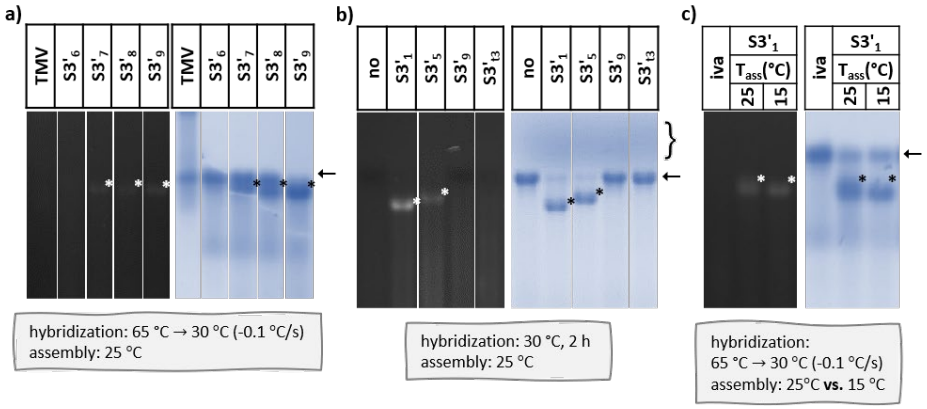

Figure A-6 Visualization of "stop" states after nanoparticle separation on native agarose gels. Hybridization and assembly was performed as stated below the gel images. The arrow indicates fully assembled particles. Black/white asterisks (*) label bands with higher electrophoretic mobility. **(a)** 0.8 % native agarose gel, broken while Coomassie Brilliant Blue staining **(b)** 1 % native agarose gel, the curly bracket highlights non-assembled TMV-CP **(c)** 1 % native agarose gel. Decreased assembly temperature has no effect on the blocking amenability of stopper S3'$_1$. "iva": *in vitro* assembly of wt-RNA with wt-CP.

Table A-2 Overview over frequency of preferred secondary structure and accessible nucleotides.

Stopper name	S3'$_1$	S3'$_5$	S3'$_9$	S3'$_{t3}$
RNAfold (30 °C)				
Number of nucleotides				
*accessible nt**	2-1	1-2-5	1-5-1	2-1
double strand	20	16	16	19
mfold (30 °C)				
Frequency (%) [a]	70	89	96	44
Number of nucleotides				
*accessible nt**	2-2-5	2-5	1-5-1	7-1
double strand	14	17	16	14
Blocking efficiency [b]	100	95	0	0
mfold (65 °C)				
Frequency (%) [a]	90	56	100	100
Number of nucleotides				
*accessible nt**	2-11	1-12	1-5-1	6-1
double strand	10	11	16	15
Blocking efficiency [b]	100	95	100	100

[a] Frequency of the predominant secondary structures resulted from the MFE and suboptimal structures for the sequence intervals; * sum of all types of structural elements accessible for hybridization; [b] equates to the amount of partially assembled products calculated by analyzing nanotube separation in native gels. All amounts were determined at a 25-fold molar excess of stopper over RNA (see in *Appendix A2* for details).

A6 Evaluation of assembly products *via* ultracentrifugation

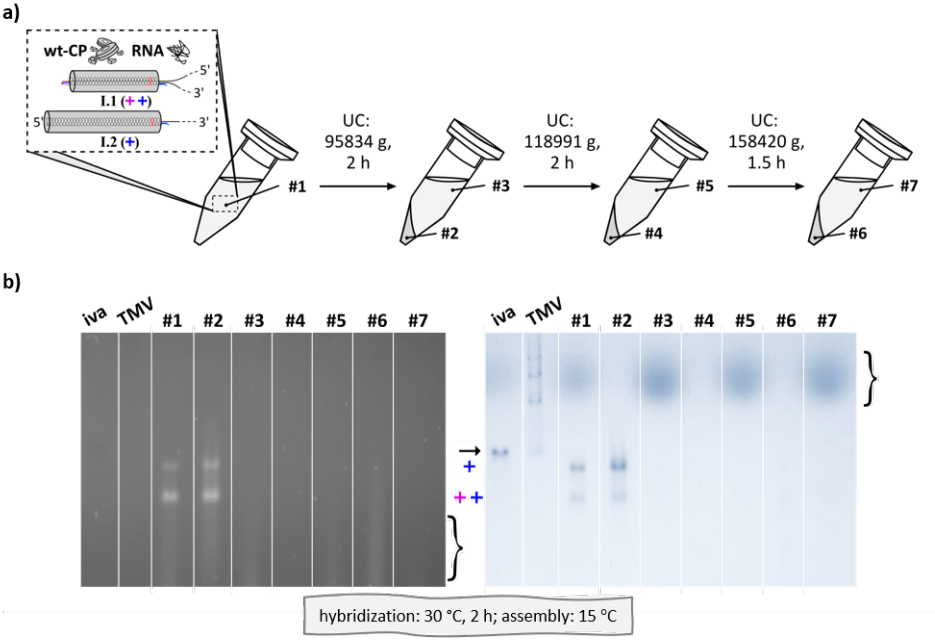

Figure A-7 Influence of different revolution speeds during ultracentrifugation. The sample was prepared as follows: hybridization of both stoppers, S5'$_6$ and S3'$_5$, to RNA was performed at 30 °C for 2 h, followed by assembly with wt-CP ON at 15 °C and subsequent centrifugation. **(a)** The steps of ultracentrifugation and sample numbers (#) are illustrated in the scheme (not to scale). The supernatants (#1, #3, #5) were proceeded for UC. **(b)** The different fractions of DTLPs were analyzed by nanoparticle separation in a native agarose gel. "iva" (*in vitro* assembly of wt-RNA with wt-CP) as well as TMV indicate fully assembled particles (arrow). Blue/purple "plus" (**+**) label bands with higher electrophoretic mobility due to stopped assembly by only S3'$_5$ (**+**), S5'$_6$ (**+**) or both, S5'$_6$ and S3'$_5$ (**++**). The upper bracket marks the residual free CPs, whereas the lower one highlights the non-assembled RNA.

A7 Evaluation of nanotube length from AFM images

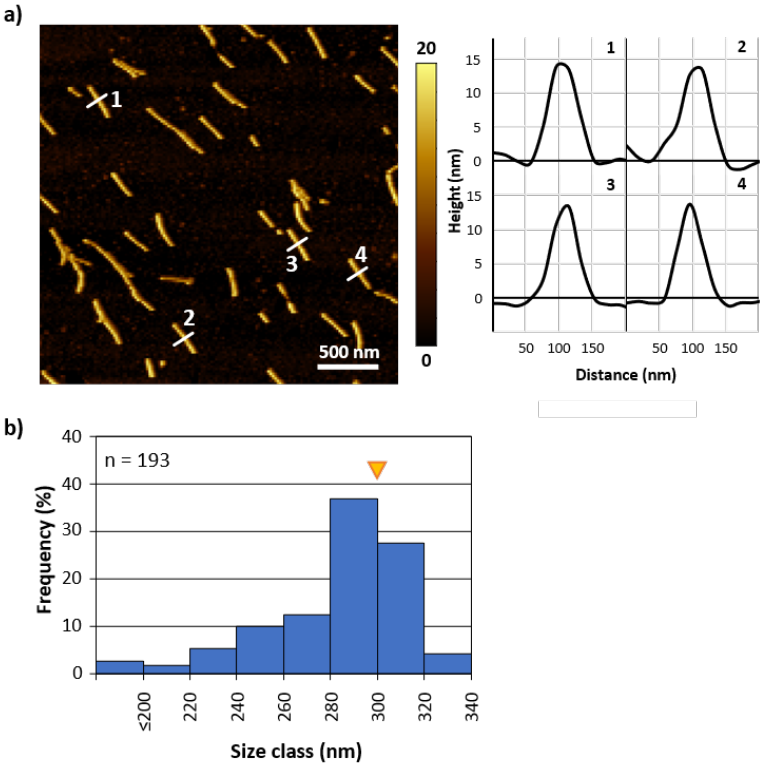

Figure A-8 (a) AFM image and corresponding width measurements of nanotubes adhered to a gold surface. 1 to 4 indicate full-length DTLPs exemplarily analyzed, the white lines represent the positions of corresponding cross sections. **(b)** Analysis of the resulting nanotube length distribution *via* the software ImageJ. n = 193 particles were measured from AFM images discounted tip convolution effects. Hence, nanotubes seemed to be 10-20 nm increased in their length.